

PATTERN FORMATION IN EVAPORATING DROPS

by

Fang-I Li

BS, National Cheng Kung University, 2001

MS, National Cheng Kung University, 2003

Submitted to the Graduate Faculty of
Swanson School of Engineering in partial fulfillment
of the requirements for the degree of
Doctor of Philosophy

University of Pittsburgh

2008

UNIVERSITY OF PITTSBURGH
SWANSON SCHOOL OF ENGINEERING

This dissertation was presented

by

Fang-I Li

It was defended on

October 23, 2008

and approved by

Dr. Ian Nettleship, Associate Professor, Department of Mechanical Engineering and Materials
Science

Dr. Jennifer Gray, Assistant Professor, Department of Mechanical Engineering and Materials
Science

Dr. Jörg M.K. Wiezorek, Assistant Professor, Department of Mechanical Engineering and
Materials Science

Dr. Sung Kwon Cho, Assistant Professor, Department of Mechanical Engineering and
Materials Science

Dr. John A. Barnard, Professor, Department of Mechanical Engineering and Materials
Science
Dissertation Director

PATTERN FORMATION IN EVAPORATING DROPS

Fang-I Li, PhD

University of Pittsburgh, 2008

The redistribution of organic solutes during drop evaporation is a nanoscale self assembly process with relevance to technologies ranging from inkjet printing of organic displays to synthesis of bio-smart interfaces for sensing and screening. Atomic force microscopy studies comparing the behavior of different generation dendrimers with different surface chemistry in two solvent alcohols on mica substrates confirm that the detailed morphologies of condensed dendrimer ring structures resulting from micro-droplet evaporation sensitively depend on the surface chemistry, the solute evaporation rate and the dendrimer generation. For the dilute concentration studied here the presence of periodically ‘scalped’ molecular rings is ubiquitous. The instability wavelength of the scalped rings is found to be proportional to the width of the ring, similar to observations of the rim instability in dewetting holes. The effect of the surface chemistry of the dendrimer molecules is obvious in the detailed structure of the self assembled rings. Varying the chain length of solvent alcohol leads to modification of ring patterns. The influence of dendrimer generation on ring structure primarily reflects the increase in dendrimer density with generation number. The evolution of G2-50%C₁₂-pentanol rings as a function of dendrimer concentration is also described. High surface mobility and phase transformation phenomena in condensed, micro-scale dendrimer structures are documented, again using atomic force microscopy. Stratified dendrimer rings undergo dramatic temperature, time and dendrimer generation dependent morphological changes associated with large-scale molecular rearrangements and partial melting. These transformations produce ring structures consisting of

a highly stable first monolayer of the scalloped structure in equilibrium with spherical cap shaped dendrimer islands that form at the center of each pre-existing scallop (creating a ‘pearl necklace’ structure). Analysis of the dendrimer island shapes reveals a dependence of island contact angle on contact line curvature (island size) that varies systematically with dendrimer generation. The morphological transformations in this system indicate the potential for creating complex, dendrimer-based multilevel structures and macroscopic scale arrays using, for example, droplet-on-demand or dip pen nanolithography techniques, coupled with appropriate annealing and stabilizing treatments.

TABLE OF CONTENTS

PREFACE.....	XII
1.0 INTRODUCTION.....	1
2.0 LITERATURE REVIEW.....	6
2.1 DENDRIMER MOLECULES.....	6
2.2 SELF-ASSEMBLY OF DENDRIMER MONOLAYERS	7
2.3 PATTERN FORMATION IN DRYING DROPS.....	8
2.4 WETTING PHENOMENA IN THREE PHASE SYSTEMS.....	10
2.5 THE CONTACT LINE TENSION CONTROVERSY	13
3.0 EXPERIMENT DETAILS	18
3.1 DENDRIMER MOLECULES.....	18
3.2 SOLUTION PREPARATION.....	19
3.3 DROPLET FORMATION.....	20
3.4 SUBSTRATES	20
3.5 ATOMIC FORCE MICROSCOPY.....	21
3.6 CONTACT ANGLE MEASUREMENTS.....	21
3.7 THERMAL STABILITY OF RING STRUCTURES	22
4.0 HYPOTHESES.....	27
5.0 OBJECTIVES	29

6.0	DENDRIMER PATTERN FORMATION FROM EVAPORATING DROPLETS	
	- INITIAL RESULTS	31
6.1	A UNIQUE MORPHOLOGY - PERIODICALLY ‘SCALLOPED’ MOLECULAR RINGS	31
6.2	THE EFFECT OF INCREMENTAL CHANGES IN DENDRIMER SURFACE CHEMISTRY ON STRATIFICATION OF THE RING STRUCTURES	32
6.3	THE ‘SCALLOPED’ MORPHOLOGY AND ITS RELATION TO THE RAYLEIGH INSTABILITY	34
6.4	RING WIDTH AND RING DIAMETER.....	35
6.5	MORPHOLOGICAL INSTABILITY AT SHORTER LENGTH SCALES	36
7.0	SOLVENT, SOLUTE SIZE, AND CONCENTRATION EFFECTS.....	43
7.1	DENDRIMER RING STRUCTURE DEPENDENCE ON SOLVENT AND DENDRIMER GENERATION.....	44
7.2	THE INSTABILITY WAVELENGTH.....	47
7.3	RING WIDTH AND RING DIAMETER.....	50
7.4	THE MORPHOLOGICAL EVOLUTION OF G2-50%C_{12}-PENTANOL RINGS AS A FUNCTION OF DENDRIMER CONCENTRATION	51
8.0	THERMAL EVOLUTION OF STRATIFIED DENDRIMER RING STRUCTURES.....	59
8.1	PRELIMINARY OBSERVATIONS	59
8.2	THERMAL STABILITY AND MOLECULE SIZE.....	63
8.2.1	G2-50%C_{12}.....	65
8.2.2	G3-50%C_{12}.....	66

8.2.3	G4-50% C_{12}	68
8.3	TIME DEPENDENT STABILIZING EFFECT ON RING STRUCTURE.	70
8.4	DEPENDENCE OF ISLAND CONTACT ANGLE ON CONTACT LINE CURVATURE.....	71
9.0	CONCLUSIONS AND RECOMMENDATIONS FOR FUTURE WORK.....	99
9.1	SURFACE CHEMISTRY EFFECTS.....	99
9.2	EVAPORATION RATE AND THE DENDRIMER GENERATION EFFECTS	100
9.3	THERMAL EFFECTS.....	101
9.4	FUTURE WORK.....	102
	BIBLIOGRAPHY	103

LIST OF TABLES

Table 3.1 Dendrimer Physical Constants.....	23
---	----

LIST OF FIGURES

Figure 1.1 A coffee drop stain	5
Figure 2.1 Schematic of physical and chemical structure of PAMAM dendrimers in solution. ..	14
Figure 2.2 Schematics of a dendrimer in solution and a dendrimer monolayer.	15
Figure 2.3 Illustration of an equilibrium sessile drop.	16
Figure 2.4 Illustration of three-phase contact line region and interpretation of the line tension ..	17
Figure 3.1 Dendrimer solution micro-droplets produced by nebulizer.....	24
Figure 3.2 Schematic of AFM (Atomic Force Microscope).....	25
Figure 3.3 Schematic and photo of DSA100 (Drop Shape Analysis System).....	26
Figure 6.1 AFM topographic images of representative ring structures.	38
Figure 6.2 Topographic images and cross-sectional scans through a representative scallop.	39
Figure 6.3 Plot of mean wavelength and mean ring width.	40
Figure 6.4 Plot of width of the ring and ring diameter.	41
Figure 6.5 Topographic image (2.5 μm x 2.5 μm) of a G4-50% C_{12} scallop.	42
Figure 7.1 AFM topographic images of representative ring structures.	53
Figure 7.2 Topographic images and radial cross-sections through a representative ‘scallop’.	54
Figure 7.3 Plot of mean wavelength and mean ring width.	55
Figure 7.4 Plot of mean ring width and ring diameter.....	56
Figure 7.5 Topographic images and radial cross-sections through G2-50% C_{12}	57

Figure 7.6 Topographic images and radial cross-sections through G2-50%C ₁₂	58
Figure 8.1 The as-deposited scalloped ring structure.	74
Figure 8.2 AFM topographic images of G2-50%C ₁₂ ring structure.	75
Figure 8.3 AFM topographic images of G2-50%C ₁₂ ring structure.	76
Figure 8.4 Annealing sequence for G2-50%C ₁₂ ring at different temperatures.	77
Figure 8.5 Comparison of ideal spherical cap profile and AFM profile.....	78
Figure 8.6 AFM topographic images and cross sections of an individual scallop.	79
Figure 8.7 Annealing sequence for G2-50%C ₁₂ ring (d=27.7 μm) at 0.9 T _c (313K, 40°C).	80
Figure 8.8 Annealing sequence for G2-50%C ₁₂ ring (d=27.13 μm) at 0.95 T _c (331K, 58°C).	81
Figure 8.9 Annealing sequence for G2-50%C ₁₂ ring (d=33.84 μm) at 1.0 T _c (348K, 75°C).	82
Figure 8.10 Annealing sequence for G2-50%C ₁₂ ring (d=27.78 μm) at 1.05 T _c (365K, 92°C). ..	83
Figure 8.11 Annealing sequence for G2-50%C ₁₂ ring (d=30.63 μm) at 1.1 T _c (383K, 110°C). ..	84
Figure 8.12 Annealing sequence for G3-50%C ₁₂ ring (d=29.74 μm) at 0.9 T _c (331K, 58°C).	85
Figure 8.13 Annealing sequence for G3-50%C ₁₂ ring (d=29.67 μm) at 0.95 T _c (350K, 77°C). ..	86
Figure 8.14 Annealing sequence for G3-50%C ₁₂ ring (d=29.90 μm) at 1.0 T _c (368K, 95°C).	87
Figure 8.15 Annealing sequence for G3-50%C ₁₂ ring (d=29.95 μm) at 1.05 T _c (386K, 113°C). ..	88
Figure 8.16 Annealing sequence for G3-50%C ₁₂ ring (d=31.20 μm) at 1.1 T _c (405K, 132°C). ..	89
Figure 8.17 Annealing sequence for G4-50%C ₁₂ ring (d=24.38 μm) at 0.9 T _c (363K, 90°C).	90
Figure 8.18 Annealing sequence for G4-50%C ₁₂ ring (d=31.38 μm) at 0.95 T _c (383K, 110°C). ..	91
Figure 8.19 Annealing sequence for G4-50%C ₁₂ ring (d=27.14 μm) at 1.0 T _c (403K, 130°C). ..	92
Figure 8.20 Annealing sequence for G4-50%C ₁₂ ring (d=27.72 μm) at 1.05 T _c (423K, 150°C). ..	93
Figure 8.21 Annealing sequence for G4-50%C ₁₂ ring (d=30.42 μm) at 1.1 T _c (443K, 170°C). ..	94

Figure 8.22 Annealing sequences at 95°C (1.0 T _c) for two G3-50%C ₁₂ rings.	95
Figure 8.23 Equilibrium between dendrimer island and dendrimer monolayer.	96
Figure 8.24 Comparison of ideal spherical cap profile and AFM profile.....	97
Figure 8.25 Plot of Cos θ and local curvature.	98

PREFACE

I would like to gratefully and sincerely thank my advisor, Dr. John A. Barnard for giving the chance to work with him four years ago and all the advice, patience and guidance in all this years. I could have never accomplished this research without his help and support.

My thanks also go to my committee members: Dr. Ian Nettleship, Dr. Jennifer Gray, Dr. Jörg M.K. Wiezorek, Dr. Sung Kwon Cho, and Dr. John A. Barnard. I truly appreciate their time and help for making this dissertation better.

I also like to thank my Family and friends: Jin Lin, Chiajung Tsou, Yawey Huang, Chiayi Wen, Wanyu Wu, Minghui Chiu and Yaoting Tsai. Thank you all for your love, friendship, and companionship. Thank you for listening the complaining, for making me strong, for making each day so fun. I would like to express my gratitude to all those who gave me the possibility to complete this dissertation.

This research was supported by NSF-DMR-0213985.

1.0 INTRODUCTION

The redistribution of initially dispersed nanoscale solutes (e.g., globular macromolecules, inorganic nanoparticles) during evaporation of small drops on a surface is of fundamental scientific interest as a nanoscale self assembly or pattern formation process. Both the size of the drops and their special symmetry can lead to structures not accessible in more conventional studies of the evaporation of continuous liquid films.

The formation of condensed annular structures on smooth solid substrates following evaporation of a liquid droplet containing dispersed small particles has been successfully interpreted in terms of the coupling of contact line pinning and evaporation leading to fluid flow to the contact line. A coffee drop stain is a commonplace example of this phenomenon. This capillary flow concentrates the particles in a growing ‘ring’¹(see Figure 1.1). Pinning of the triple line at the junction of the vapor, liquid, and solid substrate phases is generally associated with substrate heterogeneities. However, if small particles are present in the liquid, it has been proposed that their accumulation at the contact line enhances the pinning^{2, 3} and that the competition between pinning and dewetting events during evaporation can lead to a variety of more complex particle patterns in the evaporated drop⁴.

Under certain conditions this process concentrates essentially all of the initially dispersed particles in a dense outer ring. A recent alternative interpretation proposes that pinning is not a prerequisite for ring formation, but rather that the convective flow carrying the particles to the

perimeter is the essential factor, with the circular ring-shape determined by the symmetry of the drop⁵. The detailed structure of the patterns which form during evaporation of small droplets are expected to be sensitive to experimental conditions such as the macromolecule/nanoparticle concentration and outer shell chemistry, the solvent type and evaporation rate, the surface chemistry and morphology of the substrate material, as well as the temperature of the system.

Somewhat surprisingly, there has been little work extending the evaporating drop experiment to exploration of systems containing nanoscale macromolecular solute constituents and smaller drop sizes more amenable to imaging by scanning probe microscopy (SPM) techniques (ring formation during evaporation of ~50 μm diameter droplets of ink-jet deposited water-based suspensions has very recently been studied using spectral imaging techniques)⁶. The ability to tailor with precision the chemistry of macromolecular solutes so as to control their interaction with each other and the substrate is a key attribute of these systems. Furthermore, an SPM technique such as tapping mode atomic force microscopy (AFM) yields three-dimensional topographic maps with the nanoscale spatial resolution required to more fully interpret the physical mechanisms and processes responsible for the dried drop patterns. While the problem of organic solute redistribution during droplet evaporation is attracting interests scientifically as a nanoscale self assembly process, it also underpins progress in critical technologies such as drop-on-demand inkjet printing of small structures and arrays for organic displays, polymer-based electronics, combinatorial materials science ^{e.g., 7-9} as well as development of ‘bio-smart’ interfaces^{10, 11} for bio-sensing and clinical screening¹²⁻¹⁴.

This PhD research dissertation builds on important progress made in understanding the interplay of contact line pinning, evaporation, and fluid flow in evaporating droplets. We demonstrate that a unique morphology (periodically ‘scalped’ and molecularly stratified rings)

distinct from those observed in other systems, results from micro-droplet evaporation of solutions of nanoscale dendrimer solute molecules in pentanol and hexanol solvent on mica substrates. The details of the morphology of the rings are shown to depend sensitively on dendrimer surface chemistry, dendrimer generation, solvent evaporation rate, and solvent concentration. Evaporated dendrimer droplet patterns can be interpreted as a complex ‘fingerprint’ reflecting the relevant physico-chemical interactions in the system. The validity of the concept that a pattern contains useful and interpretable information, when coupled with the idea of amplification (a small change in conditions in the drop leads to a substantial change in the patterns which form), indicates that such systems can function as sensors, in the broadest sense, for a variety of bio-chemical events.

Importantly, the presence of a scalloping instability indicates that the growing condensed dendrimer ring should be considered a *phase* rather than simply an aggregate or assembly of particles. This latter point implies that these structures (unlike the aggregates of discrete particles which dominate the literature) may evolve in interesting ways and produce unique morphologies when subjected to thermal treatment after (or during) evaporation. In fact we demonstrate that stratified dendrimer rings undergo dramatic temperature and time dependent (and dendrimer generation dependent) morphological changes are associated with large-scale molecular rearrangements and partial melting. These transformations produce ring structures consisting of a highly stable first monolayer of the scalloped structure in equilibrium with spherical cap shaped dendrimer islands that form at the center of each pre-existing scallop (a kind of ‘pearl necklace’ structure). As-evaporated structures can be stabilized against thermally driven rearrangements by holding the structures at room temperature before annealing instead of annealing freshly evaporated samples. Analysis of the dendrimer island shapes reveals a

dependence of island contact angle on contact line curvature (island size) that varies systematically with dendrimer generation. These morphological transformations point to the potential for creating complex multilevel structures and arrays of macroscopic scale using, for example, droplet-on-demand or dip pen nanolithography techniques, coupled with appropriate annealing and stabilizing treatments.

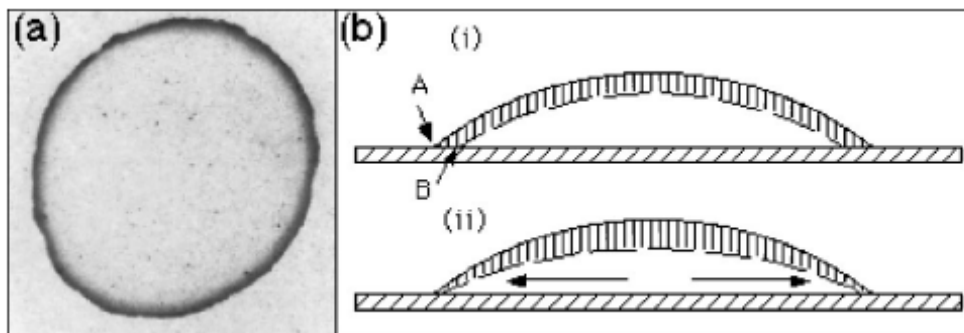


Figure 1.1 A coffee drop stain

(a) A photograph of a dried coffee drop. The dark perimeter is produced by a dense accumulation of coffee particles. The radius is approximately 5 cm. (b) Schematic illustration of the origin of the advective current. (i) If the contact line were not pinned, uniform evaporation would remove the hashed layer, the interface would move from the solid line to the dashed line, and the contact line would move from A to B. However, if the contact line is pinned then retreat from A to B is not possible, and there must be a flow that replenishes the lost fluid. (ii) Shows the actual motion of the interface and compensating current⁴.

2.0 LITERATURE REVIEW

2.1 DENDRIMER MOLECULES

"Dendrimers" or "starburst polymers" are regularly hyperbranched polymeric macromolecules that extend from a central core surrounded by generations of monomers which are covalently bonded. A dendrimer with n generations of monomers is denoted a G_n ('generation n ' dendrimer). They can be synthesized with controllable sizes (they are essentially monodisperse) determined by the core type, extent of branching, and nature of the end groups, in the range from \sim one to several tens of nm in diameter¹⁵⁻¹⁸. The core-shell structure and utility of dendrimers as nanoscale molecular building blocks has been compared to the core-shell architecture and reactivity of elemental atoms¹⁹. The origins of dendrimers may be traced back to 1978 when a repetitive synthesis process to create well-defined branching structures was successfully developed^{20, 21}. This new molecular architecture was originally called a "cascade molecule". The term "dendrimer" (greek: dendron = tree, meros = part) is now commonly used to describe this new class of molecules.

Poly(amidoamine) (PAMAM) dendrimers, in particular, have attracted intensive scientific and technological interest because of their unique properties and structure^{15, 22-25}. Both the physical characteristics of dendrimer molecule solutes and their adaptability to droplet evaporation studies are unique. Dendrimers are truly monodisperse, nanoscale, and

extraordinarily ‘tunable’ with regard to both size and chemistry. They are positively charged. Their small size makes them susceptible to both diffusive and advective motion, while control of terminal site chemistry enables design of dendrimer-dendrimer and dendrimer-substrate interactions. The molecular structure of PAMAM dendrimers is highly controllable and they can be readily synthesized in large quantities thus they have been used in numerous technological fields. For example, they are of interest for biological systems such as the targeted delivery of drugs^{26, 27} and anticancer agents^{28, 29}. A recent comprehensive review¹⁹ notes that more than 5000 references have appeared describing the structure and chemistry, methods of preparation, properties, and potential applications of these unique nanomaterials.

Commercially available poly(amidoamine) (PAMAM) dendrimers are used for all experiments in this PhD dissertation. The schematic physical structure and the chemical structure expected in the solution are presented in Figure 2.1.

2.2 SELF-ASSEMBLY OF DENDRIMER MONOLAYERS

Dendrimers can also form flat, complete monolayers on technologically relevant substrates using standard cleaning, dipping, and rinsing procedures.³⁰⁻³² Therefore, they are excellent model systems for studying self-assembly of organic molecules³³⁻³⁵ as well as metal-organic interfacial reactions, and nanocomposite formation.^{30, 36-39} Although they are roughly spherical in solution, dendrimers tend to ‘collapse’ when adsorbed onto substrate surfaces. The average heights (thicknesses) of both isolated molecules and monolayers are typically something less than half the diameter in solution, independent of generation (see Figure 2.2). For example, generation 4 (G4) PAMAM dendrimers, which have a solution diameter of 4.5 nm, have displayed monolayer

thicknesses on silicon ranging from 1.1 to 1.7 nm (scanning probe microscopy technique)³³ and from 1.4 to 2.2 nm (X-ray reflectance technique).³⁶

2.3 PATTERN FORMATION IN DRYING DROPS

The behavior of a fluid droplet on a solid surface has been studied for hundreds of years.⁴⁰ The self-assembled structures remaining on a surface following evaporation of a liquid droplet is now receiving renewed attention in the scientific and engineering communities. Understanding such morphologies is potentially important to high-throughput technologies from inkjet printing to drug screening. Deegan *et al.*, demonstrated that the structures remaining on a smooth solid substrate following evaporation of a liquid droplet (millimeter-scale) containing dispersed small particles (micron-scale) are broadly interpretable in terms of contact line pinning coupled with evaporation leading to fluid flow to the contact line. Figure 1.1 (b) depicts if the contact line is pinned, when the evaporation removes the liquid from around the contact line, a flow develops to keep the substrate wet. This capillary flow drags all the solute in the drop to the contact line where solute particles accumulate¹. A stain from a spilled drop of coffee is a commonplace example of the phenomenon. The force pinning the contact line generally comes from irregularities in the surface, such as roughness or chemical heterogeneity, but when small particles are present their accumulation at the contact line may enhance the pinning^{2,3}. Under certain conditions this process can concentrate essentially all of the initially dispersed particles in a dense outer ring. A recent alternative interpretation proposes that pinning is not a prerequisite for ring formation, but rather that the convective flow carrying the particles to the perimeter is the essential factor, with the circular ring-shape determined by the symmetry of the drop.⁵ The

competition between pinning and dewetting events during evaporation can also lead to a variety of more complex particle patterns in the evaporated drop.⁴ The physical parameters in the evaporating drop influence the processes of printing, washing and coating.⁴¹⁻⁴³

In addition to the work of Deegan *et al*^{1, 4, 44}, primarily on polystyrene microspheres in water (mm scale droplets), pattern formation phenomena in evaporating drops has also been reported by a number of other groups using various combinations of solute and solvent. These include carbon nanotubes in water⁴⁵ and aqueous SDS solution⁴⁶ (mm scale droplets), polystyrene nanospheres in water⁴⁶ (mm scale droplets), polystyrene microspheres in water⁴⁷ (0.1 mm scale droplets), collagen in acetic acid solutions⁴⁸ (mm scale droplets), colloidal silica in water^{49,50} (mm scale droplets), $\sim 0.1 \mu\text{m}$ silica particles in a water-C₂H₅OH solution⁵¹ (0.1 mm scale droplets), hydroxyapatite nanoparticles in water⁵ (mm scale droplets), silica microsphere ‘inks’^{52, 53} (0.1 mm scale droplets), NaCl, albumen, citric acid, urea, copper sulfate, sugar and 10 nm gold colloid, all in water⁵⁴ (mm scale droplets), ceramic suspensions^{55, 56} (mm scale droplets), DNA solution⁵⁷ (mm scale droplets), cyan water-based pigment ink⁶ (10 μm scale droplets), and motile and non-motile bacteria in water⁵⁸ (mm scale droplets).

Technological application of drop evaporation phenomena will depend on extracting useful ‘information content’ from analysis of the condensed patterns. In this context, very intriguing medical diagnostic applications of pattern formation in drying drops are beginning to appear in the literature. For example, analysis of dried serum droplet patterns has been successfully used for initial screening of patients suspected of having lymphoid pathologies⁵⁹. Pattern analysis has also been combined with acoustic mechanical impedance ‘signatures’ from drying serum drops to distinguish a wide range of diseases and physiological states⁶⁰. Drop

patterns have also been proposed as a biosensor for harmful nanobacteria in water¹². All of these examples use mm scale droplets.

2.4 WETTING PHENOMENA IN THREE PHASE SYSTEMS

Wetting behavior and contact angle related issues have attracted enormous attention over the past a hundred years⁶¹. Although these phenomena at macroscopic scale are well studied and understood, the subject of the contact angle of nano-droplets is still not well analyzed even though Gibbs introduced the concept of “line tension” more than a century ago⁶². Beyond fundamental scientific interest, a better understanding of this phenomenon is crucial to technologies such as soft lithography^{63, 64} and lab on chips.⁶⁵

In the early 19th century, Thomas Young postulated “Young’s Equation” to illustrate the force balance at a solid surface in the region where three immiscible co-existing phases meet. (Fig. 2-3)⁴⁰ The equilibrium at a three phase contact line is then given by the generalized Young’s equation:

$$\gamma_{lv} \cos \theta = \gamma_{sv} - \gamma_{sl} \quad (1)$$

where γ_{lv} is the liquid-vapor interfacial tension, γ_{sv} is the solid-vapor interfacial tension, γ_{sl} is the solid-liquid interfacial tension and θ is the equilibrium contact angle. From the equation, the contact angle is determined by the surface tension of the three phases in the system, therefore, the contact angle should be unique for a given solid-liquid-vapor system. However, in many cases, the experimental values of the contact angle in a given system have been found to vary.⁶⁶ Two explanations have been advanced: contact angle hysteresis⁶⁷⁻⁷⁴ and the drop size dependence of contact angle.⁷⁵⁻⁸³

Contact angle hysteresis results from the imperfections and the heterogeneity of the solid surfaces⁶⁷⁻⁷² and the presence of a thin liquid film on the solid surface⁷⁴. There is usually a wide range of contact angles for a give system with a non-ideal solid surface. The largest angle is denoted the advancing angle which is measured when a sessile drop has the maximum volume allowable for the liquid-solid interfacial area, that is to say, adding any more volume to the sessile drop dynamically will not increase its liquid-solid interfacial area. The smallest angle is termed the receding angle. If any volume is removed from the drop, the interfacial area will decrease. The difference between the advancing angle and receding angle is called contact angle hysteresis.⁶⁶

The phenomenon of drop size dependence of contact angle is ascribed to “contact line tension” which was first introduced by Gibbs. He believed that the three-phase contact line played a significant role in the solid-liquid-vapor system and should be treated as a surface discontinuity, i.e., line tension is a “one-dimensional analog of the surface tension”⁶². Unlike the contact angle hysteresis, which has been well studied, the drop size dependence of contact angle, namely, line tension is still controversial after a century of theoretical and experimental efforts. The line tension is defined as the excess free energy of a solid-liquid-vapor system per unit length of the contact line^{66, 84}, which is the reversible work to expand isothermally the unit length of the contact line.⁸⁵⁻⁸⁷

While the interfacial tension dominates the three-phase system, the contact line tension is expected to have a significant influence in nano-scaled sessile drop systems. In the nanometer range, we should take contact line tension into consideration when contact angle is determined. Hence, the modified Young equation⁸⁴:

$$\gamma_v \cos \theta = \gamma_{sv} - \gamma_{sl} - \tau \kappa \quad (2)$$

Where τ is the line tension and κ is the local curvature of the three-phase line on solid surface. In the case of an ideal solid surface and a perfectly circular contact line, the curvature of the three-phase line, κ , in Eq. (2) will be

$$\kappa = 1/a$$

where a is the radius of the contact circle. When $a \rightarrow \infty$, Eq. (2) will be replaced by the classic Young Equation:

$$\gamma_v \cos \theta_\infty = \gamma_{sv} - \gamma_{sl} \quad (3)$$

Combining Eq. (2) and Eq. (3) we get

$$\cos \theta = \cos \theta_\infty - (\tau/\gamma_v) (1/a) \quad (4)$$

$\cos \theta_\infty$ is a constant, therefore the contact angle will vary with drop size, that is to say the radius of the contact circle. From Eq. (4), a linear dependence of $\cos \theta$ on the local curvature is expected and, in principle, one may deduce the contact line tension. Theory predicts the τ is on the order of 10^{-11} J/m ⁸⁸⁻⁹². By plotting measured $\cos \theta$ versus $1/a$, both $\cos \theta_\infty$ and the ratio τ/γ_v can be extracted from a linear fit to the data. The magnitude of τ/γ_v corresponds to a characteristic length scale, c , over which the contact line tension acts. c is expected to be of order 1 nm for representative values of τ and γ_v (10^{-11} J/m and 10^{-2} J/m^2).⁹³ If γ_v is known then τ itself can be determined. Due to its small value, determining the line tension experimentally is difficult, thus, the contact line tension is probably the most controversial and uncertain quantity in wetting phenomenon. The apparent size dependence of the contact angle has recently been the subject of lively interest^{e.g.,93-101} (and some controversy), with both positive and negative τ deduced and arguments made for the inclusion in the analysis of a critical role for substrate heterogeneities⁹⁶. A comprehensive review from 2004 surveys the long history of interest in this topic⁹⁸.

2.5 THE CONTACT LINE TENSION CONTROVERSY

As mentioned before, line tension is defined as the excess free energy of a solid-liquid-vapor system per unit length of the contact line. Figure 2.4 schematically illustrates the two sources of the excess energy in the region of the three-phase contact line. If the line tension is interpreted by the molecular approach, it's generated by the excess molecular interactions in the transition zone causing local changes in the interfacial tension (Fig. 2.4 a). In this situation, the excess energy is proposed to be related to incomplete saturation of intermolecular interactions for molecules at the three-phase contact line. These interactions will cause distortion of the contact line in order to minimize the total excess energy so that the microscopic contact angle is different from the macroscopic contact angle. The other source of excess energy is local deformations in the transition zone due to the surface forces (Fig.2.4b). From this perspective, the interactions between liquid-vapor and solid-liquid interfaces cause the deformation of the shape of the liquid surface in the transition zone. Furthermore, the interactions between the interfaces will result in a difference between the surface tension of liquid in this region and liquid surface far away from the transition region⁸⁷. A full understanding of these issues is impeded by limitations in the resolution of experimental techniques used to measure contact angles in small droplets, therefore the experimentally determined line tension values are still uncertain. In addition, it has been demonstrated that imperfections (heterogeneity, roughness...) on the solid surface can significantly affect the precision of contact line energy measurements.^{80, 102, 103}

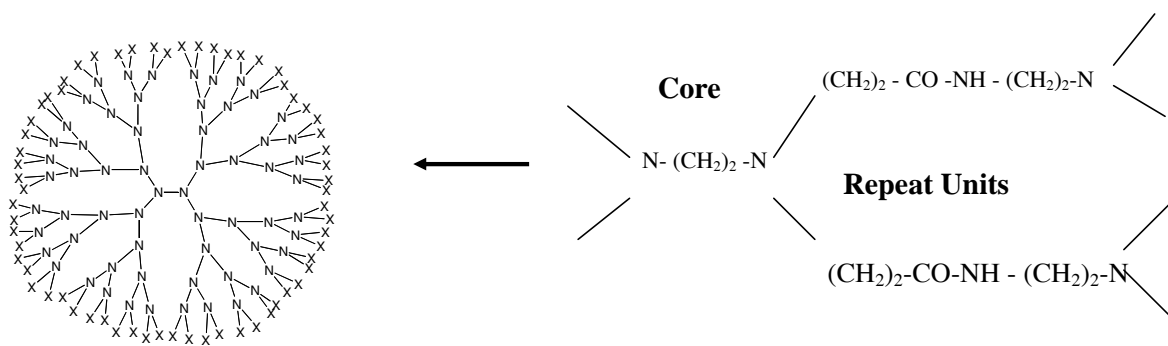


Figure 2.1 Schematic of physical and chemical structure of PAMAM dendrimers in solution.

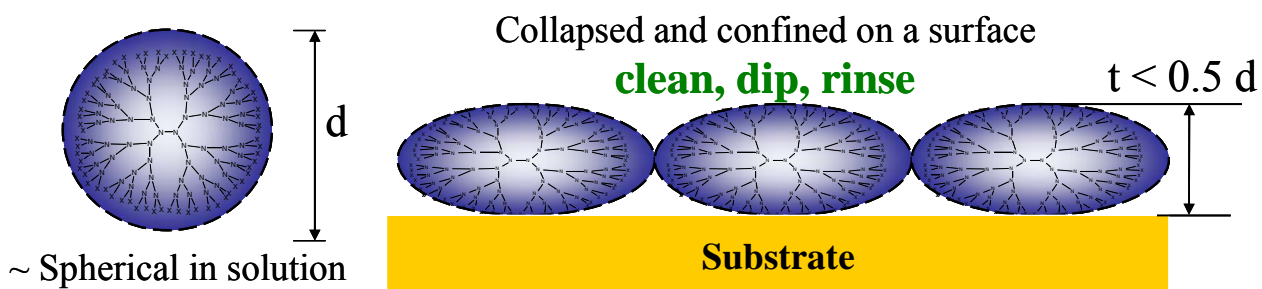


Figure 2.2 Schematics of a dendrimer in solution and a dendrimer monolayer.

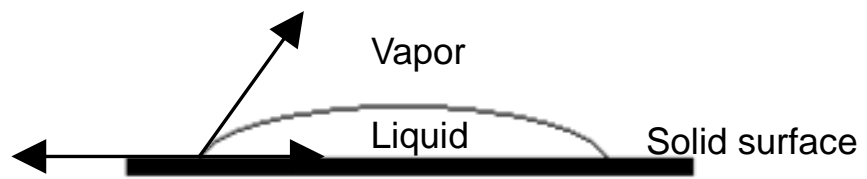


Figure 2.3 Illustration of an equilibrium sessile drop.

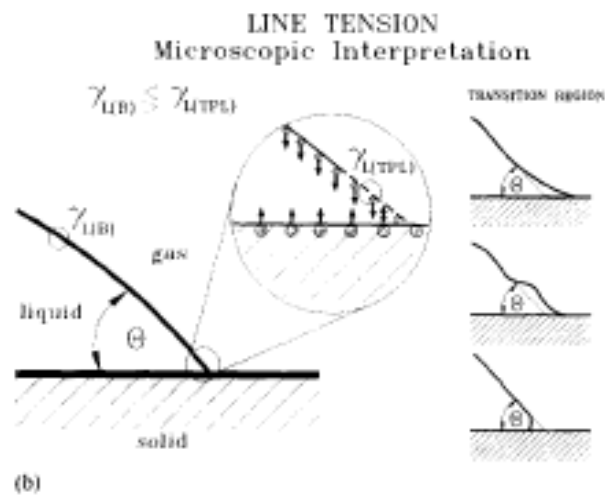
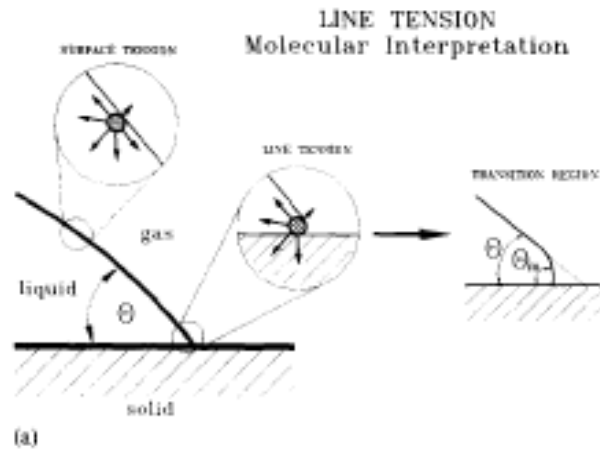


Figure 2.4 Illustration of three-phase contact line region and interpretation of the line tension

(a) molecular approach (b) microscopic approach.⁸⁷

3.0 EXPERIMENT DETAILS

3.1 DENDRIMER MOLECULES

Both the physical characteristics of dendrimer molecule solutes and their flexibility in droplet evaporation studies are unique. Dendrimers are truly monodisperse, nanoscale, and extraordinarily ‘tunable’ with regard to both size and chemistry. Their size makes them susceptible to both diffusive and advective motion, while control of terminal site chemistry enables design of dendrimer-dendrimer and dendrimer-substrate interactions.

Dendrimers are three-dimensional, globular, highly-branched macromolecules made up of a focal point core surrounded by repeated branch units, all enclosed by a terminal group 'shell'. Commercially available methanol-based poly (amidoamine) (PAMAM) dendrimer solutions purchased from Aldrich Chemical Company, Inc. (Milwaukee, WI) have been used in all experiments in this dissertation. A schematic structure of a PAMAM dendrimer appears in Figure 2.1. Dendrimers with different generation numbers are used to control the overall size of the dendrimer molecule as well as the number of surface sites. The expected size of selected PAMAM dendrimers in solution as a function of generation number is presented in Table 3.1. The structures studied in this dissertation were produced using pentanol- and hexanol-based solutions of generation 2 (G2) PAMAM-50% C₁₂ dendrimers (8 primary amino surface groups and 8 [N-(2-hydroxydodecyl)] surface groups, theoretical molecular weight 6205 amu),

generation 3 (G3) PAMAM-50% C₁₂ dendrimers (16 primary amino surface groups and 16 [N-(2-hydroxydodecyl)] surface groups, theoretical molecular weight 12,807 amu), and generation 4 (G4) PAMAM-50% C₁₂ dendrimers (32 primary amino surface groups and 32 [N-(2-hydroxydodecyl)] surface groups, theoretical molecular weight 26,011 amu). Pentanol solutions of generation 4 (G4) PAMAM dendrimers (64 terminal amine groups, theoretical molecular weight 14,215 amu), and generation 4 (G4) PAMAM-25% C₁₂ dendrimers (48 primary amino surface groups and 16 [N-(2-hydroxydodecyl)] surface groups, theoretical molecular weight 20,113 amu) are also used in comparison with generation 4 (G4) PAMAM-50%C₁₂ in Chapter 6. The different dendrimer molecules (hereafter referred to as G2-50%C₁₂, G3-50%C₁₂, G4-50%C₁₂, G4-25%C₁₂, and G4) combined with different solvent alcohols yielded a range of solutions as described below.

3.2 SOLUTION PREPARATION

All dendrimer solutions were prepared by simple volumetric dilution of as-received 20 wt % (G2-50%C₁₂ and G3-50%C₁₂) or 10 wt % (G4-50%C₁₂) methanol-dendrimer solutions obtained from Aldrich (Milwaukee, WI) using pentanol, hexanol as the solvent to produce solutions with different evaporation rates. All 0.1 wt % solutions thus contain a very small fraction of methanol in addition to pentanol or hexanol. One solution type, G2-50%C₁₂-pentanol, was also prepared over a range of concentrations (0.1, 0.3, 1.0, 3.3, and 10 wt %). For this series, at the higher concentrations the fraction of methanol is therefore substantial.

3.3 DROPLET FORMATION

Small droplets of alcohol-dendrimer solution were produced using a concentric nebulizer (Meinhard Glass Products) and 30 psi N₂ gas, collected on the freshly cleaved surface of mica, and allowed to evaporate under ambient conditions (see Figure 3.1). By controlling the time of deposition it is possible to collect large numbers of isolated droplets in a single run and minimize the number of overlapping droplets. The diameters of the dried molecular rings ranged from ~ 2 – 40 μm. The range of diameters corresponds to ~ 0.28 femtoliters – 2.24 picoliters based on a contact angle of 20° which is typical for these solutions. The great advantage of this process is the simultaneous deposition of large numbers of droplets under identical experimental conditions on a single substrate. Every droplet is in effect an individual experiment. The disadvantage is the lack of precise control of droplet size and location.

3.4 SUBSTRATES

The cleanliness of the substrate is crucial in obtaining reproducible results in this research. Mica is a potassium aluminum silicate mineral, which has the form of $\text{KAl}_2(\text{AlSi}_3\text{O}_{10})(\text{OH})_2$. The mica sheets are purchased from Structure Probe, Inc. Freshly pried mica (the mica sheet is separated using an ‘Exacto’ knife) provides a clean, atomically flat, homogeneous substrate surface eliminating the potential interference of surface irregularities. Mica substrates are simple to prepare and extremely flat and yield AFM images with high spatial resolution and contrast.

3.5 ATOMIC FORCE MICROSCOPY

Atomic force microscopy (AFM) utilizes a sharp tip rastered over the sample surface to generate a 3-D topographic image. A constant force is maintained between the tip and the sample. As the tip moves over the surface of the sample, the cantilever bends in response to the force between the tip and sample. The laser reflected by the cantilever is detected by a photosensitive detector (PSD). By measuring the differences in signal at the PSD, the roughness of the sample can be measured (Figure 3.2). The AFM technique includes three standard operation options: contact mode, tapping mode, and non-contact mode. In this dissertation the resulting condensed dendrimer structures formed from individual droplets were characterized in air by atomic force microscopy (AFM) in ‘tapping mode’ with a standard tip (Digital Instruments, Inc., model D-3100). The radius of the tip is 10 nm. The patterns are stable under ambient conditions over many weeks.

3.6 CONTACT ANGLE MEASUREMENTS

Contact angles of the solutions are measured by DSA 100 (Drop Shape Analysis) by Kruss GmbH (Germany) to analyze basic wetting behavior. The Kruss system uses proprietary DSA1.9 software to analyze the drop image. When a drop on the sample is placed on the moveable sample table, it is illuminated from one side and the camera on the other side records images of the drop (Figure 3.3). Drop images are transferred into a computer equipped with a video-digitizer board (frame grabber) and shown on the monitor. With the help of the DSA1.9 software it is possible to calculate the contact angle, surface energies and surface tensions.

Contact angle measurements of macroscopic drops of pure pentanol and hexanol and the pentanol- and hexanol-based dendrimer solutions were made on mica and indicate that the pure alcohols and the diluted dendrimer alcohol solutions had contact angles of $\sim 20^\circ$ for pentanol and $\sim 26^\circ$ for hexanol.

3.7 THERMAL STABILITY OF RING STRUCTURES

The stability experiment was carried out by annealing samples on a digital hot plate at desired temperatures. In order to have a standard reference state for studying relative stability, all samples were imaged immediately after evaporation (the as-deposited state) and then annealed within one hour of droplet deposition and evaporation using a digital hotplate. A small volume ‘oven’ was created by inverting a glass Petri dish on top of a digital hotplate, preset at the temperature of interest. Samples were slipped under the edge of the Petri dish in direct contact with the aluminum block of the hotplate, and removed as soon as the desired annealing time was reached. The annealing history is thus essentially isothermal, with rapid heating and cooling transitions. Spatial coordinates and registration marks on the mica were used to locate and image the same rings in the as-deposited and annealed states.

Table 3.1 Dendrimer Physical Constants.

Molecular diameter in solution (D), thickness of monolayer, molecular density of the unadsorbed molecule (ρ) and adsorbed as a monolayer (ρ_{ML}), number of terminal amine groups (N), theoretical molecular weight (MW), and calculated areal density (Γ) of NH₂ groups at the dendrimer surface as a function of dendrimer generation number. Values calculated from technical information available from Dendritech, Inc.

G	D (nm)	Thickness (nm/ML)	ρ (g/cm ³)	ρ_{ML} (g/cm ³)	N (# end groups)	MW (a.u. x 10 ³)	Γ (nm ⁻²)
4	4.5	1.8	0.49		64	14.2	1.0
25%G4	10.7	4.7	0.80		64	201.1	
5	5.4		0.58		128	28.8	1.4
6	6.7	2.8	0.61		256	58.0	1.8
7	8.1	3.7			512	116.5	2.5
8	9.7	4.6	0.81	1.1	1024	233.4	3.5
9	11.4		1.00		2048	467.2	5.0
10	13.5	5.6	1.21		4096	934.7	7.2

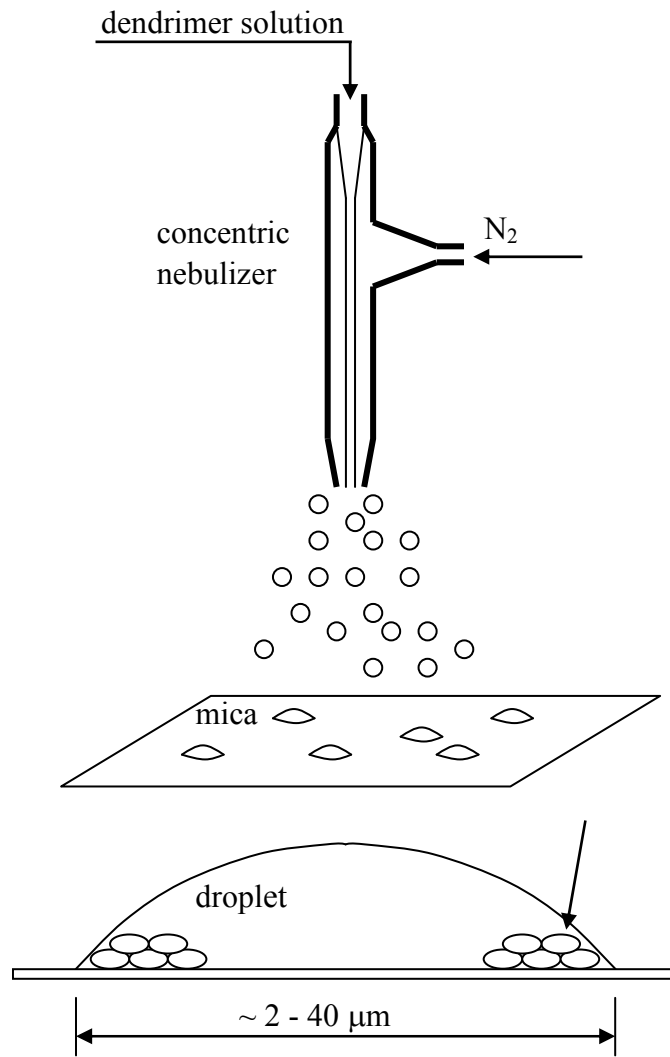


Figure 3.1 Dendrimer solution micro-droplets produced by nebulizer.

Droplets settle on freshly cleaved mica and then evaporate. Ring structures develop by accumulation of molecules at pinned contact line.

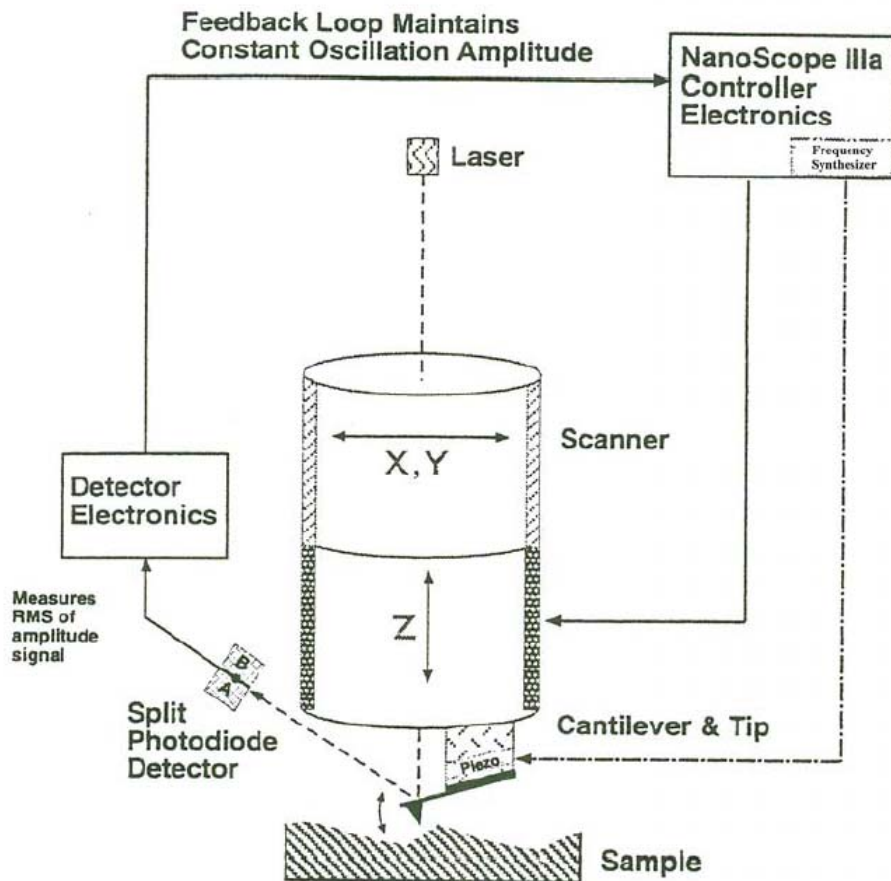


Figure 3.2 Schematic of AFM (Atomic Force Microscope).

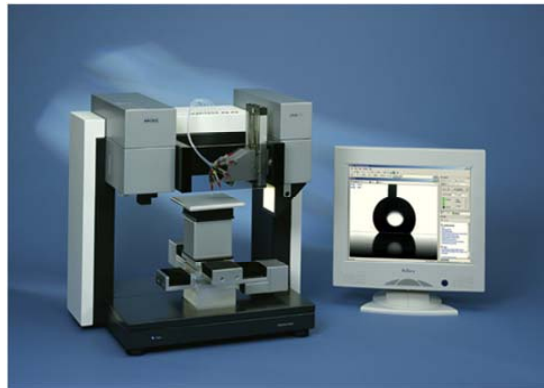
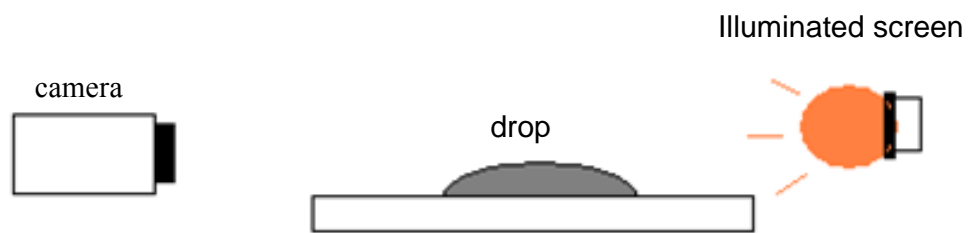


Figure 3.3 Schematic and photo of DSA100 (Drop Shape Analysis System).

4.0 HYPOTHESES

The core working hypothesis to be explored in this PhD dissertation is that *incremental* changes to experimental conditions (including small changes to the surface chemistry of discrete nano-scale macromolecules in dilute solution, solute concentration, solute size, and solvent evaporation rate) will lead to *substantive, reproducible, and interpretable* changes in the morphology of the self-assembled micron-scale patterns which result from evaporation of droplets of the solution on a substrate. A corollary to this hypothesis is that the detailed structure of the pattern may serve as a ‘fingerprint’ of interactions in the system and that they therefore may function as a sensor, in a broad sense, for physical, chemical, and biological events. The sensitivity and reliability of a nanoscale ‘fingerprint’ technique of this type as an indicator for a specific ‘interaction’ or ‘condition’ will eventually depend on development of ‘libraries’ of patterns which serve as comparison exemplars for the phenomena of interest. The research carried out in this dissertation will serve primarily as a proof of concept testing the basic hypothesis, but it will also provide guidance on development of pattern libraries.

The unique characteristics of the solute macromolecule (the dendrimer) selected for study (compared with the standard oxide or metal nanoparticle) also lead us to explore a secondary hypothesis, that dendrimer molecules might respond to post-evaporation annealing in a manner more consistent with a condensed phase, rather than a simple aggregate of individual nanoparticles.

In Chapter 6 (Dendrimer Pattern Formation from Evaporating Droplets – Initial Results) solutions of dendrimer molecules with incrementally varying terminal site chemistry were used in an initial test of the hypothesis to determine whether the condensed molecular patterns resulting from micro-droplet evaporation sensitively depend on, and are characteristic of, the surface chemistry of the solute molecules.

In Chapter 7 (Solvent, Solute Size, and Concentration Effects) this work is then extended to explore the effects of dendrimer concentration, dendrimer size, and solvent evaporation rate. Varying the chain length of the solvent alcohol (in our case comparing pentanol and hexanol) is expected to lead to modification of the dendrimer ring patterns, primarily due to the dependence of the evaporation rate on vapor pressure (for free evaporation of a liquid sphere the evaporation rate is proportional to the vapor pressure¹⁰⁴). The role of solute size is explored by using three different generation dendrimers, G2, G3, and G4. The effects of solute concentration are examined in a series of G2-based solutions with weight fractions varying over two orders of magnitude.

Finally, in Chapter 8 (Thermal Evolution of Stratified Dendrimer Ring Structures), the stability of the dried dendrimer patterns is examined by subjecting them to systematic thermal treatments. These annealing treatments were expected to induce changes in topography at a ‘critical’ temperature which depends on the size of the molecules.

5.0 OBJECTIVES

The overall goal of this PhD research dissertation is to develop new understanding of complex pattern formation phenomena associated with redistribution of nanoscale solutes, initially dispersed in very small droplets, during evaporation on a solid surface. Understanding this seemingly simple physical behavior is of fundamental scientific interest as a unique geometrically constrained nanoscale self assembly or pattern formation process. An improved understanding of this behavior in picoliter volume and smaller droplets is particularly important to progress in rapidly developing technologies such as ‘drop-on-demand’ printing of small structures and arrays for organic displays, polymer-based electronics, photonic crystals, and combinatorial materials science, as well as bio-sensing, clinical screening, and drug delivery concepts. Although the viability of potential applications is clearly important, this work is designed to be primarily fundamental in emphasis and aimed at understanding physical mechanisms and root causes.

The objective of this dissertation research is organized into five more specific research goals.

Research goals:

1. To understand the key morphological features of the dendrimer assembly process produced in freely evaporating picoliter volume droplets of alcohol-dendrimer molecule solutions deposited on substrates.

2. To understand the solute concentration dependence of pattern formation.
3. To understand the effects of dendrimer outer shell chemistry and size on pattern formation.
4. To understand the role of evaporation rate on the assembly process.
5. To understand the stability of the dendrimer patterns under thermal treatment.

6.0 DENDRIMER PATTERN FORMATION FROM EVAPORATING DROPLETS - INITIAL RESULTS

6.1 A UNIQUE MORPHOLOGY - PERIODICALLY 'SCALLOPED' MOLECULAR RINGS

A representative selection of the dried ring structures formed from three dendrimer-pentanol solutions (0.05 wt% of G4, G425%, G4-50%C₁₂) appear in Figure 6.1. The exteriors of the rings are essentially perfectly circular. Every ring shows distinctive interior waviness or 'scalloping' with clear evidence for periodicity. The contrast within the rings also makes clear that there is an undulation in the height of the ring coincident with the radial scalloping. The dimensions of the rings and the size of the scallops in the plane of the substrate are micron-scale but normal to the substrate the rings are only tens of nanometers thick. Note that the droplet size variation in the nebulized mist led to a natural variation in the ring diameter. The images in Figure 6.1 have been scaled to yield equal diameters on the printed page and arbitrarily arranged to show decreasing numbers of scallops from left to right for each dendrimer type. The uniform dark background contrast inside and outside the ring is the clean, very flat mica substrate (careful examination of cross-sections in Figure 6.2 reveals that the 'clean' mica interior is at the same elevation as the region outside of the ring which has not been exposed to the dendrimer solution). Contamination is minimal. For these solutions essentially all of the solute dendrimer molecules

initially dispersed in the volume of the micro-droplet, are transported to, and incorporated in, the growing ring, as the droplet evaporates with its contact line pinned. Note that the liquid droplet perimeter remains circular during this process. The direction of ring growth proceeds toward the center of the drop; the outer perimeter is pinned at an early stage of the process. Evaporation near the contact line tends to lower the contact angle which is compensated by flow of solvent (containing dendrimer molecules) to the perimeter¹. However, in contrast to the patterns formed from micron scale polystyrene particles in water⁴, where the structure is determined by intermittent dewetting events as the droplet evaporates, molecular rings show no evidence of local dewetting behavior. The interior scalloped edge of the ring is generally smoothly undulating at this scale and no secondary contact lines, which result from formation of dry patches, are formed. The dendrimer molecules appear to be incorporated in a continuous process which stops when the supply of dendrimers is exhausted.

6.2 THE EFFECT OF INCREMENTAL CHANGES IN DENDRIMER SURFACE CHEMISTRY ON STRATIFICATION OF THE RING STRUCTURES

The detailed structure of the scalloped rings is clearly revealed in magnified topographic images and cross-sectional scans through a representative scallop for each dendrimer molecule solution (Figure 6.2). In the top row of 5 μm x 5 μm topographic images the G4 dendrimer scallop has smoothly varying contrast with no evidence for stratification of the molecular layers (G4 molecules are expected to have a height of ~ 1.8 nm). As the terminal shell chemistry of the G4 dendrimer is progressively modified through replacement of the terminal amine groups with N-(2-hydroxydodecyl) surface groups (G4-25%C₁₂ and G4-50%C₁₂) stratification of the molecular

layers becomes quite apparent in the topographic images with sharp layering in G4-50%C₁₂. Cross-sectional scans cut radially and tangentially through the scallops quantitatively reveal extraordinary stratification of the dendrimer ring structure, with perfect dendrimer monolayer ‘terraces’ clearly visible, most strikingly in G4-50%C₁₂. The slope of the dendrimer surface as one ascends a scallop radially from outside the ring is much higher than inside the ring. The large difference between the horizontal and vertical scales in the cross-sections exaggerates the apparent slope. In the cross-sections cut along the long axis of the scallop (bottom row) the terraces are much easier to see at this scale as the scallops are elongated along the circumference; for G4-50%C₁₂ they are 300 - 400 nm wide compared to about ½ that value for the radial direction. Note also the flat, large plateau which caps the scallop. The mean step height from one terrace to another is ~ 4.5 nm for G4-25%C₁₂ (very close to that observed for isolated monolayer islands of G4-25%C₁₂ on mica¹⁰⁵) and ~ 4.7 nm for G4-50%C₁₂. The form of the monomolecular layering observed here may be described as a squat, terraced cone with a roughly elliptical rather than circular base. Molecular terracing somewhat reminiscent of the structures found here has been reported in drop spreading experiments with tetrakis(2-ethyleoxy)-silane¹⁰⁶ and Langmuir-Blodgett-Kuhn films of poly(amic acid) with azobenzene-chromophore side groups¹⁰⁷.

6.3 THE ‘SCALLOPED’ MORPHOLOGY AND ITS RELATION TO THE RAYLEIGH INSTABILITY

Topographic images of the dendrimer rings were quantitatively analyzed as follows. The diameter, d , is determined. The periodicity of the scalloping is quantified by marking the positions of the minima in the width of the ring (width is measured as a radial distance in the plane of the substrate) using visual inspection of the images at the scale shown. The number of minima in a ring is denoted k . Using d and k the arithmetic mean wavelength of the undulation, $\lambda = \pi d/k$, is calculated for a given ring. Using the marked positions of the minima, individual wavelengths are determined for all the undulations in a ring. Their standard deviation, s , is used to assess the ‘quality’ of the periodicity using the ratio, R , where $R = s/\lambda$. A representative value for the mean width of a dendrimer ring, w , is determined from the topographic images by determining the surface area of mica covered by dendrimers, A , and dividing this quantity by the perimeter, $w = A/\pi d$.

The interior scalloping of the dendrimer rings observed here is physically and visually reminiscent of the so-called ‘rim’ instability observed in dewetting holes¹¹⁰⁻¹¹⁴. The rim instability itself is considered a manifestation of the classic Rayleigh instability which explains the break-up of a cylinder of liquid into droplets¹¹⁵. For the rim instability case the predicted instability wavelength (corresponding to the fastest growing unstable mode) is 4 times the width of the rim. In Figure 6.3 λ versus w is plotted for rings from all three dendrimer solutions. The proportionality is quite evident. A slope of 4.6 fits the trend in the data and is indicated as a guide to the eye. Generally, the linearity of the λ versus w relationship improved in the order G4

→ G4-25% C_{12} → G4-50% C_{12} . Similarly the quality of the periodicity improved in the same order. The error bars on Figure 6.3 indicate \pm one standard deviation and reveal this trend.

6.4 RING WIDTH AND RING DIAMETER

There are uncertainties in the apparently straightforward evaporating drop experiment which should be mentioned. Although the solution from which the nebulized droplets for a given experiment are made at a fixed concentration the natural variation in the droplet size and transit time to the mica surface for individual droplet produce variations (presumably small) in dendrimer concentration (due to differential evaporation of pentanol in flight) from droplet to droplet as they land on the substrate and ring formation process starts. In addition, although the macroscopic contact angle of millimeter size droplets can be measured reliably in our current apparatus, there is variation, and one might expect larger variations for very small nebulizer-generated droplets whose contact angle may be affected by concentration and local substrate heterogeneities. Nevertheless, one should expect that the width of the ring should roughly scale with the ring diameter⁴. This would be strictly true for drops of different sizes but exactly equal concentrations and shapes. Figure 6.4 demonstrates that this trend is generally borne out in our experiments despite the experimental uncertainties. The line is a simple linear fit through all of the data and a guide for the eye. Once again, the linearity exhibited in Figure 6.4 improved in the order G4 → G4-25% C_{12} → G4-50% C_{12} . Note that the range of experimental values for d , l , and w was smallest for G4. This fact combined with the large R values found for G4 likely contributes to its less regular behavior in Figures 6.3 and 6.4.

6.5 MORPHOLOGICAL INSTABILITY AT SHORTER LENGTH SCALES

As the quality of the molecular terracing increases with the replacement of terminal amine groups with N-(2-hydroxydodecyl) surface groups, a smaller-scaled instability of the growth front at the inner edge of the ring are observed. A short wavelength undulation along individual terrace edges becomes very apparent in G4-50% C_{12} . The undulation is more pronounced at the front edge of the lower terraces (see Figure 6.5). Growth of highly stratified dendrimer ring structures thus appears to involve wavelength selection at two length scales. The undulation at the terrace edge has a wavelength of 100- 200 nm, roughly the same as the terrace width. Monolayer height defects ('holes'), concentrated closer to the front edge of the lower terraces, are occasionally also noted (not found in Fig. 6.5). In some rings there is a small region immediately in front of the lowest terrace which contains small dispersed islands of dendrimer molecules 'left behind' on an otherwise clean mica substrate.

At the molecular scale G4-50% C_{12} dendrimers (and to a less perfect extent G4-25% C_{12} dendrimers) which are transported to the growing condensed ring are incorporated at a terrace edge. The molecules clearly have sufficient mobility to reach these presumably low energy sites and the ring grows by lateral growth of the terraces. For this dendrimer molecule with this specific chemical termination a type of molecular 'step flow' regime obtains. By contrast G4 molecules appear to 'pile-up' at the growing ring in a more disordered fashion. Step flow is a concept typically associated with atomic epitaxial growth, first treated by Burton, Cabrera, and Frank¹⁰⁸. In this picture, atoms arriving at the surface of a growing crystal from the vapor phase diffuse on the terraces and either attach at a step site or desorb. Growth perpendicular to the terrace is accomplished monolayer by monolayer by flow of steps across the surface. Morphological instability leading to waviness of the terrace edges during epitaxial growth has

also been treated for atomic epitaxial growth and found to occur for asymmetric attachment energetics at the step, i.e., when there is a difference in the flux of atoms to a step from terraces above and below¹⁰⁹. While the clear similarities between step flow in epitaxial growth and the terraced ring patterns observed here are instructive there are important distinctions. In atomic epitaxial growth experimental conditions include constant flux of arriving atoms at the crystal surface. By contrast, in the evaporating drop experiment one has a finite reservoir of molecules whose flux to the growing terrace varies with time and depends on the number density of molecules in solution. The concentration of dendrimers in the solvent must evolve in a complex way determined by the pentanol evaporation and the dendrimer incorporation rates. Ring growth finally stops when the supply of dendrimers in solution is exhausted. The geometry of atomic epitaxial growth is approximated as an infinite plane with the direction of step flow confined to the plane and influenced by crystalline anisotropy. In the evaporating drop experiment the direction of growth is governed by the external symmetry of the drop itself and the convective flow of solute to the pinned perimeter and is thus, on average, radially directed toward the center of the drop. The crystallinity of the mica substrate (and any associated anisotropy) does not appear to influence molecular ring growth.

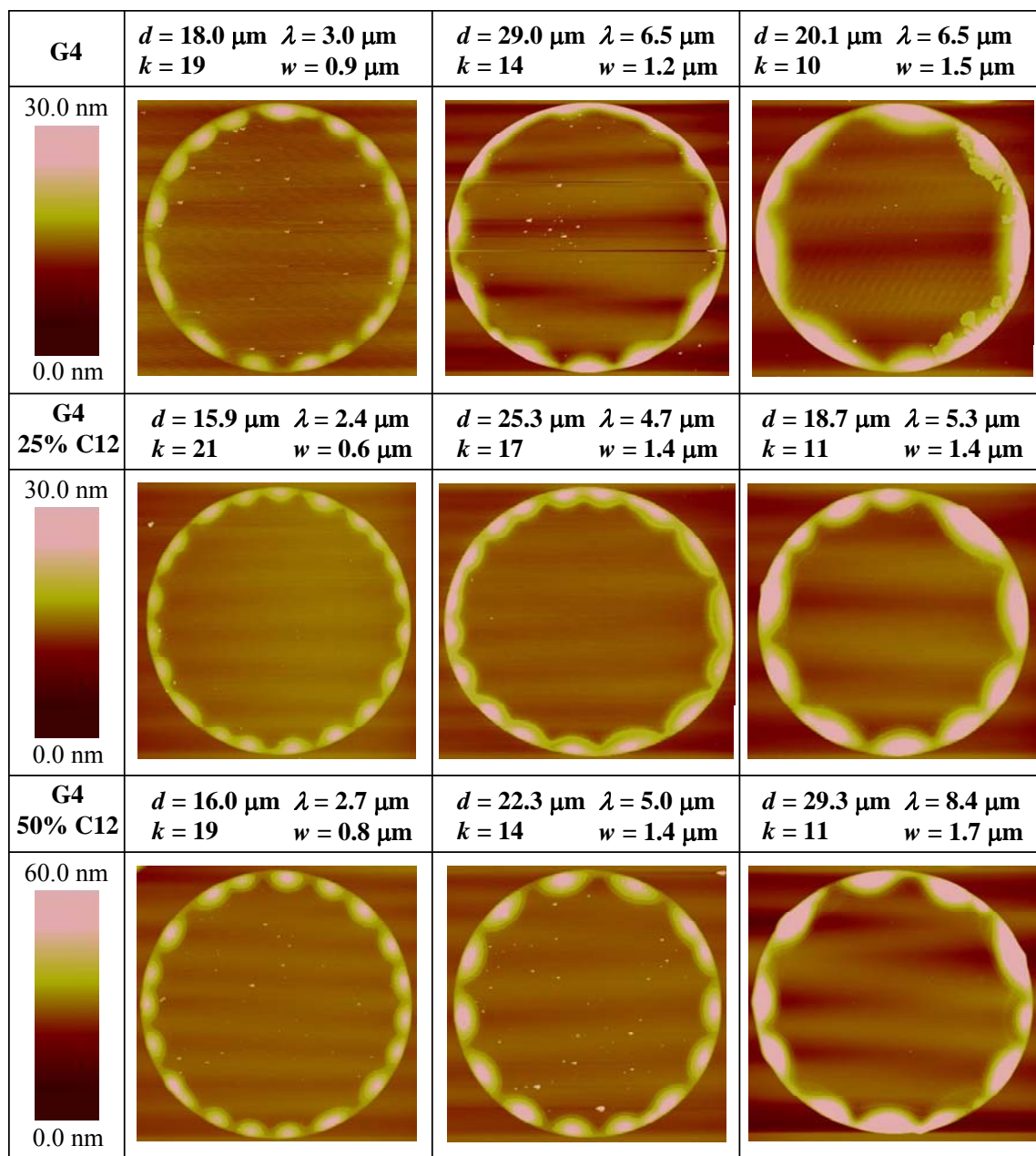


Figure 6.1 AFM topographic images of representative ring structures.

Patterns formed by evaporation of micro-droplets of G4 (top row), G4-25% C_{12} (middle row), and G4-50% C_{12} (bottom row) dendrimer-pentanol solutions (0.05wt%) on mica. The topographic images have been scaled to yield equal diameters on the printed page and arranged to show decreasing numbers of scallops from left to right for each dendrimer type. The diameter, d , the number of minima in the width of the ring, k , the mean wavelength of the undulation, λ , and the mean width of a dendrimer ring, w , are indicated above each ring.

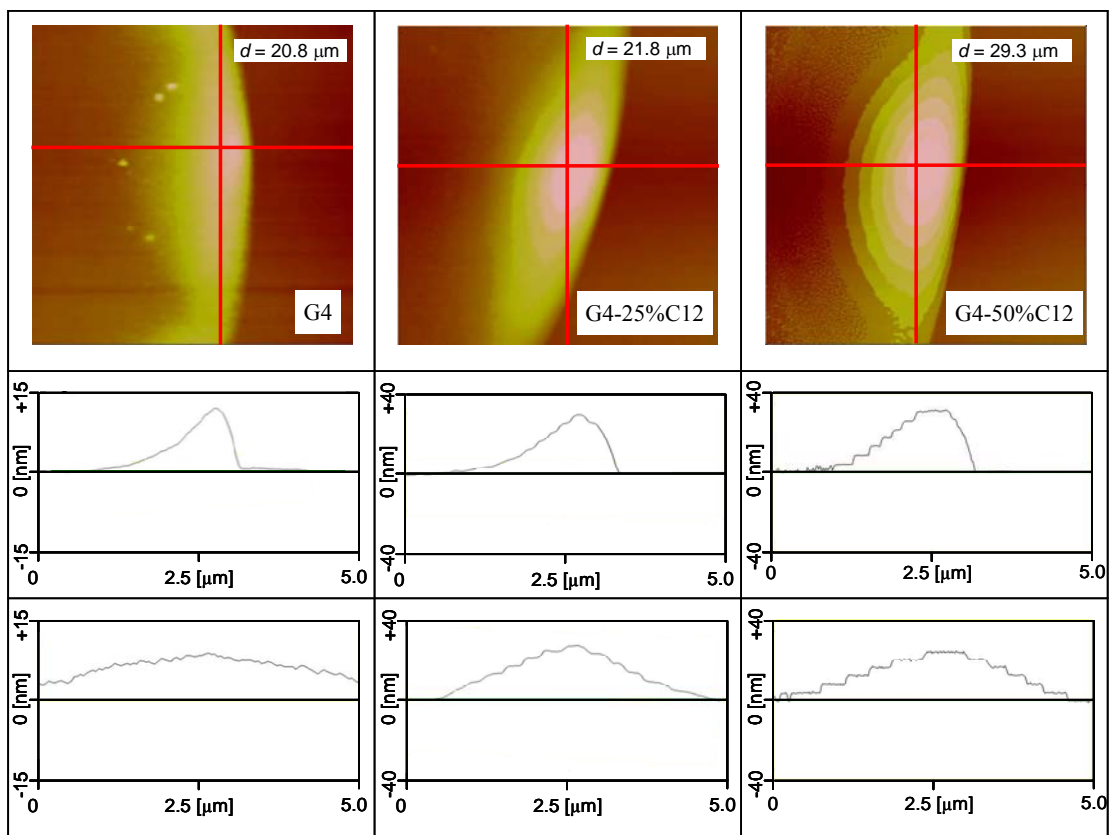


Figure 6.2 Topographic images and cross-sectional scans through a representative scallop.

Top row: $5\ \mu\text{m} \times 5\ \mu\text{m}$ topographic images. Middle row: radial cross-sections. Bottom row: tangential cross-sections. The diameters of the rings from which they are taken are indicated.

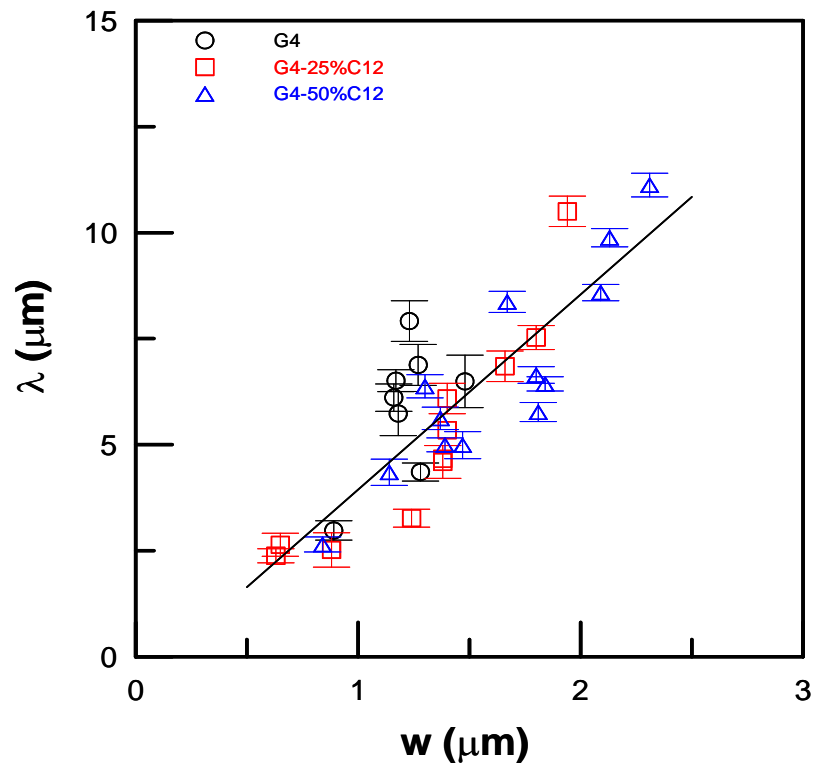


Figure 6.3 Plot of mean wavelength and mean ring width.

The mean undulation wavelength, λ , versus the mean ring width, w , for rings from three dendrimer-pentanol solutions (G4, G4-25%C₁₂ and G4-50%C₁₂).

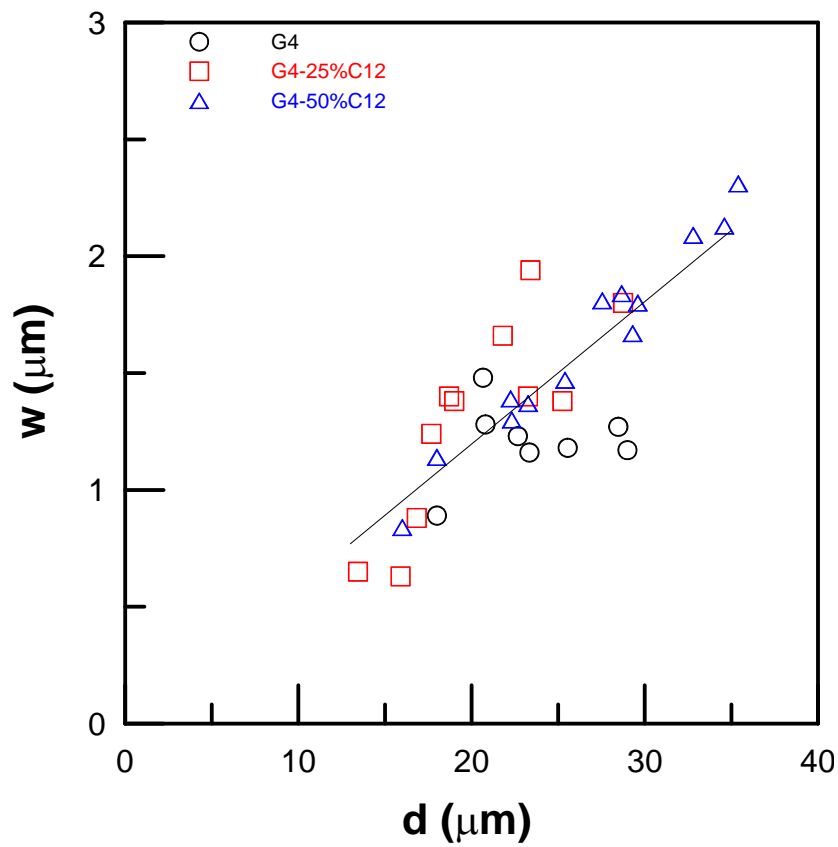


Figure 6.4 Plot of width of the ring and ring diameter.

Width of the ring, w , versus the ring diameter, d , for rings from all three pentanol-dendrimer solutions (G4, G4-25% C_{12} and G4-50% C_{12}).

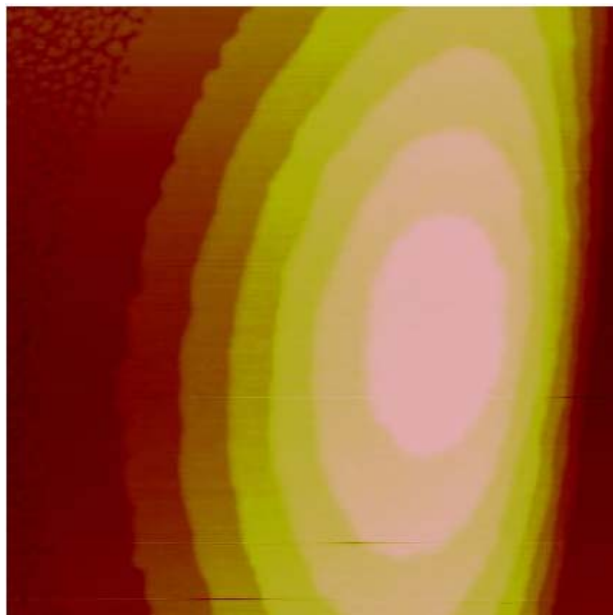


Figure 6.5 Topographic image ($2.5 \mu\text{m} \times 2.5 \mu\text{m}$) of a G4-50% C_{12} scallop.

Illustration of the short wavelength undulation along individual terrace edges. The undulation is more pronounced at the front edge of the lower terraces.

7.0 SOLVENT, SOLUTE SIZE, AND CONCENTRATION EFFECTS

In Chapter 6 we demonstrated (using dendrimer solute molecules, pentanol solvent, mica substrates, and ~ 10 μm scale droplets) that the condensed ring structures resulting from microdroplet evaporation sensitively depend on, and are characteristic of, the surface chemistry of the dendrimer solute molecules. For the dilute concentration studied, the presence of a unique morphology, periodically ‘scalped’ dendrimer rings, was ubiquitous. The instability wavelength of the scalped rings was determined to be proportional to the width of the ring, similar to observations of the rim instability in dewetting holes¹¹⁰⁻¹¹⁴. The role of dendrimer surface chemistry was obvious in the detailed structure of the self assembled rings. By incrementally varying the terminal site chemistry of the dendrimer molecules from 100% amine terminated to 50% amine – 50% [N-(2-hydroxydodecyl)] terminated, ring morphologies transitioned from scalped but vertically disordered (with no evidence for layer by layer molecular growth) to highly periodic scalps and very distinct monomolecular height terraced growth, with flat terraces and sharply defined steps. Pattern formation in the evaporating droplet thus depends sensitively on the chemistry of the dendrimer terminal shell which modulates dendrimer-dendrimer and dendrimer-substrate interactions.

In this Chapter we extend our work to examine the effects of evaporation rate, dendrimer molecule size, and solute concentration on ring pattern formation in evaporating dendrimer-alcohol microdrops on mica. Varying the chain length of the solvent alcohol (in our

case comparing pentanol and hexanol) is expected to lead to modification of the dendrimer ring patterns, primarily due to the dependence of the evaporation rate on vapor pressure (for free evaporation of a liquid sphere the evaporation rate is proportional to the vapor pressure¹⁰⁴). The vapor pressure of pentanol is a factor of three higher than hexanol¹¹⁶. Note that the viscosity of the solution is also affected, increasing by ~ 30% from pentanol to hexanol¹¹⁷. The role of solute size is explored by using three different generation dendrimers, G2, G3, and G4. Finally the effects of solute concentration are examined in a series of G2-based solutions with weight fractions varying over two orders of magnitude.

7.1 DENDRIMER RING STRUCTURE DEPENDENCE ON SOLVENT AND DENDRIMER GENERATION

AFM images of the ring structures resulting from the evaporation of dendrimer-pentanol and dendrimer-hexanol microdroplets were collected and analyzed. In Figure 7.1 we simultaneously compare both the effect of solvent alcohol (and thus evaporation rate) and dendrimer generation (and thus size). A selection of representative ring structures formed from the six dendrimer molecule solutions (G2-50% C_{12} , G3-50% C_{12} , and G4-50% C_{12} dendrimers in both pentanol and hexanol, all at the same 0.1 wt % dilution) appear in Figure 7.1. Roughly similar sized rings were selected for comparison (the droplet size variation in the nebulized ‘mist’ leads to a variation in the observed ring diameters on the mica surface). The images in Figure 7.1 have been scaled to yield equal diameters on the printed page.

There are some general features common to all of the rings formed from these six solutions (those shown in Figure 7.1, as well as many others studied but not displayed here). As

mentioned in chapter 6, the exteriors of all of the rings are essentially perfectly circular and every ring shows distinctive interior waviness or ‘scalloping’. This scalloping is generally very periodic. The image of the G2-50% C_{12} pentanol-based ring (upper-left) was selected as an exception to illustrate the ‘worst case scenario’ in terms of the regularity of scalloping. The remaining images in Figure 7.1 are ‘typical’. At this scale there is little evidence of local dewetting behavior (e.g., secondary contact lines associated with formation of dry patches).

Some trends in behavior which distinguish the solutions can also be observed in Figure 7.1. The interior scalloped edge of the pentanol-based rings is smoothly undulating at this scale while the hexanol-based rings exhibit a much rougher interior edge. The pentanol-based rings also exhibit cleaner mica interiors while the hexanol-based rings have a population of dispersed dendrimer islands in the interior. The overall ring morphology, at least as revealed in these topographic images, is not strongly affected by the dendrimer generation number (and thus the size of the molecule). However, it does appear that the width of the rings and the wavelength of the scalloped undulation decreases as the generation number increases. The trend in ring width can be explained by the fact that the density of the dendrimer molecules increases with generation number (size). The increase in density with generation number is apparent when the ratio of the molecular weight to molecular volume based on the hydrodynamic diameter is considered for PAMAM type dendrimers¹⁹. Thus, although the weight fraction in this series is fixed, the volume fraction is not, and decreases in the order G2-50% C_{12} \rightarrow G3-50% C_{12} \rightarrow G4-50% C_{12} . Perhaps just as significantly, the areal density of surface sites increases dramatically with generation number¹⁹. This steric crowding leads to stiffer, less ‘floppy’ spheroidal shapes in higher generation dendrimers which may lead to more efficient packing on assembly. The

steric crowding is also likely to influence the strength of the dendrimer-dendrimer chemical interactions. The quantitative relationship between the width and wavelength is explored below.

The detailed structure of the scalloped rings is more clearly observed in the magnified topographic images and cross-sectional scans through a representative scallop for each dendrimer molecule solution (Figure 7.2). In each image in Figure 7.2 the outer right hand portions (the '3 o'clock' position) of the full rings presented in Figure 7.1 were rescanned at $5\ \mu\text{m} \times 5\ \mu\text{m}$. These ring segments thus grow from right to left. In chapter 6, we have demonstrated that the terminal shell chemistry of the dendrimers selected for study (consisting of 50% standard PAMAM amine groups and 50% N-(2-hydroxydodecyl) surface groups) strongly promote stratification of the molecular layers during ring growth for G4-50%C₁₂. It is apparent in Figure 7.2 that the same type of mixed terminal shell chemistry also leads to extremely sharp layering in G2-50%C₁₂ and G3-50%C₁₂. Cross-sectional scans cut radially (Figure 7.2) and tangentially (not shown) through the scallops quantitatively reveal extraordinary stratification of the dendrimer ring structures, with nearly perfect dendrimer monolayer 'terraces' clearly visible. The slope of the condensed dendrimer structure ascending a scallop radially is consistently higher from outside than from inside the ring (the large difference between the horizontal and vertical scales in the cross-sections exaggerates the apparent slope). The terraces have widths (ranging from $\sim 100\ \text{nm}$ to more than $1\ \mu\text{m}$) that increase systematically toward the center of the ring. The scallop shapes are elongated along the circumference and flat, large plateaus cap the scallop (except for this particular example of G2-50%C₁₂-pentanol). The mean step height from one terrace to another measured on many samples is $\sim 3.6\ \text{nm}$ for G2-50%C₁₂, $\sim 4.1\ \text{nm}$ for G3-50%C₁₂, and $\sim 4.6\ \text{nm}$ for G4-50%C₁₂. The value for G4-50%C₁₂ is in good agreement with the result obtained earlier and described in Chapter 6. The dendrimer monolayer thickness increases,

as expected, with generation number, but is found to be essentially independent of the solvent used.

In examining the inner edge of the lowest terraces (the left hand side of each image), a smaller-scale instability of the growth front is observed. A short wavelength undulation, or more convoluted instability, becomes apparent along individual terrace edges. The undulation is more pronounced at the front edge of the lower terraces. The wavelength of this secondary instability is strongly affected by the solvent. In pentanol the wavelength of the instability is significantly smaller than the terrace width while in hexanol they are of similar magnitude. Growth of highly stratified dendrimer ring structures thus appears to involve wavelength selection in the overall morphology of the scallops and in the morphology of the front edges of the individual monolayer terraces of which they are composed. Monolayer height defects ('holes') are occasionally also noted (see G3-50% C_{12} -hexanol in Figure 7.2), and are generally found at the front edge of the lower terraces. In the pentanol-based rings there is a narrow region immediately in front of the lowest terrace consisting of small dispersed islands of dendrimer molecules 'left behind' on the otherwise clean mica surface, while the interior of the ring is free of dendrimer molecules. In the hexanol-based rings the inner edge of the lowest terrace terminates in a more convoluted boundary and somewhat larger islands of dendrimer molecules are distributed at lower density throughout the ring interior.

7.2 THE INSTABILITY WAVELENGTH

Quantifying the dendrimer rings as described in chapter 6, the mean wavelength (λ) and the width (w) is plotted in Figure 7.3 for rings from all six dendrimer solutions (three pentanol-

based and three hexanol-based). Grouping all the data from the three generations of dendrimer by solvent, and fitting the pentanol-based and hexanol-based data separately, the difference in the proportionality between λ versus w is apparent. A slope of 4.8 fits the trend in the data for pentanol-based solutions quite well and is indicated with the solid line as a guide to the eye. For hexanol, however, a lower slope of 2.3 is found and indicated with a dashed line. The linearity of the λ versus w relationship is slightly better in pentanol than hexanol. The overall quality of the periodicity of the scallops as measured by R (but not plotted here) is very good. The average R-value for all rings measured is 0.09 and similar in pentanol and hexanol. G3 and G4 rings are generally more regular than G2. The error bars on Figure 7.3 indicate \pm one standard deviation. Note that within each solvent group there is a sub-group organization by dendrimer molecule generation. That is, there is a loose clustering of squares (G2-50%C₁₂), triangles (G3-50%C₁₂), and circles (G4-50%C₁₂), reflecting the density increase with generation number, and the corresponding decrease in width and therefore, wavelength.

Understanding the sequence of events during ring formation is the key challenge to explaining the two instabilities (the large-scale morphological instability referred to as a ‘scallop’, and the small-scale waviness at the front edge of the terraces) observed in the condensed dendrimer patterns. Two possible explanations for the instabilities are considered, a Rayleigh-type¹¹⁵ interfacial energy driven process exemplified by the rim instability¹¹⁰⁻¹¹⁴, and a Mullins-Sekerka^{118, 119} type instability associated with the growth process itself. Two critical experimental results are generated by changing the solvent from pentanol to hexanol and thus dramatically slowing the evaporation process and decreasing the convective flux of dendrimer molecules to the perimeter of the drying droplet. For the scalloped structure we find a clear and significant decrease in the ratio λ/w as the evaporation rate slows. For the terrace edge

instability the ratio of the wavelength of the instability to the terrace width significantly *increases* as the evaporation rate slows. The behavior of the scallops runs counter to conventional models of growth-based morphological instability which predict a finer structure for the instability at higher fluxes. Rayleigh-type behavior, including the rim instability, does not depend on the flux. Thus changing the solvent from pentanol to hexanol can only affect the morphology of the scallops if there is a substantial difference in the interfacial energy between the well-ordered, condensed dendrimer phase, which makes up the growing ring, and these two solvents. Attempts to determine this interfacial energy via contact angle measurements have proven inconclusive; pure pentanol and hexanol both readily wet substrates coated with a continuous but ‘disordered’ dendrimer layer prepared by soaking the substrate in the dendrimer solution. The stage at which the wavelength of the scalloping instability is ‘set’ remains an open question; it could occur during growth of the ring or after all the molecules are accommodated in the ring but while the pentanol (or hexanol) solvent is still present. By contrast, the behavior of the secondary instability at the terrace edges is more readily explained – it is in line with expectations based on Mullins-Sekerka type analyses.

In the dilute regime all three dendrimers studied (0.1 wt% G2-, G3-, and G4-50% C_{12} in both pentanol and hexanol) are incorporated in a highly organized terraced ring structure with monomolecular height steps. These dendrimers have sufficient mobility to reach step edge sites, and the ring grows by lateral growth of the terraces. For these dendrimer molecules, and this particular chemical termination, a molecular ‘step flow’ regime obtains. From chapter 6, step flow is a concept typically associated with atomic epitaxial thin film growth¹⁰⁸. Atoms arriving at the surface of a growing crystalline solid from the vapor phase diffuse on the terraces, attach at a step site, or desorb. Growth perpendicular to the terrace (film thickening) is accomplished by

monolayer-by-monolayer flow of steps across the surface. Morphological instability leading to waviness of the terrace edges during atomic epitaxial growth has been found to occur for asymmetric attachment energetics at the step¹⁰⁹. The similarities between step flow in epitaxial growth and the terraced dendrimer ring patterns are interesting. However, in atomic epitaxial growth atoms arrive at the crystal surface at a constant flux, whereas, in the evaporating drop experiment, there is a finite reservoir of molecules whose flux to the perimeter varies with time and depends on the concentration of molecules in solution. The concentration of dendrimers in the solvent evolves with time as determined by the solvent evaporation and dendrimer incorporation rates. Ring growth terminates when either the solute is fully incorporated or the solvent evaporates. The geometry of atomic epitaxial growth is an infinite plane with step flow in the plane and influenced by crystalline anisotropy. In the evaporating drop experiment the growth direction is governed by the external symmetry of the drop and the convective flow of solute to the perimeter and is thus, on average, radial (directed toward the center of the drop).

7.3 RING WIDTH AND RING DIAMETER

The same dilution (0.1 wt% dendrimer) was used for all of the solutions from which the nebulized droplets in Figures 7.1, 7.2, and 7.3 were prepared. We have elaborated in chapter 6 that there are uncertainties (as the scatter seen in Figure 7.3) in this evaporation experiment, such as different evaporation rate of the solvents, the flying time of each droplet, and a small contact angle difference between pentanol and hexanol of millimeter size droplets ($\sim 20^\circ$ for pentanol-based and $\sim 26^\circ$ for hexanol-based solutions) which contribute to the variation (presumably small) in dendrimer concentration from droplet to droplet as they land onto the mica and ring pattern

growth begins. One might also expect contact angle variations in microdroplets due to local substrate heterogeneities. For drops of different sizes but equal concentrations and shapes (contact angles), the width of the resulting rings should scale with the ring diameters⁴. Figure 7.4 demonstrates again that this trend is broadly borne out in our experiments. In this plot the molecules are grouped by generation and for G3-50% C_{12} (triangles) and G4-50% C_{12} (circles) lines representing simple linear fits through the data serve as a guide for the eye. The quality of the fit for G4-50% C_{12} is better than G3-50% C_{12} . No fit has been displayed for G2-50% C_{12} as the scatter is large. Despite the experimental uncertainties, Figure 7.4 is also consistent with the explanation that the change in density of the dendrimer molecules as a function of generation number manifests itself in wider rings at a given diameter for smaller generation dendrimers (this feature was also noted in the discussion of Figure 7.1).

7.4 THE MORPHOLOGICAL EVOLUTION OF G2-50% C_{12} -PENTANOL RINGS AS A FUNCTION OF DENDRIMER CONCENTRATION

The shape evolution of the dendrimer rings as a function of the concentration of dendrimer molecules in solution was also explored by comparing five different G2-50% C_{12} -pentanol solutions (0.1, 0.3, 1.0, 3.3, and 10 wt %). Similarly-sized and representative rings from these solutions appear in Figures 7.5 (0.1, 0.3, and 1.0 wt %) and 7.6 (3.3 and 10 wt %). Increasing the concentration thickens and widens the rim (gradually filling in the center of the ring) while at least initially preserving the scalloped structure (0.1, 0.3, and 1.0 wt %). Terracing is still apparent, even in the large-scale topographic images, up to 3.3 wt % G2-50% C_{12} . At the highest concentrations the rings rapidly fill in and the scalloping disappears. Circular external

shapes are preserved throughout. Dried drop shape evolution is also tracked in corresponding cross-sections through the center of each ring. Monolayer terraces are apparent at the inner edge of the rings up through 3.3 wt % but terrace growth breaks down after a few monolayers and the majority of the additional dendrimers in solution are incorporated in the ring in a disordered manner creating the growing rounded rims that are apparent in the cross-sections. At 10 wt % the deposit is no longer a ring shape but rather a spherical cap with a depression in the middle. Note that while the lateral scale is identical in each cross-section the vertical scale increases with concentration.

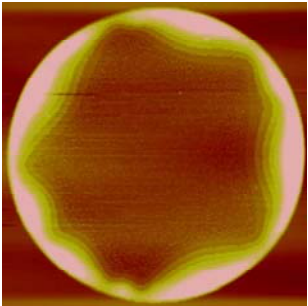
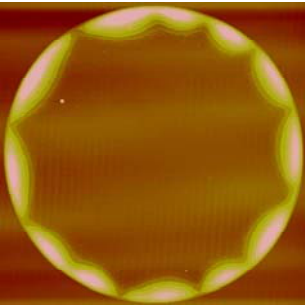
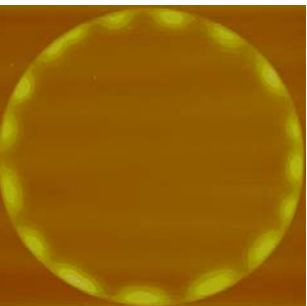
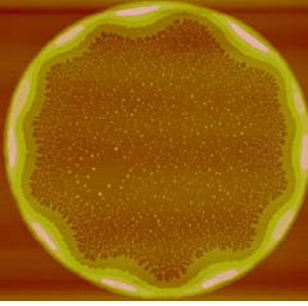
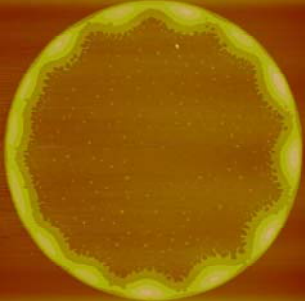
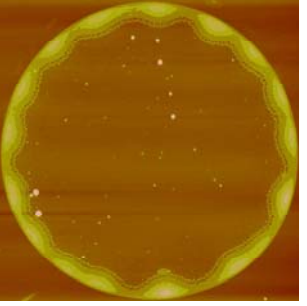
All at 0.1 wt%	G2-50% C_{12}	G3-50% C_{12}	G4-50% C_{12}
pentanol	$d = 25.7 \mu\text{m}$ $\lambda = 10.1 \mu\text{m}$ $k = 8$ $w = 2.7 \mu\text{m}$	$d = 29.4 \mu\text{m}$ $\lambda = 7.7 \mu\text{m}$ $k = 12$ $w = 2.0 \mu\text{m}$	$d = 20.4 \mu\text{m}$ $\lambda = 3.8 \mu\text{m}$ $k = 17$ $w = 1.0 \mu\text{m}$
60.0 nm  0.0 nm			
hexanol	$d = 28.7 \mu\text{m}$ $\lambda = 8.2 \mu\text{m}$ $k = 11$ $w = 2.9 \mu\text{m}$	$d = 21.2 \mu\text{m}$ $\lambda = 4.7 \mu\text{m}$ $k = 14$ $w = 1.2 \mu\text{m}$	$d = 22.5 \mu\text{m}$ $\lambda = 4.2 \mu\text{m}$ $k = 17$ $w = 1.4 \mu\text{m}$
60.0 nm  0.0 nm			

Figure 7.1 AFM topographic images of representative ring structures.

Patterns formed by evaporation of micro-droplets of G2-50% C_{12} , G3-50% C_{12} , and G4-50% C_{12} in both pentanol and hexanol solutions (all at 0.1 wt %) on mica. The topographic images have been scaled to yield equal diameters on the printed page. The diameter, d , the number of minima in the width of the ring, k , the mean wavelength of the undulation, λ , and the mean width of a dendrimer ring, w , are indicated above each ring.

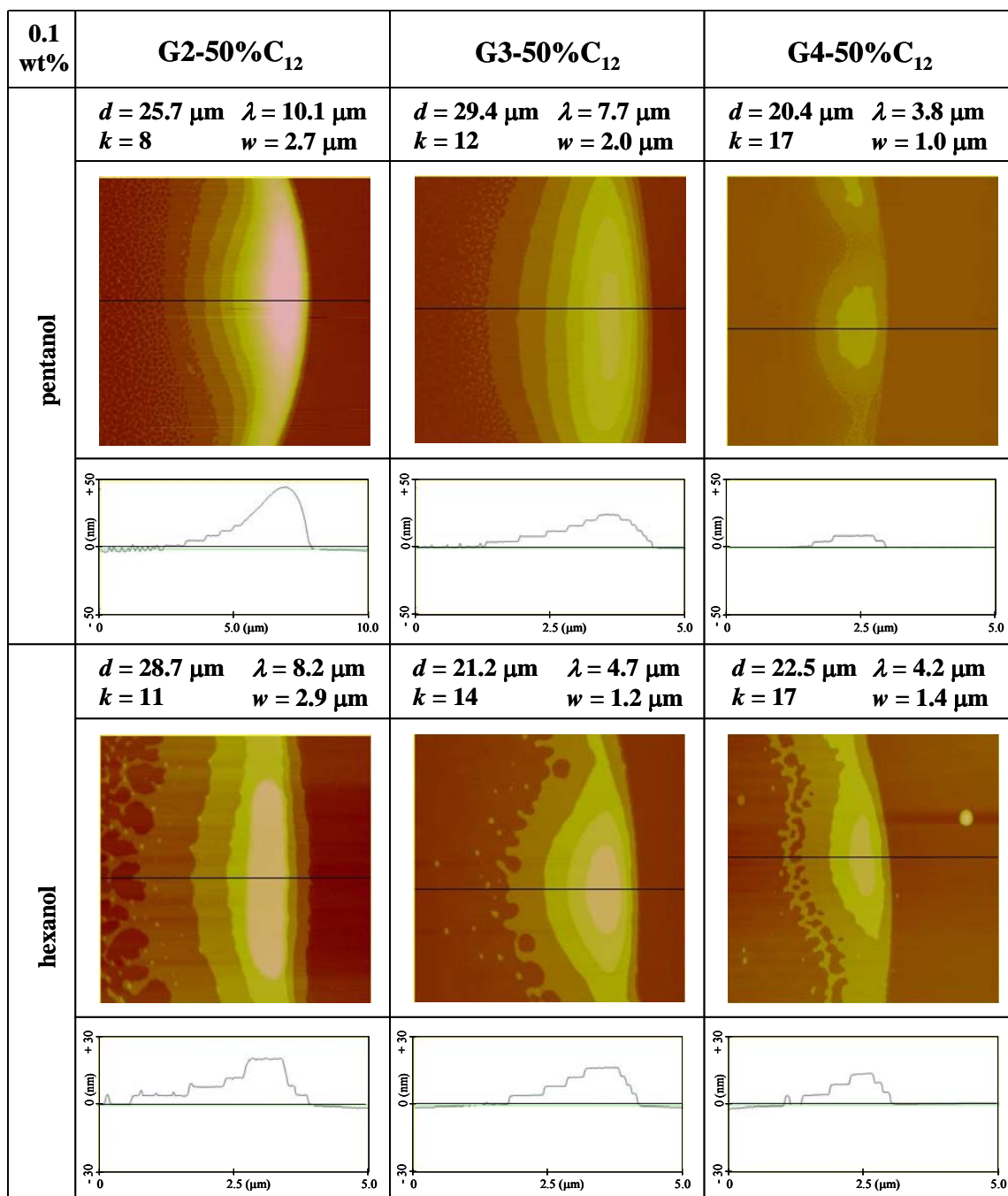


Figure 7.2 Topographic images and radial cross-sections through a representative ‘scallop’.

Images are from each of the rings depicted in Figure 7.1. All topographic images are $5 \mu\text{m} \times 5 \mu\text{m}$ except for G2-50% C_{12} in pentanol which is $10 \mu\text{m} \times 10 \mu\text{m}$.

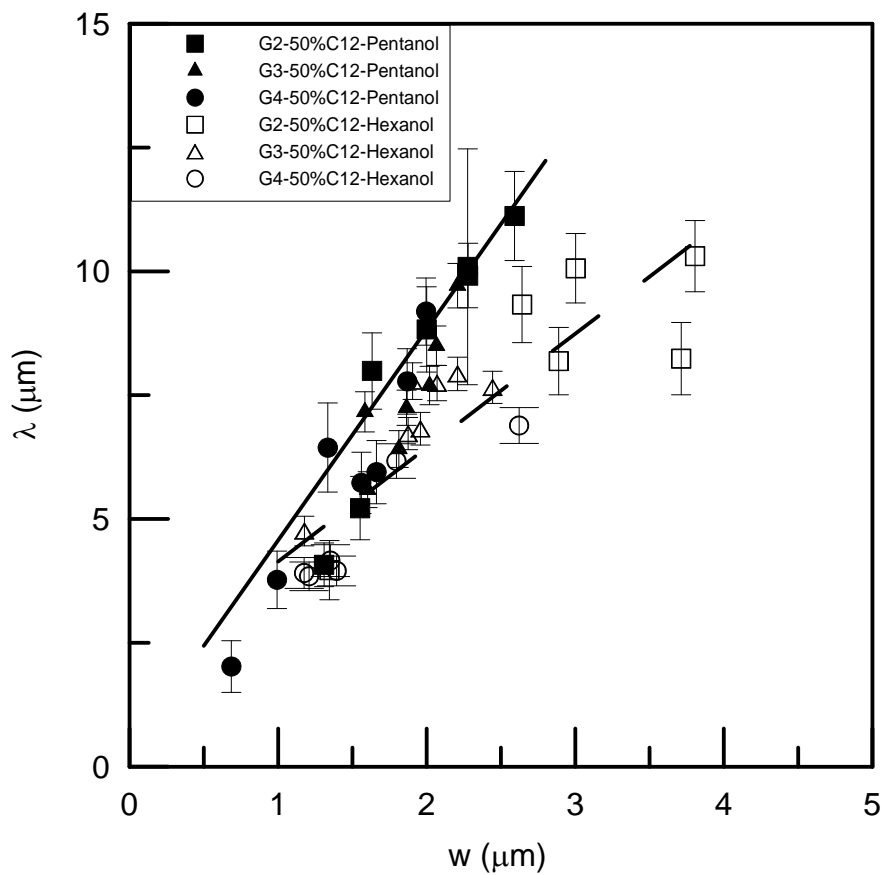


Figure 7.3 Plot of mean wavelength and mean ring width.

Mean undulation wavelength, λ , versus mean ring width, w , for rings from all six dendrimer solutions (all at 0.1 wt %). The data is grouped by solvent (pentanol and hexanol). A line with a slope of 4.8 fits the trend in the data for pentanol-based solutions (solid line) while for hexanol a lower slope of 2.3 is found (dashed line). The error bars indicate \pm one standard deviation in the measured wavelengths.

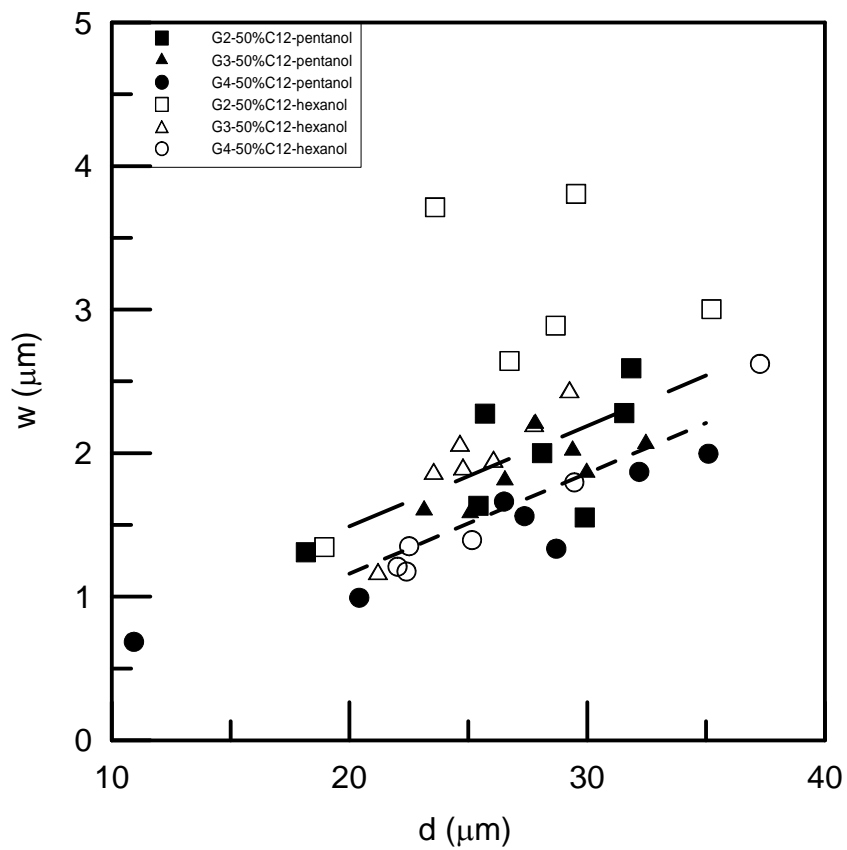


Figure 7.4 Plot of mean ring width and ring diameter.

Mean ring width, w , versus ring diameter, d , for rings from all six dendrimer solutions. For G3-50%C₁₂ and G4-50%C₁₂ solutions lines representing simple linear fits through the data serve as a guide for the eye.

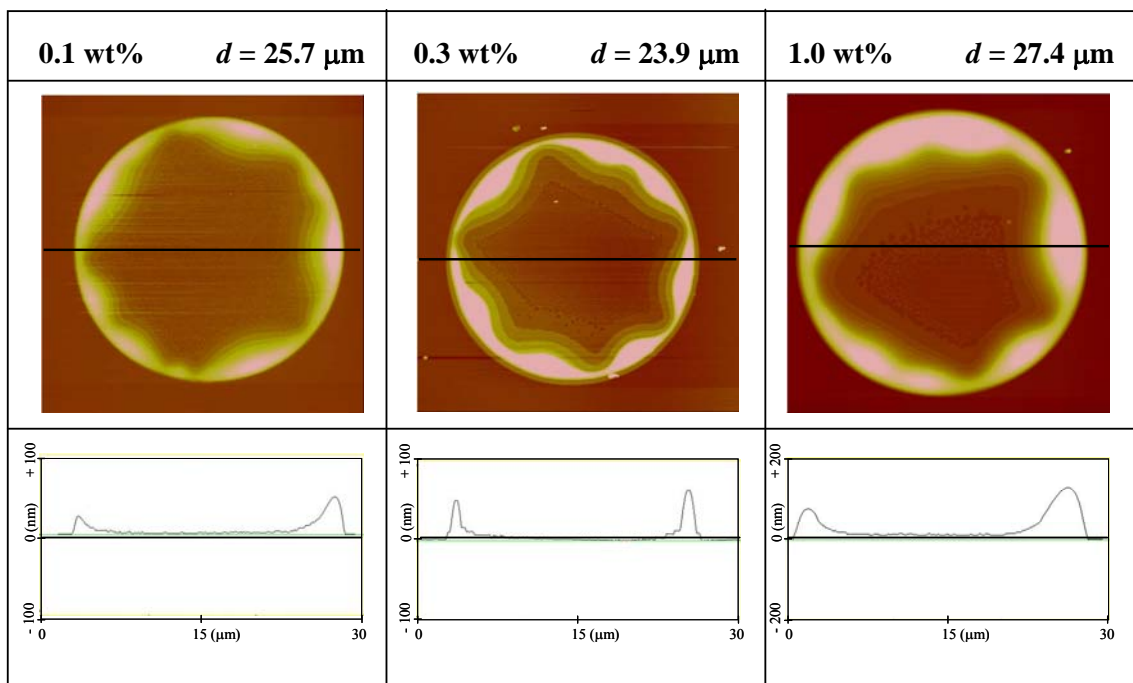


Figure 7.5 Topographic images and radial cross-sections through G2-50% C_{12} .
Pentanol evaporated droplets as a function of concentration (0.1, 0.3, and 1.0 wt %).

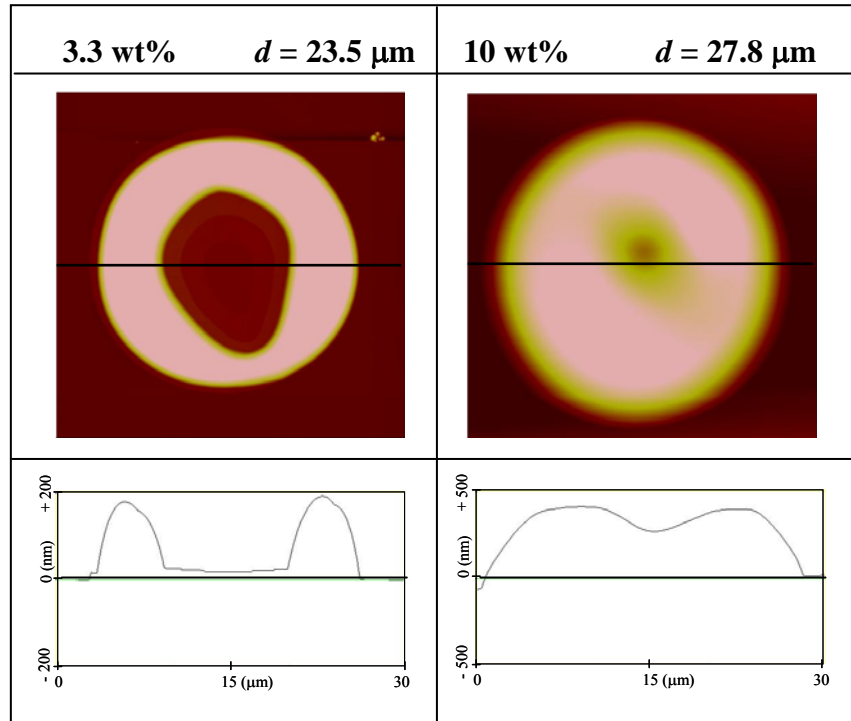


Figure 7.6 Topographic images and radial cross-sections through G2-50% C_{12} . Pentanol evaporated droplets as a function of concentration (3.3 and 10 wt %).

8.0 THERMAL EVOLUTION OF STRATIFIED DENDRIMER RING STRUCTURES

8.1 PRELIMINARY OBSERVATIONS

The scalloping instability described in detail in Chapters 6 and 7 indicates that the growing condensed dendrimer ring should be considered a *phase* rather than simply an aggregate or assembly of particles. This interpretation implies that these structures (unlike the aggregates of discrete particles which dominate the literature) may evolve in interesting ways and produce unique morphologies when subjected to thermal treatment after (or during) evaporation. This Chapter therefore describes the complex, temperature-dependent molecular rearrangements produced by annealing the dried dendrimer structures.

Evidence for the high surface mobility of C₁₂ terminated PAMAM dendrimers (in this case, 0.1 wt % G2-50%C₁₂-hexanol) was first noted when examining scalloped ring structures annealed in air in a simple laboratory oven for one hour at 150°C. This sample had been stored (in ambient conditions) for a number of days after droplet deposition and evaporation and the annealing treatment was only expected to produce, perhaps, a small change in topography due to densification of the dendrimer layers. The dramatic rearrangements described below came as a great surprise. In Figure 8.1 the as-deposited scalloped ring structure, as well as a representative section through an individual scallop, reveal the terraced dendrimer structure associated with monolayer by monolayer growth. In Figure 8.2 a typical ring structure (in both topographic and

3-D views) illustrates the very substantial molecular rearrangements induced by the annealing treatment. Magnified topographic images and corresponding cross-sectional scans of this ring are found in Figure 8.3. Note that in this case the as-deposited ring of Figure 8.1 and the annealed ring of Figure 8.2 are from the same sample but are not the same ring; however, they are completely representative of the changes in all of the rings produced by annealing.

A number of key preliminary conclusions can be drawn from these initial observations. In examining the ring structure as a whole Figure 8.2 indicates that some of the dendrimer molecules originally organized in a stratified structure have rearranged themselves into circular islands with smoothly curved surfaces which are shown below to be spherical caps. A large island sits near the center of each scallop, while much smaller satellite islands are found at the boundary between two adjacent scallops. The contrast in the image also makes clear that the dendrimer molecules which are most mobile and have aggregated into islands are drawn from layers above the first monolayer (the first monolayer, which is in intimate contact with the mica substrate has remained stable during this annealing treatment). The ring structure has clearly coarsened, with lower surface to volume ratio islands replacing layered structures.

Consider the magnified topographic image ($10\ \mu\text{m} \times 10\ \mu\text{m}$) and cross section through an individual island after annealing (Figure 8.3a, b). This droplet has a nearly circular base with a diameter of $\sim 1.85\ \mu\text{m}$ and a height of $\sim 62\ \text{nm}$ (measured from the top of the monolayer which surrounds the island). There is no evidence for layering in the islands – the surface is smoothly curving. Rescanning the region between scallops at $5\ \mu\text{m} \times 5\ \mu\text{m}$ (Figure 8.3c and d) the roughness at the edge of the monolayer is apparent (compare to Figure 8.1). One might speculate that dendrimer molecules have diffused from the edge up onto the top of the first monolayer and then across the first monolayer to join the growing island, leaving behind edges

which are rough at the molecular scale. Notice that the outer edge (the original pinned perimeter of the drop) is also now rough at the same scale. Similar measurements on the *same* ring before and after annealing will clarify this behavior and are described below. Note also the presence of a small concentration of very small ‘holes’ in the annealed monolayer, again likely due to individual dendrimers diffusing out of the monolayer to join a growing island. The finite width of the AFM tip (~ 10 nm radius) makes it impossible to confirm with certainty that the ‘holes’ are the result of missing molecules and thus go through the monolayer all the way to the substrate. Finally, this annealing treatment has in fact increased the density of the first monolayer – the thickness is ~ 3 nm compared to ~ 3.8 nm in the as-deposited state.

A second similar experiment was carried out on pentanol based droplets (0.1 wt % G2-50% C_{12} -pentanol) annealed at a series of temperatures for one hour. Again the samples had been stored for several days prior to annealing and the as-deposited and annealed images are all from different rings. The incremental nature of the coarsening process is revealed in Figure 8.4. In the as-deposited state (Figure 8.4a) we see the typical stratified structure in the scallop. In this particular example the stratification does not persist to the top of the scallop; the section becomes smoothly rounded above the fifth terrace. After annealing at 80 °C for one hour the onset of the dissolution of the terrace edges is clear and the layered structure is beginning to break down (Figure 8.4b). Annealing at 100 °C (Figure 4c) was not yet sufficient to entirely absorb the second layer of the stratified structure and the incomplete development of the circular islands is quite clear (at this stage coexisting with a two layer structure). Finally at higher temperatures (150 °C, Figure 4d) the second monolayer fully dissolves at the expense of the growing circular island.

The shape of the islands formed by annealing was found to be very closely approximated by a spherical cap. A comparison of the ideal spherical cap shape, calculated based on the experimental height and diameter of the island in Fig. 8.4d, and the actual AFM cross-sectional scan shows extremely close agreement (Figure 8.5). This close correspondence will allow for analysis of the size dependent contact angle in these systems (see below).

Having demonstrated almost fortuitously that G2-50%C₁₂ scalloped rings undergo complex rearrangements when annealed in air at modest temperatures, a more reproducible experimental protocol for studying this behavior in greater detail was developed. In the course of carrying out a number of preliminary annealing experiments on a variety of samples it became clear that the stability of the ring structures was a sensitive function of the length of time the freshly evaporated ring structures were held at room temperature prior to the annealing treatment. Storing the samples prior to annealing apparently stabilized their structure and significantly increased the temperature required to induce large scale molecular rearrangements (island formation). In Figure 8.6 a sequence of AFM topographic images and cross sections of an individual scallop from a 0.1 wt % G3-50%C₁₂ sample are presented which illustrate the subtle rearrangements that occur at room temperature over the course of 30 hours. Measuring the long axis of the third and fourth layers it is clear that these roughly elliptical monolayers are contracting with time as dendrimer molecules rearrange themselves to reduce the number of molecules in the highest curvature locations. The third (and fourth) layer systematically decreases in length from 9.95 μm to 9.36 μm to 8.56 μm (8.27 μm to 7.83 μm to 7.11 μm). The gradual widening of the region between two adjacent scallops is also apparent. Note also in the cross-sections the gradual dissolution of the topmost (eighth) layer which caps the scallop.

The early experimental results described above in Figures 8.1 – 8.4 were based on samples that had been stored for several days prior to annealing. Thus the temperatures used were considerably higher than are needed for the ‘fresh’ samples which will be described below. In addition, comparing similar but not identical ring structures, before and after annealing, yields global trends but does not allow for direct analysis of local molecular rearrangements. Finally, the use of a conventional laboratory oven with its comparatively large volume and slow temperature changes limited experimental flexibility. New experimental procedures were developed to address these problems. In order to have a standard reference state for studying relative stability, the samples discussed below (unless otherwise stated) were imaged immediately after evaporation (the as-deposited state) and then annealed within one hour of droplet deposition and evaporation using a digital hotplate. A standard glass Petri dish was inverted on the hotplate preset at the temperature of interest. Samples were slipped under the edge of the Petri dish in direct contact with the aluminum block of the hotplate, and removed as soon as the desired annealing time was reached. Therefore the annealing history of the samples discussed below is essentially isothermal, with very rapid heating and cooling transitions. Spatial coordinates and registration marks were used to find and image the same rings in the as-deposited and annealed states.

8.2 THERMAL STABILITY AND MOLECULE SIZE

With a new protocol in place a comparative study of the annealing behavior of scalloped ring structures made from 0.1 wt % solutions of G2-, G3-, and G4-50% C_{12} PAMAM dendrimer molecules in pentanol was carried out. These dendrimers have theoretical molecular weights of

6205, 12807, and 26011 amu, respectively. Our expectation, borne out below, was that larger molecules should exhibit greater stability and require higher temperatures to induce rearrangement. The following criterion was developed to establish a critical temperature, T_c , for these systems. T_c is defined as the temperature at which a 5 minute anneal of a freshly prepared sample will lead to molecular rearrangements which fully remove all dendrimer layers above the first monolayer (which is much more tightly bound by its interaction with the mica substrate, and thus less mobile) and create dendrimer islands with essentially circular perimeters consistent with the spherical cap geometry. T_c was determined for each molecule in preliminary annealing experiments. For G2-50% C_{12} $T_c = 348K$ (75°C), for G3-50% C_{12} $T_c = 368K$ (95°C), and for G4-50% C_{12} $T_c = 403K$ (130°C). The systematic increase in T_c with generation number tracks the increase in dendrimer size, molecular weight, and the dramatic increase in areal density of surface sites.¹⁶ The increase in surface site density translates to stronger adhesion to the mica substrate. For the complete analysis a representative ring for each dendrimer molecule was identified and imaged by AFM in the freshly evaporated (as-deposited) state. This ring was then imaged following annealing at a given temperature for varying lengths of time (initially 5 minutes followed by annealing at the same temperature for 25 and then 30 additional minutes). Finally, the ring was imaged again after 24 hours at room temperature. The annealing treatments are designated AD (as-deposited), 5 min, 30 min, 60 min, and 60 min + 24 h @ RT. We consider in order the behavior of droplets made from a 0.1 wt % solution of G2-50% C_{12} , G3-50% C_{12} , and G4-50% C_{12} PAMAM dendrimer molecules in pentanol at five different annealing temperatures (0.9, 0.95, 1.0, 1.05, and 1.1 T_c). The behavior of the three dendrimer molecule sizes at five different temperatures is displayed in the following 15 figures. In each figure the top row

displays the full ring, the middle row a magnified image (10 μm x 10 μm) of an individual scallop, and the bottom row a section through the scallop.

8.2.1 G2-50% C_{12}

In Figure 8.7 the temporal evolution of a typical scalloped ring structure annealed at 0.9 T_c (313K, 40°C) is depicted. The initial 5 min anneal is sufficient to move all the molecules from the terraced structure (except for the first monolayer) to the growing islands. However, the islands (which coincide with the scallops) have not consolidated into circles but remain highly elongated. By 30 min several small islands at the junctions of the scallops have ‘pinched off’ as the migration away from high curvature locations continues. At 60 min little has changed; the islands are still elongated and the first monolayer is still intact. The measurement made 24 h later shows little change. Even at this low temperature there is substantial rearrangement leading to the removal of the terraced structure (only the first layer remains) and creation of a smoothly curved islands. The islands are still highly elliptical at the end of the experiment, reflecting the scallop shape from which they are formed. The outer perimeter of the ring remains quite smooth throughout the process.

At 0.95 T_c (331K, 58°C) the initial 5 min anneal again transforms the layered structure into a single monolayer coexisting with rounded but elongated islands (Fig. 8.8). As the annealing continues the islands evolve into nearly circular forms. Subtle rearrangements are still occurring during the 24 h at room temperature before acquisition of the final image. However the islands are not yet circular and thus this temperature falls below T_c . Note that the morphology of the first monolayer is remarkably constant throughout – the small-scale

convolutions are reproduced at each stage of the annealing process, again illustrating the comparatively strong bonding between this first monolayer and the mica substrate. The outer perimeter of the ring again remains smooth.

At T_c (348K, 75°C) 5 min at T_c completely transforms the structure as all of the dendrimers above the first monolayer melt and collect in circular islands at each scallop (Fig. 8.9). The islands are, in fact, spherical caps. At T_c the first monolayer is very slightly less stable than it was at $0.95 T_c$. This can be seen in the nucleation gradual growth of the trio of small holes indicated in the second, third, fourth, and fifth panels of the middle row. This temperature is also sufficient to induce some roughening of the perimeter of the ring but the first monolayer remains essentially intact and in equilibrium with the islands.

At $1.05 T_c$ (365K, 92°C) the 5 min anneal produces fully circular islands but also significantly degrades both the first monolayer (which has been stable up to this temperature) and the perimeter of the ring (Fig. 8.10). By 30 min the first monolayer is also peppered with very small holes which grow slightly over time. The most substantive changes have occurred by the 30 min mark. Finally at $1.1 T_c$ (383K, 110°C) behavior quite similar to $1.05 T_c$ is observed (Fig. 8.11).

8.2.2 G3-50%C₁₂

In Figure 8.12 the temporal evolution of a typical scalloped ring structure annealed at $0.9 T_c$ (331K, 58°C) is depicted. The 5 min anneal begins to pull molecules from the terraced structure and the height at the scallop center grows. By 30 min all molecules above the 3rd monolayer

have joined the islands which are now well-rounded in profile, as seen in the radial section. At 60 min the 3rd monolayer is essentially gone and the island heights increases slightly. Interestingly, the measurement made 24 h later reveals that the 2nd monolayer has now essentially dissolved. While there is clearly substantial rearrangement leading to the gradual degradation of the terraced structure and creation of smoothly curved islands, the island is still highly elliptical at the end of the experiment, reflecting the scallop shape from which it is formed. An unusually large decrease in height of the island in the final cross section is noted. The outer perimeter of the ring is quite smooth throughout the process.

At $0.95 T_c$ (350K, 77°C) the as-deposited ring structure selected for study is especially well terraced, with 6 monolayers clearly visible in the cross section (Fig. 8.13). The initial 5 min anneal causes the dissolution of all layers above the first monolayer and the formation of rounded islands. However the islands are not yet circular and thus this temperature is just below T_c . At 30 min the islands are essentially circular and this morphology is preserved at 60 min and after 24 h. Note that the morphology of the first monolayer is remarkably constant throughout – the small-scale convolutions are reproduced at each stage of the annealing process, again illustrating the comparatively strong bonding between this first monolayer and the mica substrate. The outer perimeter of the ring again remains smooth.

At T_c (368K, 95°C) the as-deposited ring structure is again well terraced, with 6 monolayers visible in the cross section (Fig. 8.14). 5 min at T_c completely transforms the structure as all of the dendrimers above the first monolayer melt and collect in circular islands at each scallop. The islands are, in fact, spherical caps. At T_c the first monolayer is very slightly less stable than it was at $0.95 T_c$. This can be seen in the gradual growth of small hole indicated by the heavy arrow. One also can observe what appears to be the creation of several small holes

in the first monolayer during the 24 h period at room temperature (light arrows). This temperature is sufficient to induce some roughening of the perimeter of the ring.

Annealing for 5 min at $1.05 T_c$ (386K, 113°C) produces fully circular islands but also significantly degrades the perimeter of the ring (Fig. 8.15). Compared with G2 at $1.05 T_c$ the first monolayer is more stable here. Note that the dispersion of small dendrimer domains that lie in a band at the interior edge of the ring diffuses away during the 24 h at room temperature. Although it is difficult to resolve at this scale but the first monolayer is also peppered with very small holes following the 24 h hold. Finally at $1.1 T_c$ (405K, 132°C) we see quite similar behavior to that observed at $1.05 T_c$ (Fig. 8.16).

8.2.3 G4-50%C₁₂

The G4-based rings structures all had highly stratified structures in the as-deposited state (more so than for G2 and G3). In Figure 8.17 the evolution of a typical scalloped ring structure annealed at $0.9 T_c$ (363K, 90°C) is depicted. The as-deposited state has 4 distinct layers. The 5 min anneal begins to pull molecules from the terraced structure and the height at the scallop center grows. By 30 min all molecules above the second monolayer have joined the islands which are now well-rounded in profile, as seen in the radial section. Very little changes beyond this point. The measurement made 24 h later does reveal that small holes have formed in the first monolayer. While there is substantial degradation of the terraced structure and creation of smoothly curved islands, the islands are still highly elliptical at the end of the experiment, and the second monolayer has not yet melted. The outer perimeter of the ring is quite smooth throughout the process.

At $0.95 T_c$ (383K, 110°C) the as-deposited ring structure selected for study has five monolayers clearly visible in the cross section through the center of a scallop (Fig. 8.18). The initial 5 min anneal causes the dissolution of all layers above the first monolayer and the formation of rounded but highly elongated islands coincident with each major scallop, along with a number of satellite islands. Although some small changes can be noted on close inspection, the structure after 5 min anneal is essentially preserved throughout 60 min anneal (small holes are found again after 24 h). The morphology of the first monolayer is remarkably constant - the small-scale convolutions at inner edge of the ring are preserved at each stage of the annealing process, again illustrating the comparatively strong bonding between this first monolayer and the mica substrate and stability of the layer as a whole. At this temperature the outer perimeter of the ring again remains smooth.

At T_c (403K, 130°C) the as-deposited ring structure is again well terraced, with 4 monolayers visible in the cross section (Fig. 8.19). In accordance with our definition, 5 min at T_c completely transforms the structure as all of the dendrimers above the first monolayer melt and collect in circular islands at each scallop. For this ring only two satellite islands are noted (between the six and seven o'clock position on the ring). Between 5 min and 60 min the island height decreases, perhaps due to time dependent densification processes occurring as the dendrimers in the islands accommodate themselves in a viscous fluid state. However, the island diameters do not change during this stage. At T_c the first monolayer appears quite stable except for the very small holes which appear in the first monolayer after 24 h. The perimeter remains quite smooth.

Annealing for 5 min at $1.05 T_c$ (423K, 150°C) again produces nearly circular islands from a well-terraced as deposited state (Fig. 8.20). Compared with G2 at $1.05 T_c$ the first

monolayer is again more stable here. Note that the dispersion of small dendrimer domains that lie in a band at the interior edge of the ring gradually diffuses away during annealing sequence. Although it is difficult to resolve at this scale but the first monolayer is also peppered with very small holes starting at the 60 min mark. Holding at $1.05 T_c$ for 60 min again leads to densification of the island. The densification of the island is more noticeable in G4 than G3 or G2. We suspect that this may be related to the fact that areal density of surface sites increases significantly with generation number¹⁹. Thus the hydroxydodecyl surface group chains are more crowded in G4. The time-dependent interdigitation of chains from neighboring dendrimer molecules gradually brings them closer together. In G3 and G2 the more open structure may allow for rapid, nearly full densification on melting. At this temperature, the width of the first monolayer actually decreases by roughly 10% by 60 min due to dissolution/diffusion of the inner edge. Finally at $1.1 T_c$ (443K, 170°C) the first monolayer begins to dissolve more rapidly and the outer perimeter actually breaks at its thinnest points (Fig. 8.21). At this high temperature the small holes in the first monolayer grow and become a significant fraction of the layer area.

8.3 TIME DEPENDENT STABILIZING EFFECT ON RING STRUCTURE

Before considering the dependence of island contact angle on island size we briefly elaborate on the stabilizing effect of holding the samples at room temperature before annealing. In Figure 8.22 a direct comparison of ‘fresh’ and stabilized samples is made for G3-50% C_{12} samples at T_c . In the top half of the figure the annealing sequence up to 60 minutes for a freshly annealed sample is reproduced showing the complete transformation to the monolayer plus island structure in 5 minutes. In the bottom half of the figure a different ring from the same solution was

stabilized at room temperature for 24 hours prior to exposure to the same annealing sequence. The stabilizing effect is dramatic. Annealing for 5 minutes following stabilization only begins to round the scallop tops above the 3rd monolayer and these rounded regions remain highly elongated even out to 60 minutes. There is little change in the ‘stabilized’ morphology except for the initial rounding. The first three monolayers are clearly preserved even at 60 min.

8.4 DEPENDENCE OF ISLAND CONTACT ANGLE ON CONTACT LINE CURVATURE

An unexpected byproduct of these annealing studies was the opportunity to carry out an investigation of the very interesting problem of the size dependence of the contact angle (and thus the quantity known as the contact line tension) in a unique thermodynamic system. Perhaps the most common geometry encountered in such studies is a sessile liquid droplet of one material on a flat, homogeneous solid substrate of another material, in equilibrium with its vapor phase. In our case annealing at a sufficient temperature causes the melting of dendrimers above the first monolayer and formation of a dendrimer island with a spherical cap shape on top of the dendrimer monolayer. The schematic in Figure 8.23 illustrates the equilibrium between the liquid dendrimer island phase and the solid dendrimer monolayer phase (which resides on the mica substrate). In this case there is no ‘foreign’ solid substrate but rather a 2D solid form of the liquid dendrimer. The interaction of the monolayer dendrimer molecules with the mica substrate stabilizes them in the solid state at temperatures high enough to cause melting of the dendrimers that are not in contact with the mica. The atypical geometry found in Figure 8.23 may be viewed as a special type of partial self-wetting¹²⁰⁻¹²². In classic partial self-wetting the liquid and solid

phases of the same material are properly ‘bulk’ in form. Typically the liquid drop is in contact with a specific low index surface of a single crystal solid. In our system the solid dendrimer is of reduced dimension (a monolayer) and its properties are clearly influenced by the interaction with the mica substrate.

Experimental contact angles for a range of island sizes for all three molecules (G2-, G3-, and G4-50%C₁₂) were deduced from AFM measurements of the contact line radius a , and maximum island height h , under the assumption of a spherical cap geometry, i.e., $\cos \theta = (a^2 - h^2)/(a^2 + h^2)$. All of the islands were formed by annealing for 5 minutes at the T_c appropriate for each molecule. The ideal spherical cap profile was also determined using a , h , and the equation for a circle. A comparison of the AFM profile and the ideal spherical cap profile for a representative island from each molecule is plotted in Figure 8.24. AFM images of the islands with the section lines used appear as inserts in the plots. The agreement between the AFM profile and the ideal form is found to be very good over the whole profile, including near the three-phase line, giving us confidence that the contact angle values are reliable.

The contact angle, θ , at small scales depends not only on the solid-vapor, solid-liquid, and liquid-vapor interfacial tensions (γ) but also on the local three-phase contact line curvature and line tension, τ . For circular contact lines of radius a , one can write a modified Young equation:

$$\cos \theta = (\gamma_{sv} - \gamma_{sl})/\gamma_{lv} - (\tau/\gamma_{lv}a) = \cos \theta_{\infty} - (\tau/\gamma_{lv}a)$$

By plotting measured $\cos \theta$ versus $1/a$, both $\cos \theta_{\infty}$ and the ratio τ/γ_{lv} can be extracted from a linear fit to the data. Our experimental situation has unique advantages in the sense that the droplet forms ‘intrinsically’ from dendrimer molecules already present above the first

monolayer, which melt and contract to form spherical caps. This exposes pristine, previously buried, monolayer regions and creates the three phase contact line. This is quite different from either placing droplets onto a foreign substrate or nucleating them via condensation (the latter method very likely is particularly skewed by preferential nucleation at surface defects)

The measured $\cos \theta$ are plotted versus $1/a$ for all three dendrimer molecule types in Figure 8.25. The linear behavior over this range of droplet sizes is quite evident. The positive slope implies a negative τ in this system. No values are available for γ_{lv} in this system so τ cannot be quantified. However, from the slopes of the fits the length scale of the interaction c can be determined, as well as the macroscopic contact angle, θ_∞ . These values are tabulated in Figure 8.25. There is a systematic dependence on dendrimer molecule size with c and θ_∞ decreasing in the order $G2 \rightarrow G3 \rightarrow G4$ (as the molecule size and number of terminal sites increases). The large change in c and θ_∞ for G4 broadly correlates with the comparatively large jump in T_c for G4. The trends noted here can be understood as consistent with substrate adhesion increasing with generation number thus lowering the macroscopic contact angle. As adhesion increases (tracking the dramatic increase in areal density of surface sites) the relative importance of τ declines. Absent quantitative information on γ_{lv} as a function of generation number, at this stage one cannot determine how the magnitude of τ varies with dendrimer generation.

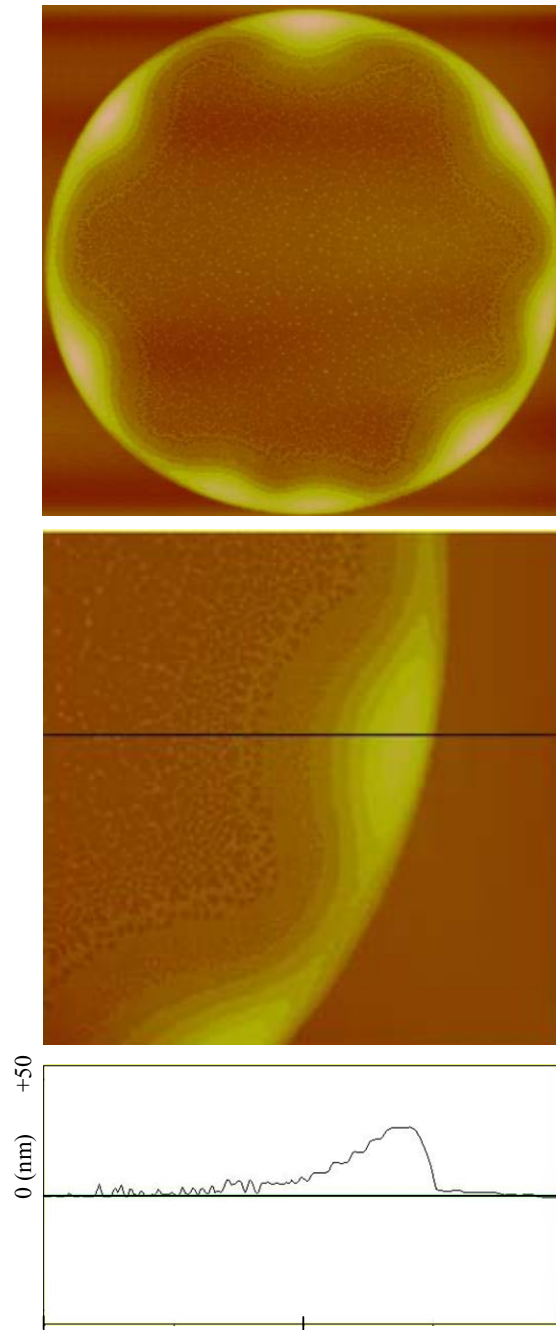
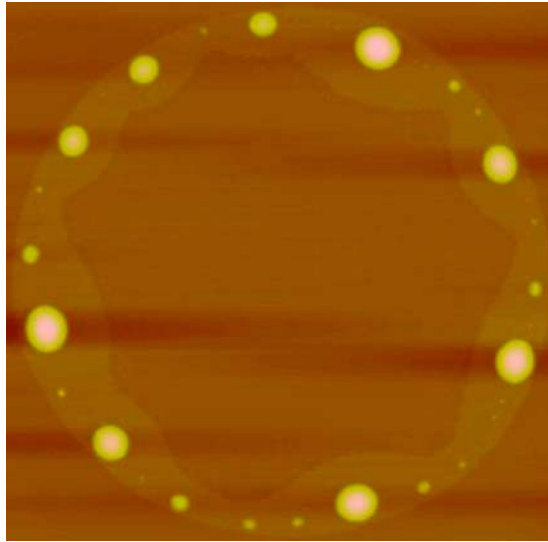
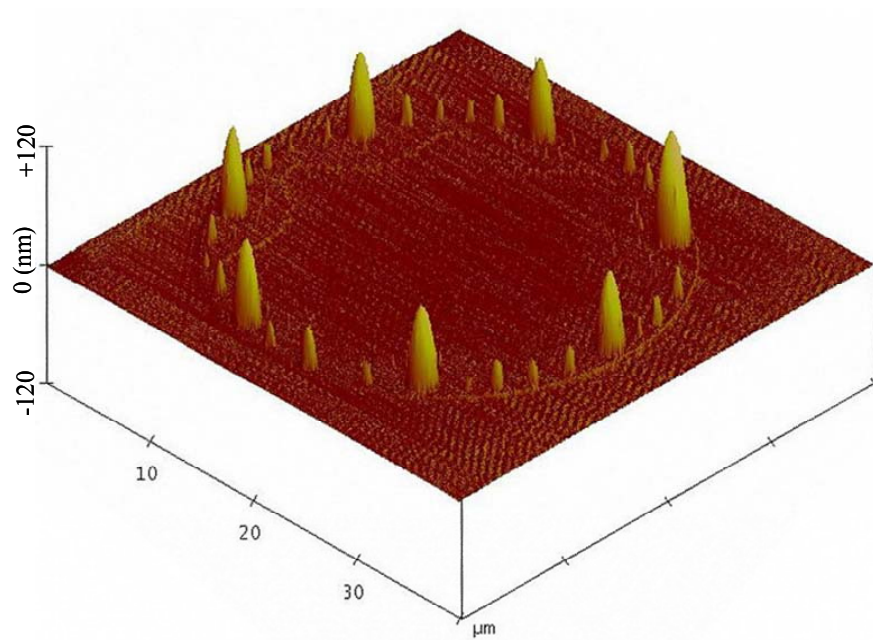


Figure 8.1 The as-deposited scalloped ring structure.

The ring structure and a representative section through an individual scallop.



(a)



(b)

Figure 8.2 AFM topographic images of G2-50%C₁₂ ring structure.

(a) after annealing in air in a simple laboratory oven for one hour at 150°C (b) 3 dimensional view of (a).

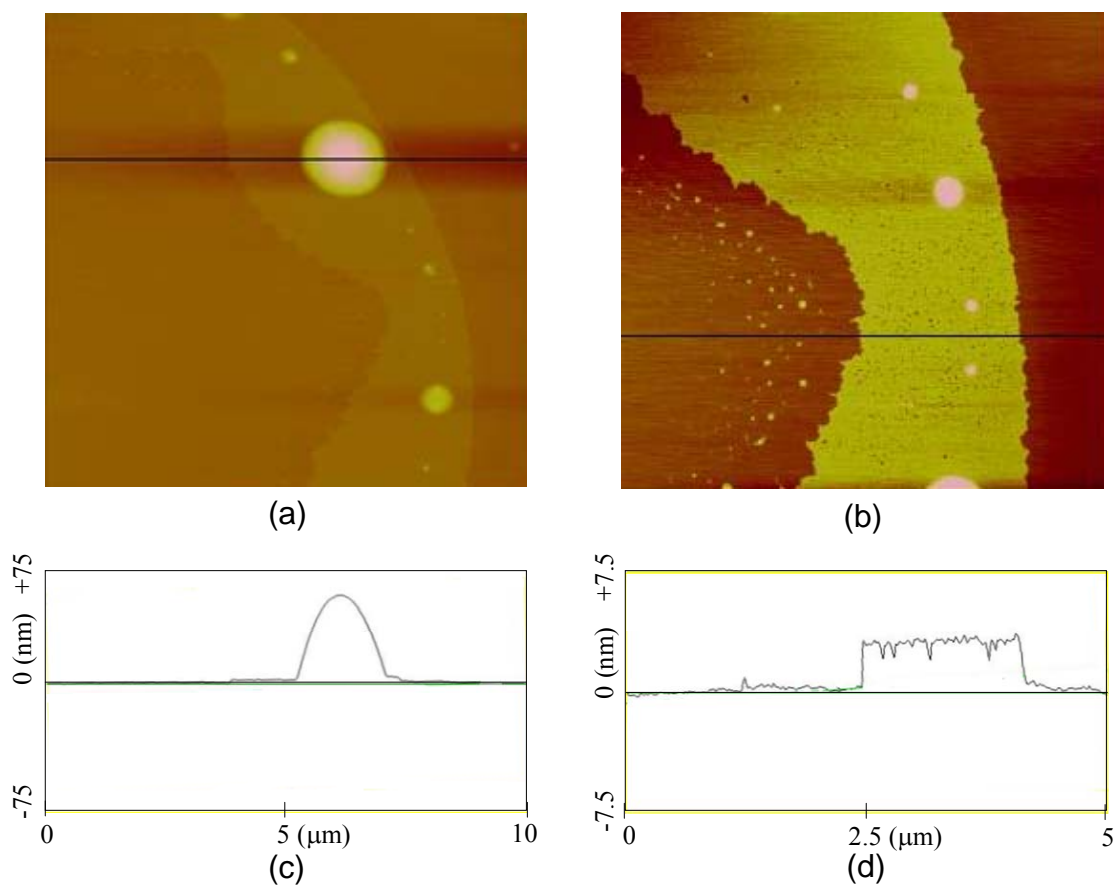


Figure 8.3 AFM topographic images of G2-50% C_{12} ring structure.

Magnified topographic images and corresponding cross-sections of the ring structure in figure 8.2 (a) (b) 10 μm x 10 μm scan (c) (d) 5 μm x 5 μm scan of the region between scallops.

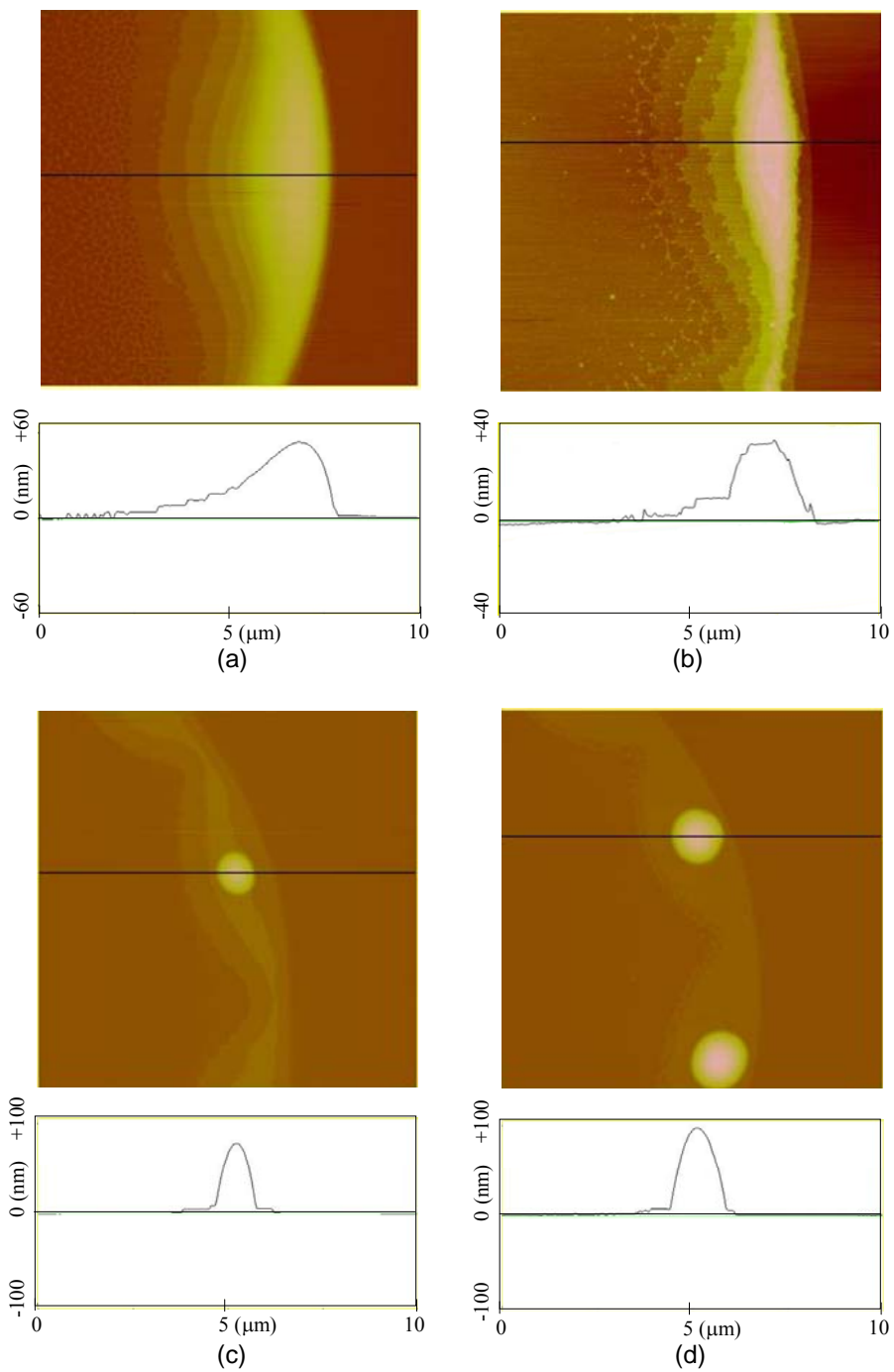


Figure 8.4 Annealing sequence for G2-50%C₁₂ ring at different temperatures.

(a) as-deposited (b) annealing at 80°C for an hour (c) annealing at 100°C for an hour (d) annealing at 150°C for an hour.

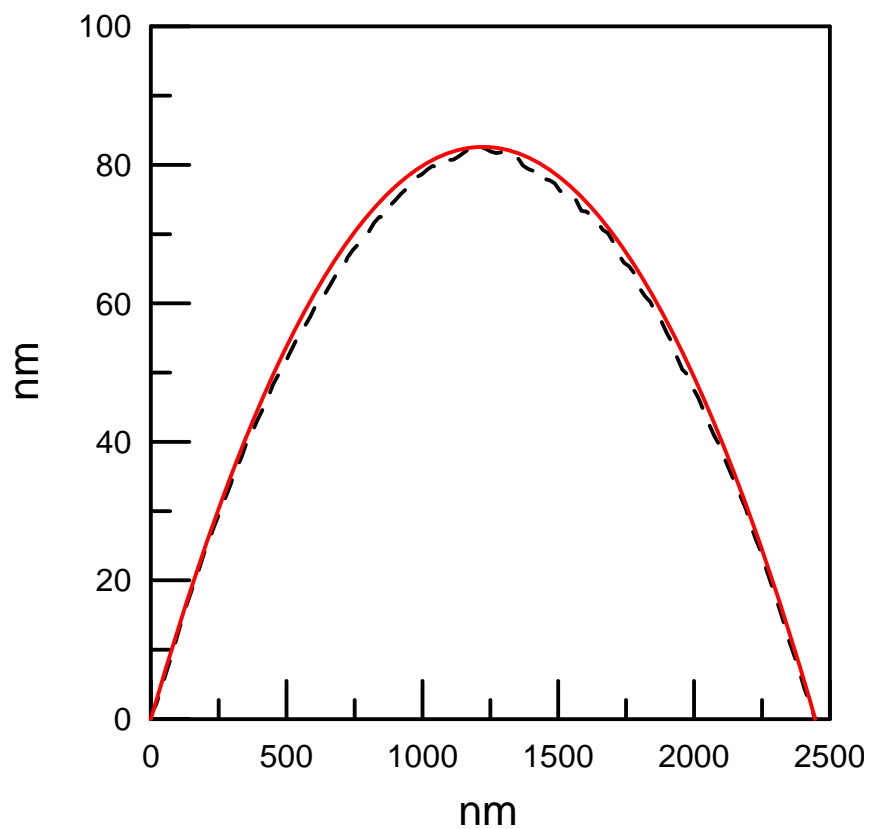


Figure 8.5 Comparison of ideal spherical cap profile and AFM profile.

The ideal spherical cap profiles (solid lines) and the measured AFM profile(dashed line) for dendrimer island of G2-50%C₁₂.

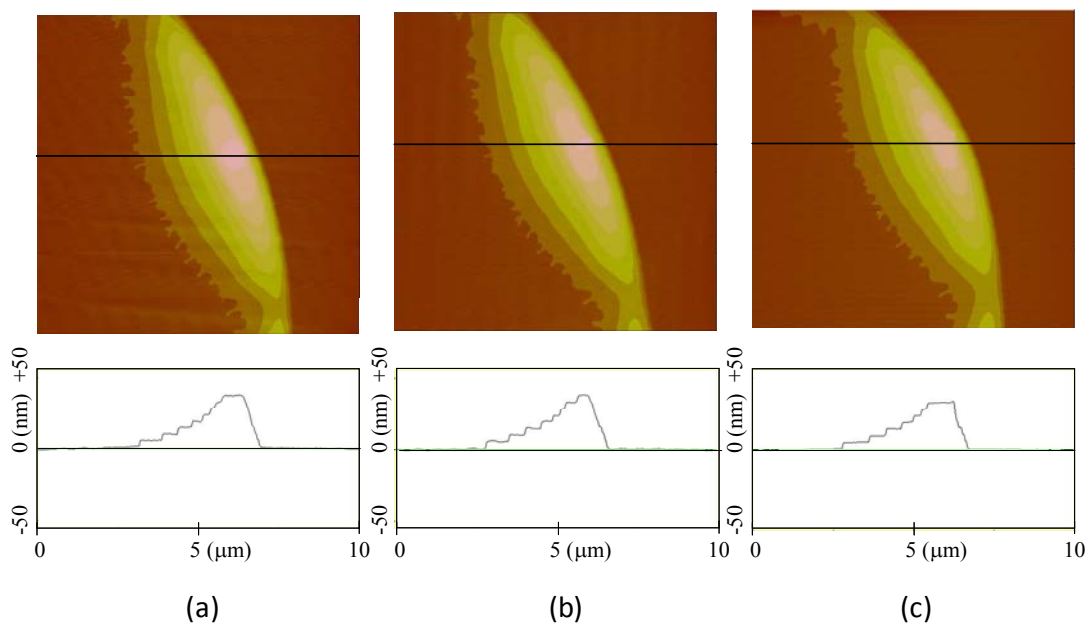


Figure 8.6 AFM topographic images and cross sections of an individual scallop.

(a) 30 minutes after deposition (b) 4 hours after deposition (c) 30 hours after deposition of a 0.1 wt % G3-50%C₁₂ sample

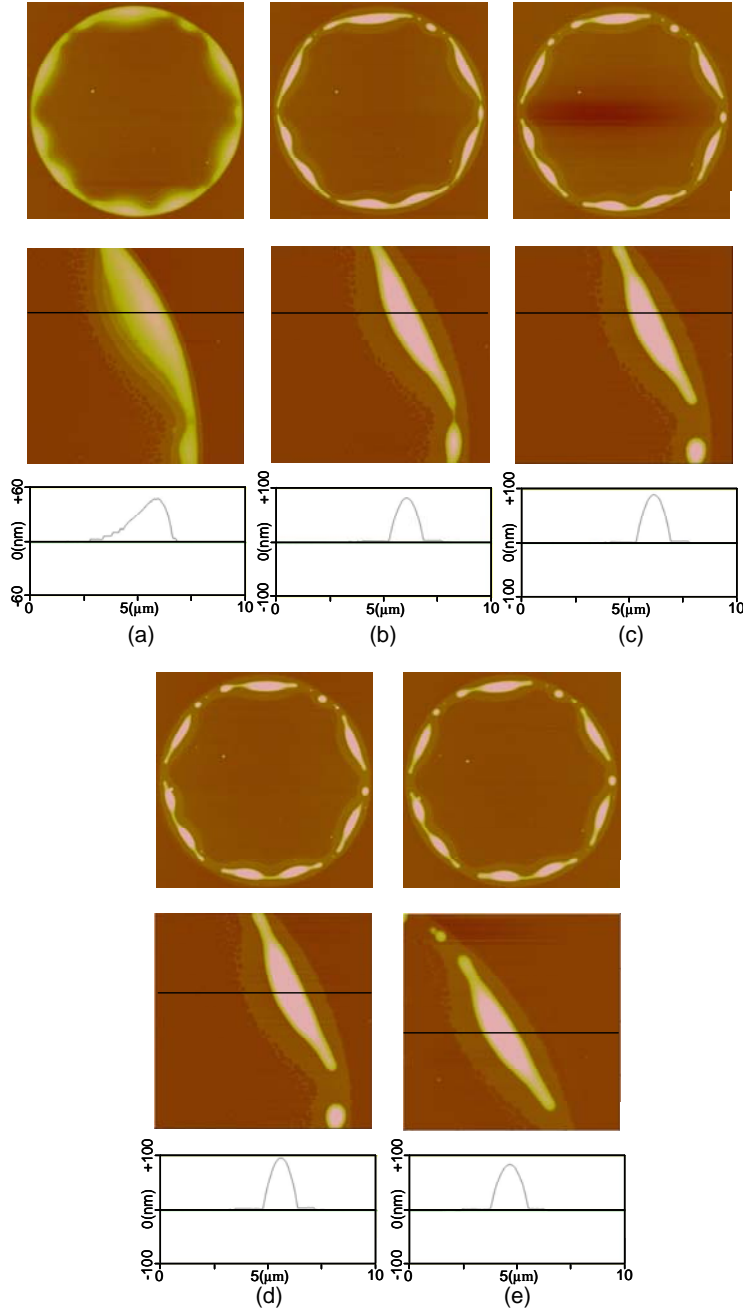


Figure 8.7 Annealing sequence for G2-50% C_{12} ring ($d=27.7 \mu\text{m}$) at $0.9 T_c$ (313K, 40°C).

(a) as deposited (b) 5 minutes at 40°C (c) 30 minutes at 40°C (d) 60 minutes at 40°C (e) 24 hours after annealing at 40°C . Top: topographic images of full rings; middle: topographic images of ring segment at ‘3-o’clock’ position; bottom: radial cross-sectional scans through representative ‘scallop’. The topographic images of the full rings are scaled to yield equal diameters on the print page. The ‘middle’ images are $10 \mu\text{m} \times 10 \mu\text{m}$

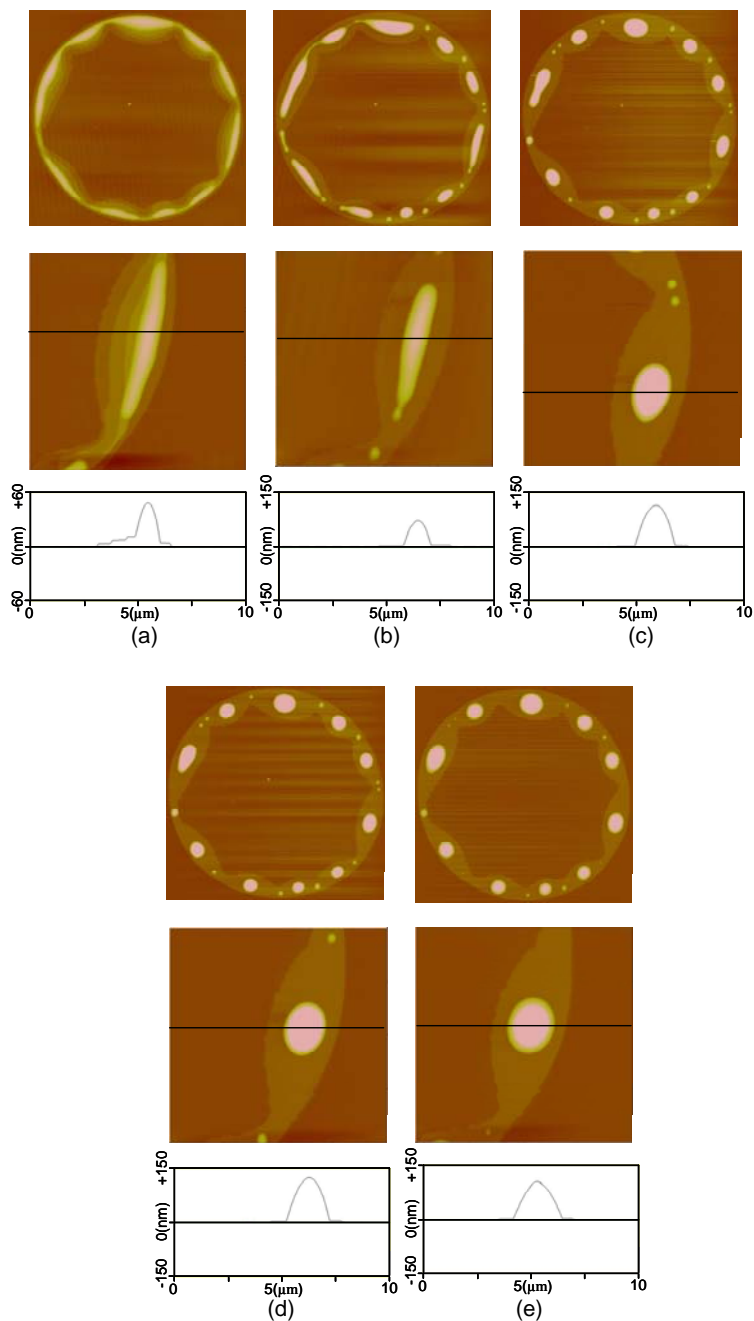


Figure 8.8 Annealing sequence for G2-50% C_{12} ring ($d=27.13 \mu\text{m}$) at $0.95 T_c$ (331K, 58°C).

(a) as deposited (b) 5 minutes at 58°C (c) 30 minutes at 58°C (d) 60 minutes at 58°C (e) 24 hours after annealing at 58°C . Top: topographic images of full rings; middle: topographic images of ring segment at ‘3-o’clock’ position; bottom: radial cross-sectional scans through representative ‘scallop’. The topographic images of the full rings are scaled to yield equal diameters on the print page. The ‘middle’ images are $10 \mu\text{m} \times 10 \mu\text{m}$.

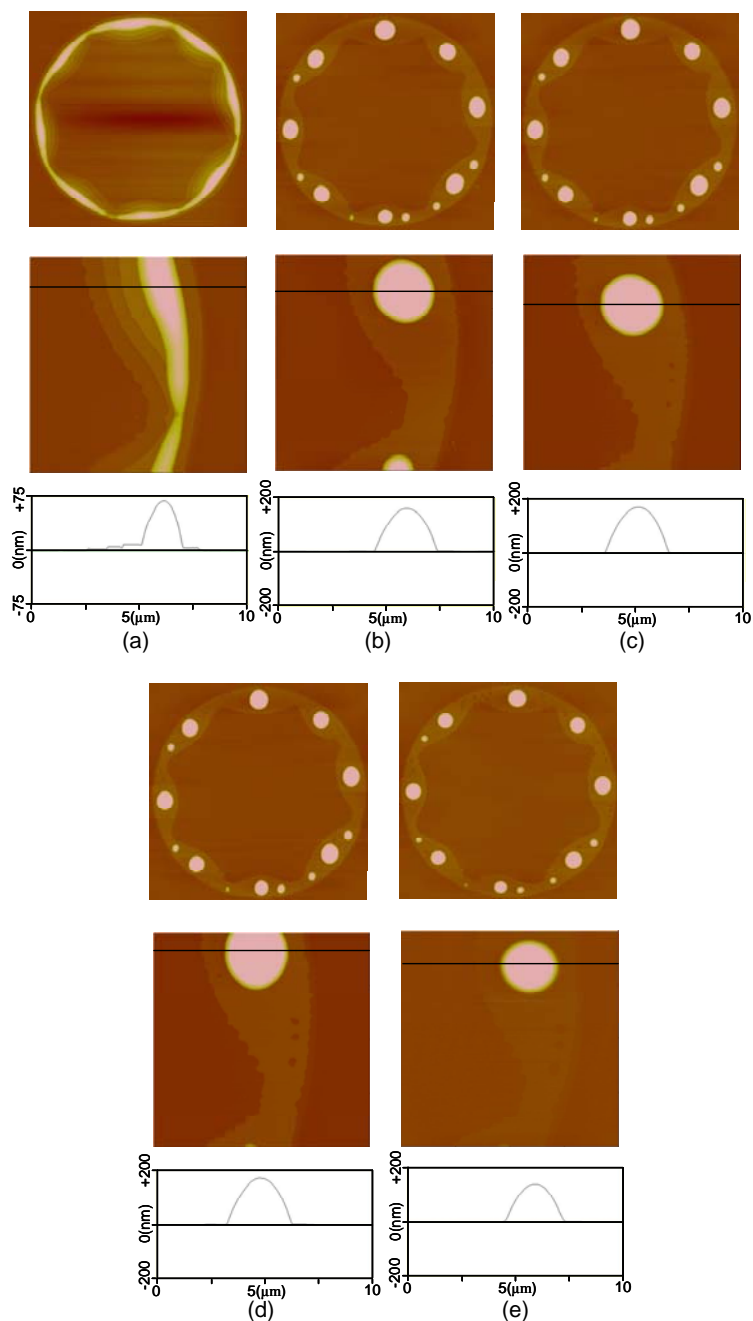


Figure 8.9 Annealing sequence for G2-50% C_{12} ring ($d=33.84 \mu\text{m}$) at $1.0 T_c$ (348K, 75°C).

(a) as deposited (b) 5 minutes at 75°C (c) 30 minutes at 75°C (d) 60 minutes at 75°C (e) 24 hours after annealing at 75°C . Top: topographic images of full rings; middle: topographic images of ring segment at ‘3-o’clock’ position; bottom: radial cross-sectional scans through representative ‘scallop’. The topographic images of the full rings are scaled to yield equal diameters on the print page. The ‘middle’ images are $10 \mu\text{m} \times 10 \mu\text{m}$.

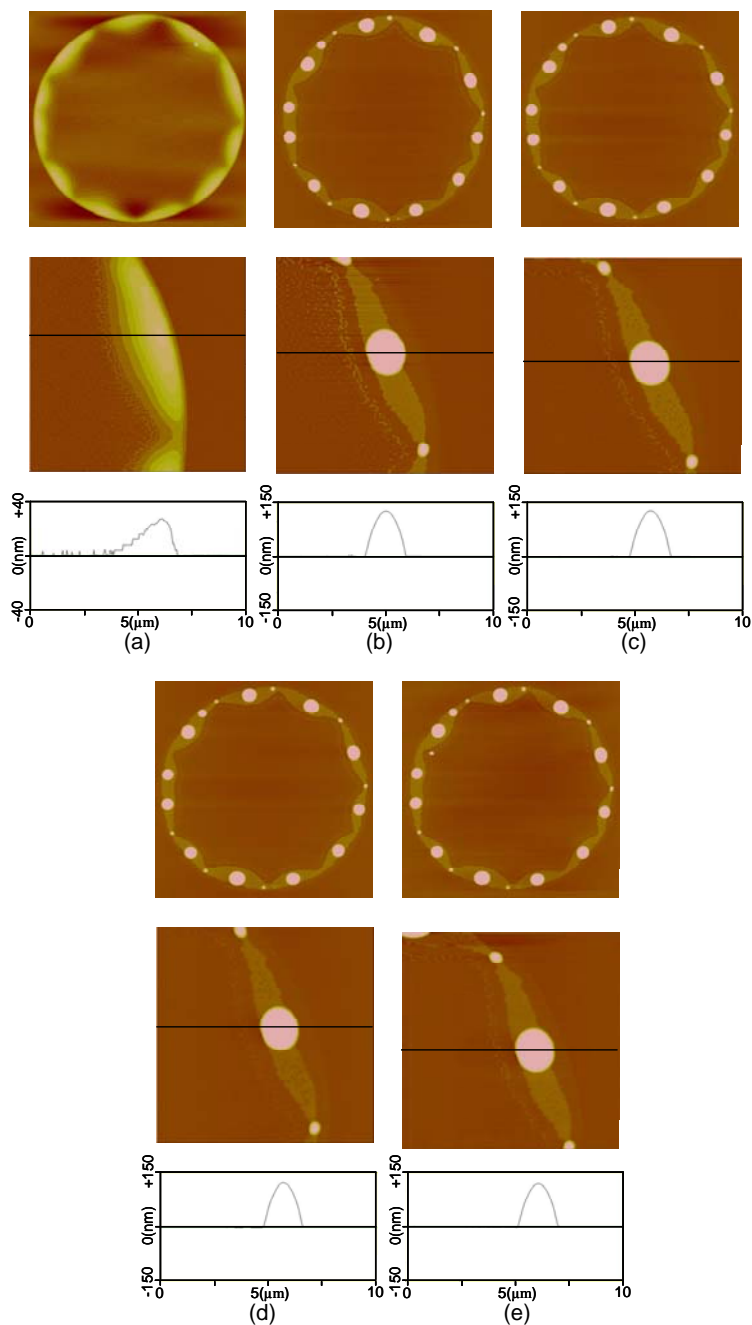


Figure 8.10 Annealing sequence for G2-50% C_{12} ring ($d=27.78 \mu\text{m}$) at $1.05 T_c$ (365K, 92°C).

(a) as deposited (b) 5 minutes at 92°C (c) 30 minutes at 92°C (d) 60 minutes at 92°C (e) 24 hours after annealing at 92°C . Top: topographic images of full rings; middle: topographic images of ring segment at ‘3-o’clock’ position; bottom: radial cross-sectional scans through representative ‘scallop’. The topographic images of the full rings are scaled to yield equal diameters on the print page. The ‘middle’ images are $10 \mu\text{m} \times 10 \mu\text{m}$.

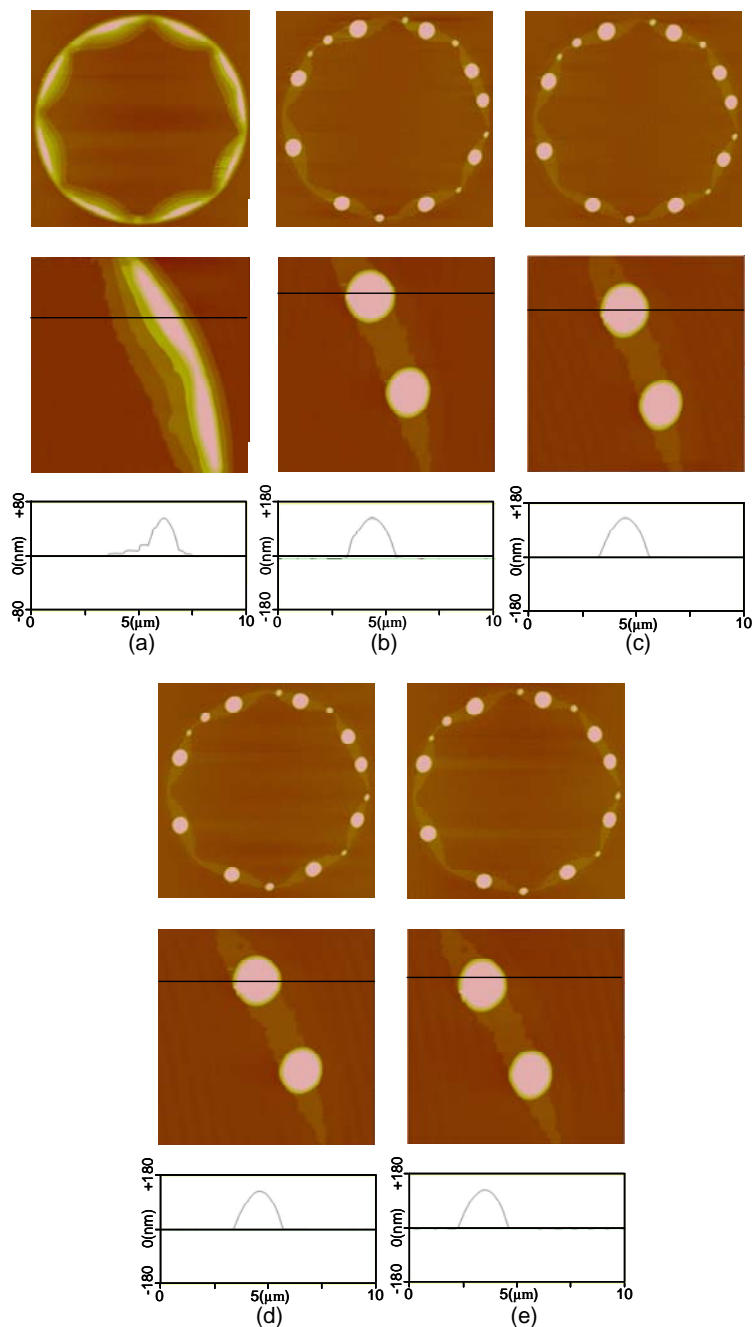


Figure 8.11 Annealing sequence for G2-50% C_{12} ring ($d=30.63 \mu\text{m}$) at $1.1 T_c$ (383K, 110°C).

(a) as deposited (b) 5 minutes at 110°C (c) 30 minutes at 110°C (d) 60 minutes at 110°C (e) 24 hours after annealing at 110°C . Top: topographic images of full rings; middle: topographic images of ring segment at ‘3-o’clock’ position; bottom: radial cross-sectional scans through representative ‘scallop’. The topographic images of the full rings are scaled to yield equal diameters on the print page. The ‘middle’ images are $10 \mu\text{m} \times 10 \mu\text{m}$.

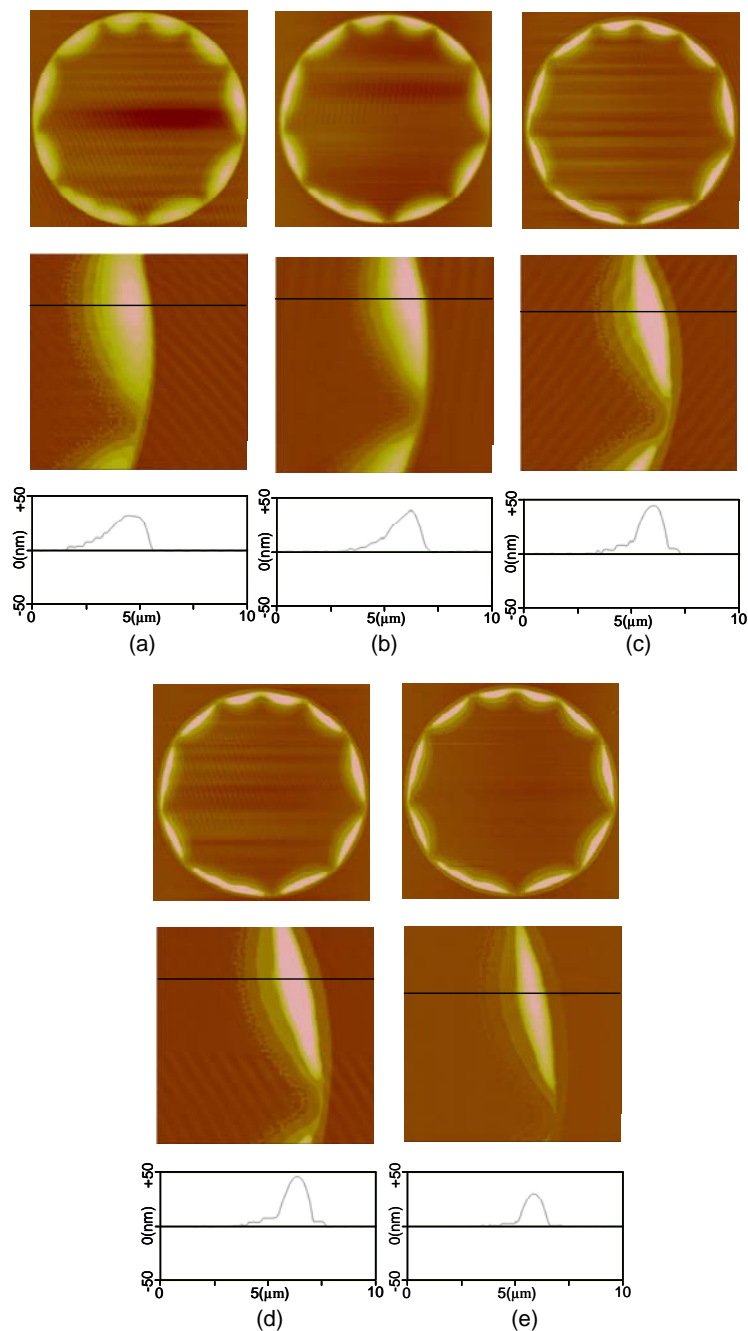


Figure 8.12 Annealing sequence for G3-50% C_{12} ring ($d=29.74 \mu\text{m}$) at $0.9 T_c$ (331K, 58°C).

(a) as deposited (b) 5 minutes at 58°C (c) 30 minutes at 58°C (d) 60 minutes at 58°C (e) 24 hours after annealing at 58°C . Top: topographic images of full rings; middle: topographic images of ring segment at ‘3-o’clock’ position; bottom: radial cross-sectional scans through representative ‘scallop’. The topographic images of the full rings are scaled to yield equal diameters on the print page. The ‘middle’ images are $10 \mu\text{m} \times 10 \mu\text{m}$.

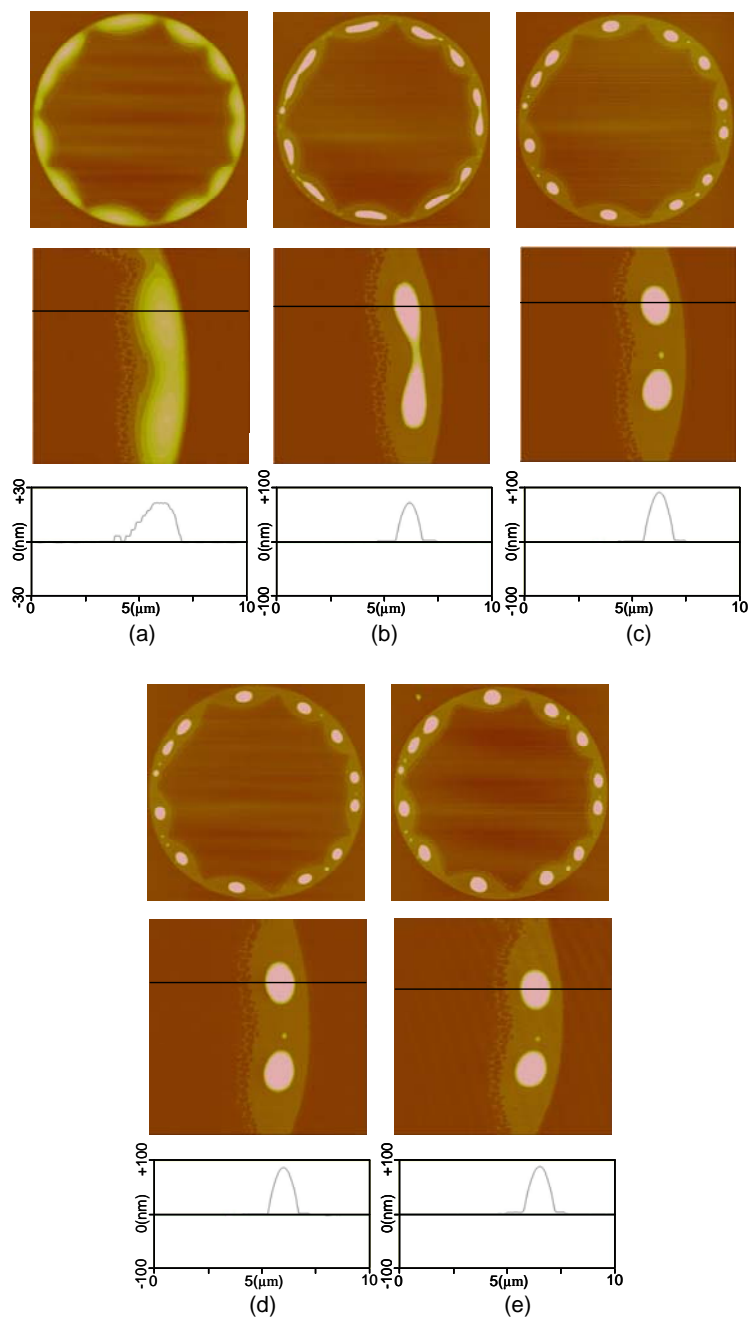


Figure 8.13 Annealing sequence for G3-50% C_{12} ring ($d=29.67 \mu\text{m}$) at $0.95 T_c$ (350K, 77°C).

(a) as deposited (b) 5 minutes at 77°C (c) 30 minutes at 77°C (d) 60 minutes at 77°C (e) 24 hours after annealing at 77°C . Top: topographic images of full rings; middle: topographic images of ring segment at '3-o'clock' position; bottom: radial cross-sectional scans through representative 'scallop'. The topographic images of the full rings are scaled to yield equal diameters on the print page. The 'middle' images are $10 \mu\text{m} \times 10 \mu\text{m}$.

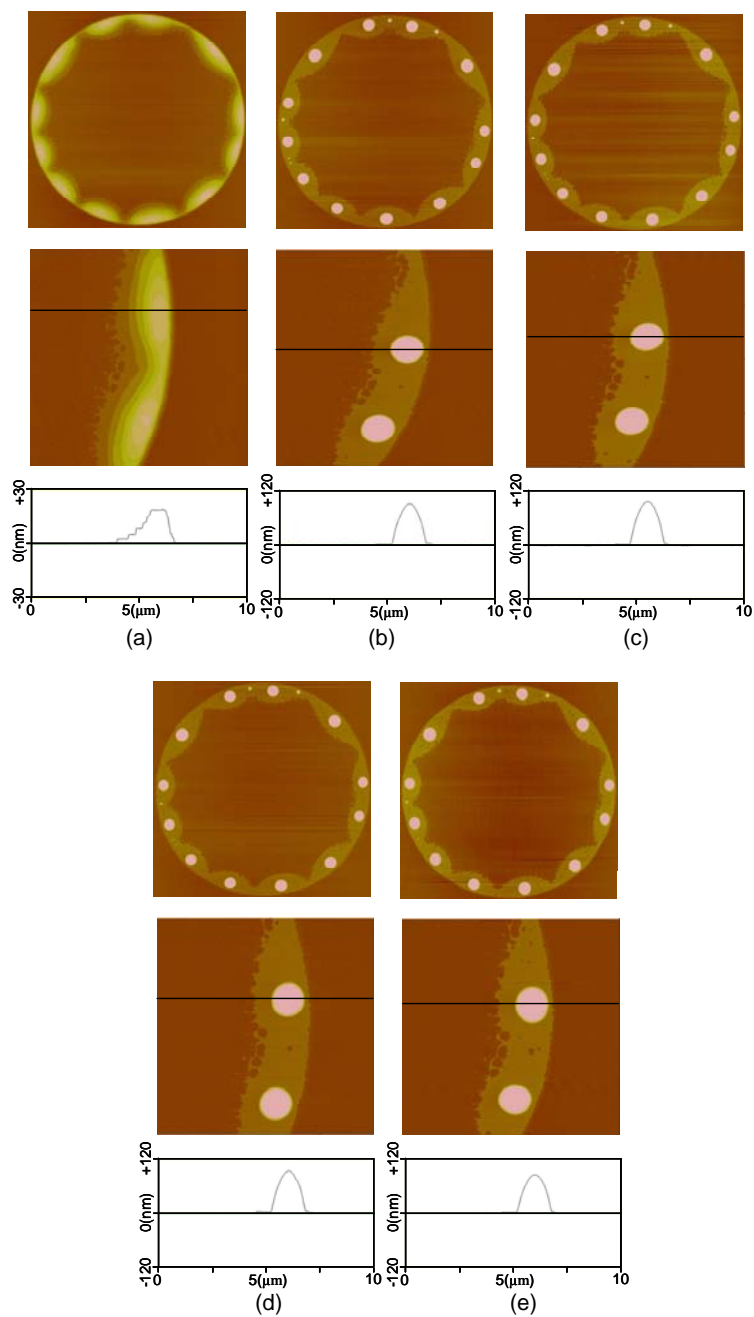


Figure 8.14 Annealing sequence for G3-50% C_{12} ring ($d=29.90 \mu\text{m}$) at $1.0 T_c$ (368K, 95°C).

(a) as deposited (b) 5 minutes at 95°C (c) 30 minutes at 95°C (d) 60 minutes at 95°C (e) 24 hours after annealing at 95°C . Top: topographic images of full rings; middle: topographic images of ring segment at ‘3-o’clock’ position; bottom: radial cross-sectional scans through representative ‘scallop’. The topographic images of the full rings are scaled to yield equal diameters on the print page. The ‘middle’ images are $10 \mu\text{m} \times 10 \mu\text{m}$

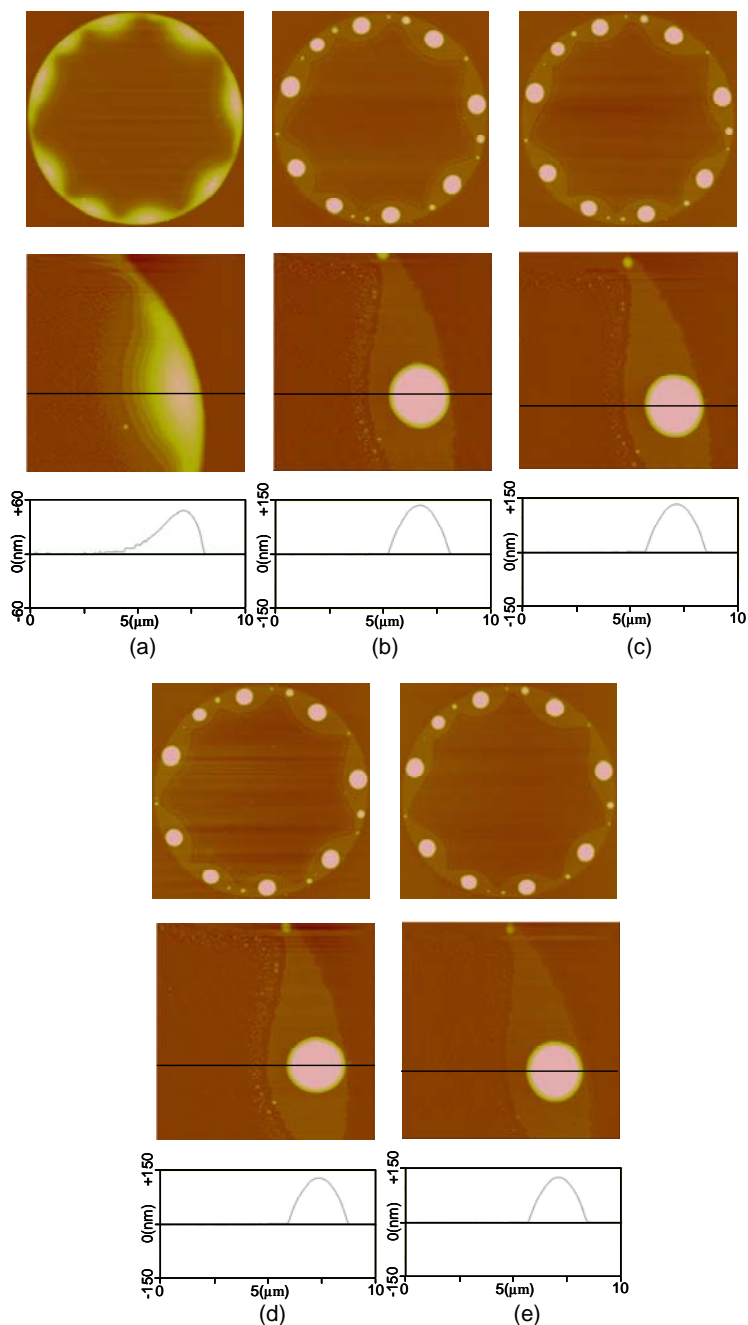


Figure 8.15 Annealing sequence for G3-50% C_{12} ring ($d=29.95 \mu\text{m}$) at $1.05 T_c$ (386K, 113°C).

(a) as deposited (b) 5 minutes at 113°C (c) 30 minutes at 113°C (d) 60 minutes at 113°C (e) 24 hours after annealing at 113°C . Top: topographic images of full rings; middle: topographic images of ring segment at ‘3-o’clock’ position; bottom: radial cross-sectional scans through representative ‘scallop’. The topographic images of the full rings are scaled to yield equal diameters on the print page. The ‘middle’ images are $10 \mu\text{m} \times 10 \mu\text{m}$

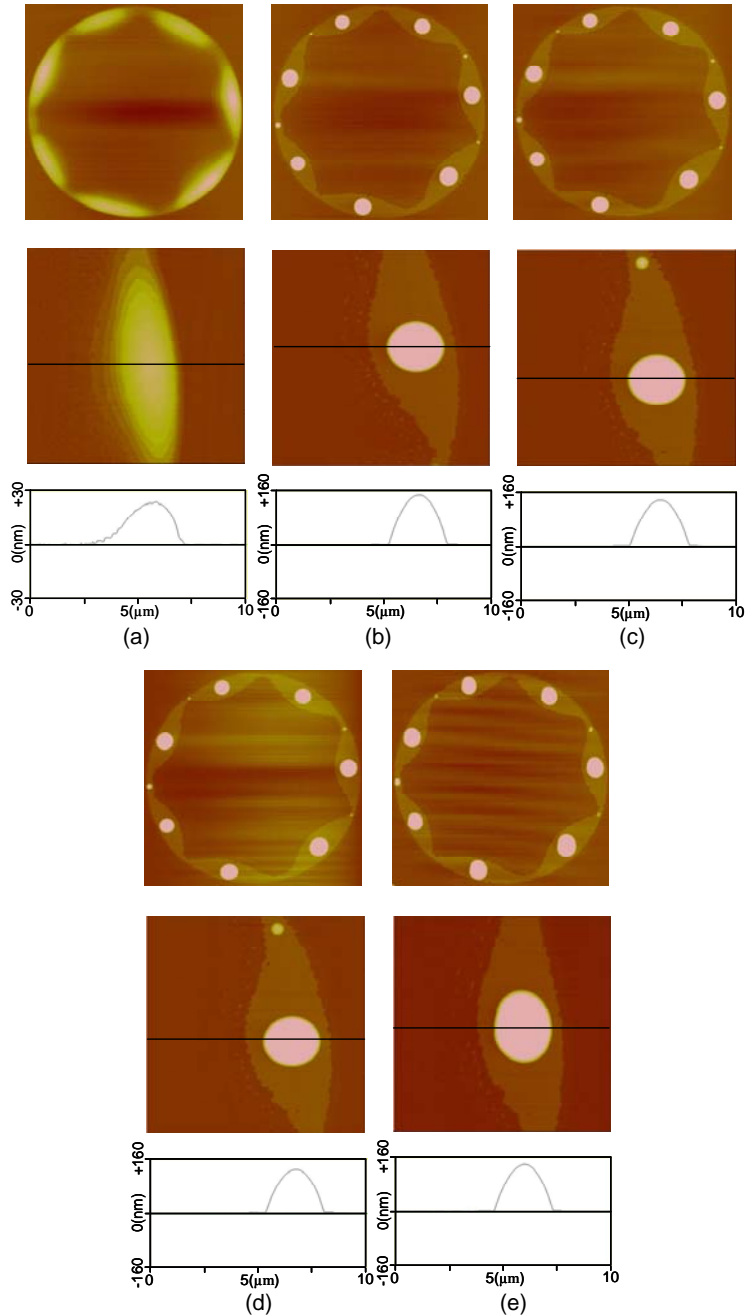


Figure 8.16 Annealing sequence for G3-50% C_{12} ring ($d=31.20 \mu\text{m}$) at $1.1 T_c$ (405K, 132°C).

(a) as deposited (b) 5 minutes at 132°C (c) 30 minutes at 132°C (d) 60 minutes at 132°C (e) 24 hours after annealing at 132°C . Top: topographic images of full rings; middle: topographic images of ring segment at ‘3-o’clock’ position; bottom: radial cross-sectional scans through representative ‘scallop’. The topographic images of the full rings are scaled to yield equal diameters on the print page. The ‘middle’ images are $10 \mu\text{m} \times 10 \mu\text{m}$.

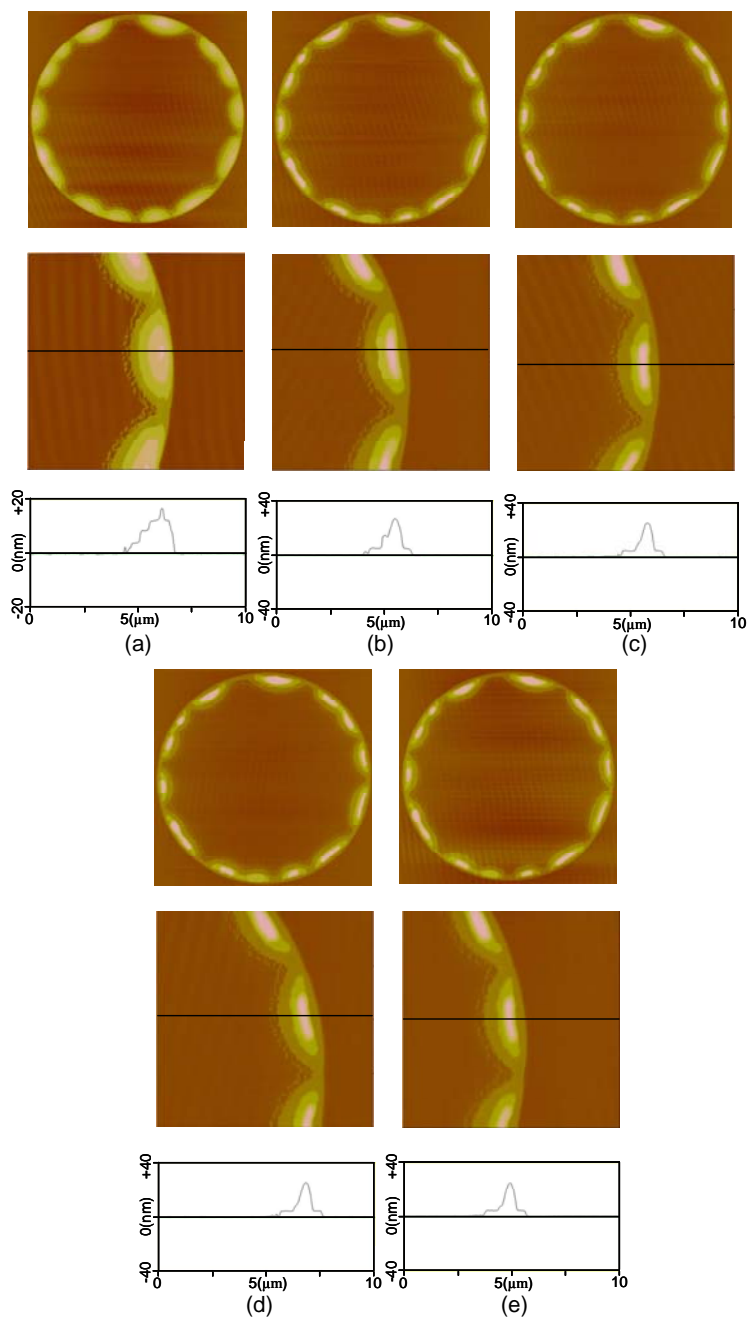


Figure 8.17 Annealing sequence for G4-50% C_{12} ring ($d=24.38 \mu\text{m}$) at $0.9 T_c$ (363K, 90°C).

(a) as deposited (b) 5 minutes at 90°C (c) 30 minutes at 90°C (d) 60 minutes at 90°C (e) 24 hours after annealing at 90°C . Top: topographic images of full rings; middle: topographic images of ring segment at ‘3-o’clock’ position; bottom: radial cross-sectional scans through representative ‘scallop’. The topographic images of the full rings are scaled to yield equal diameters on the print page. The ‘middle’ images are $10 \mu\text{m} \times 10 \mu\text{m}$

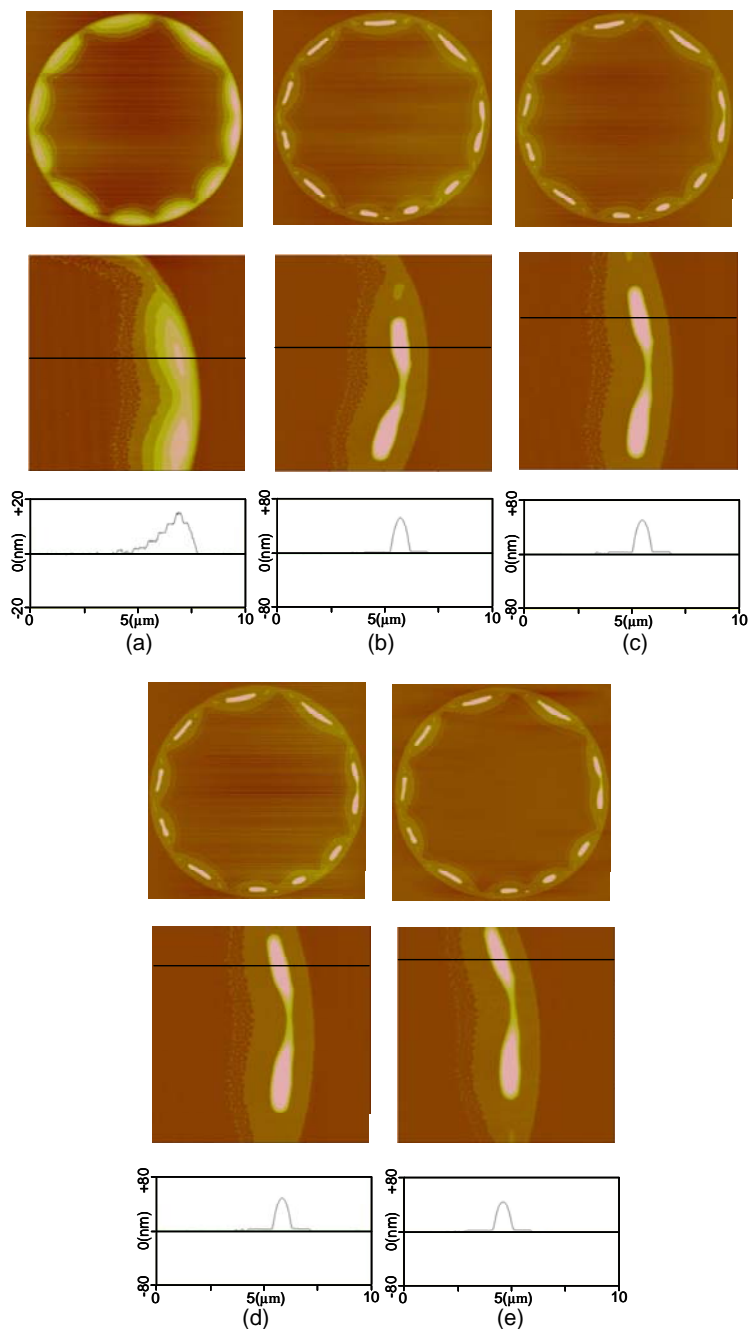


Figure 8.18 Annealing sequence for G4-50% C_{12} ring ($d=31.38 \mu\text{m}$) at $0.95 T_c$ (383K, 110°C).

(a) as deposited (b) 5 minutes at 110°C (c) 30 minutes at 110°C (d) 60 minutes at 110°C (e) 24 hours after annealing at 110°C . Top: topographic images of full rings; middle: topographic images of ring segment at ‘3-o’clock’ position; bottom: radial cross-sectional scans through representative ‘scallop’. The topographic images of the full rings are scaled to yield equal diameters on the print page. The ‘middle’ images are $10 \mu\text{m} \times 10 \mu\text{m}$

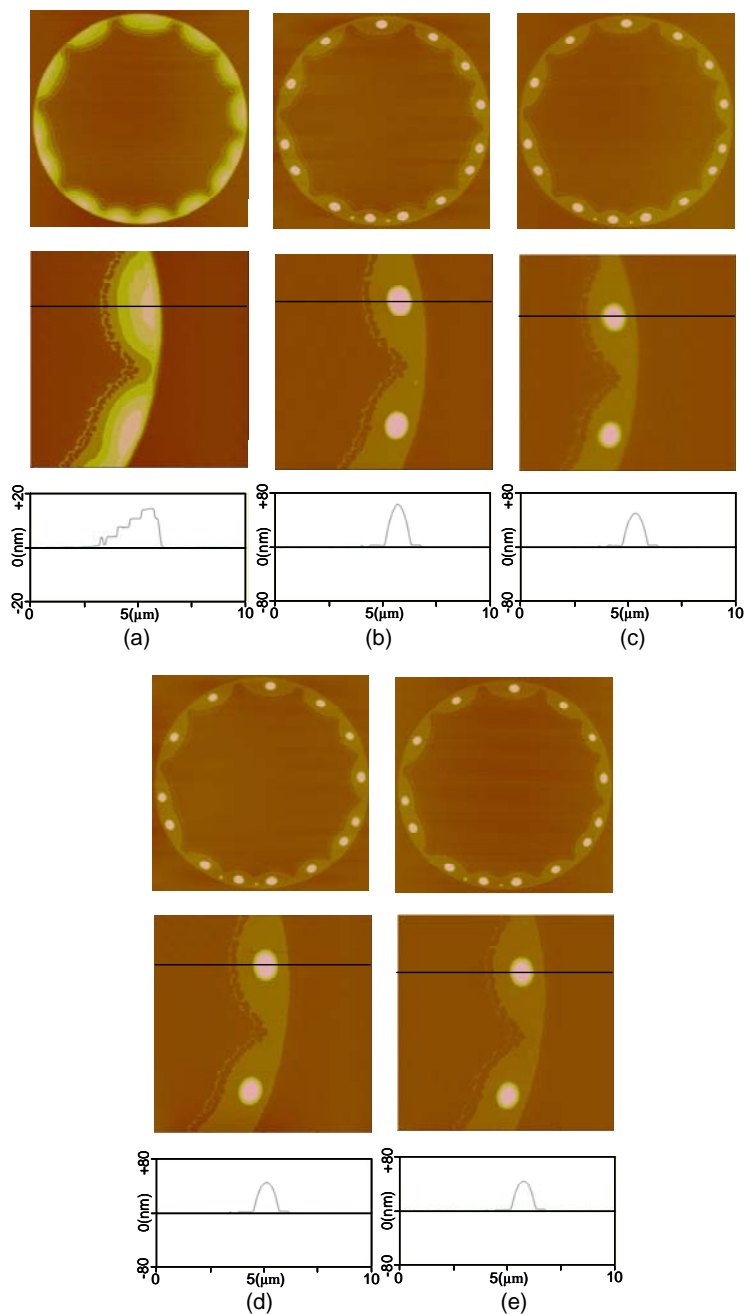


Figure 8.19 Annealing sequence for G4-50% C_{12} ring ($d=27.14 \mu\text{m}$) at $1.0 T_c$ (403K, 130°C).

(a) as deposited (b) 5 minutes at 130°C (c) 30 minutes at 130°C (d) 60 minutes at 130°C (e) 24 hours after annealing at 130°C . Top: topographic images of full rings; middle: topographic images of ring segment at ‘3-o’clock’ position; bottom: radial cross-sectional scans through representative ‘scallop’. The topographic images of the full rings are scaled to yield equal diameters on the print page. The ‘middle’ images are $10 \mu\text{m} \times 10 \mu\text{m}$

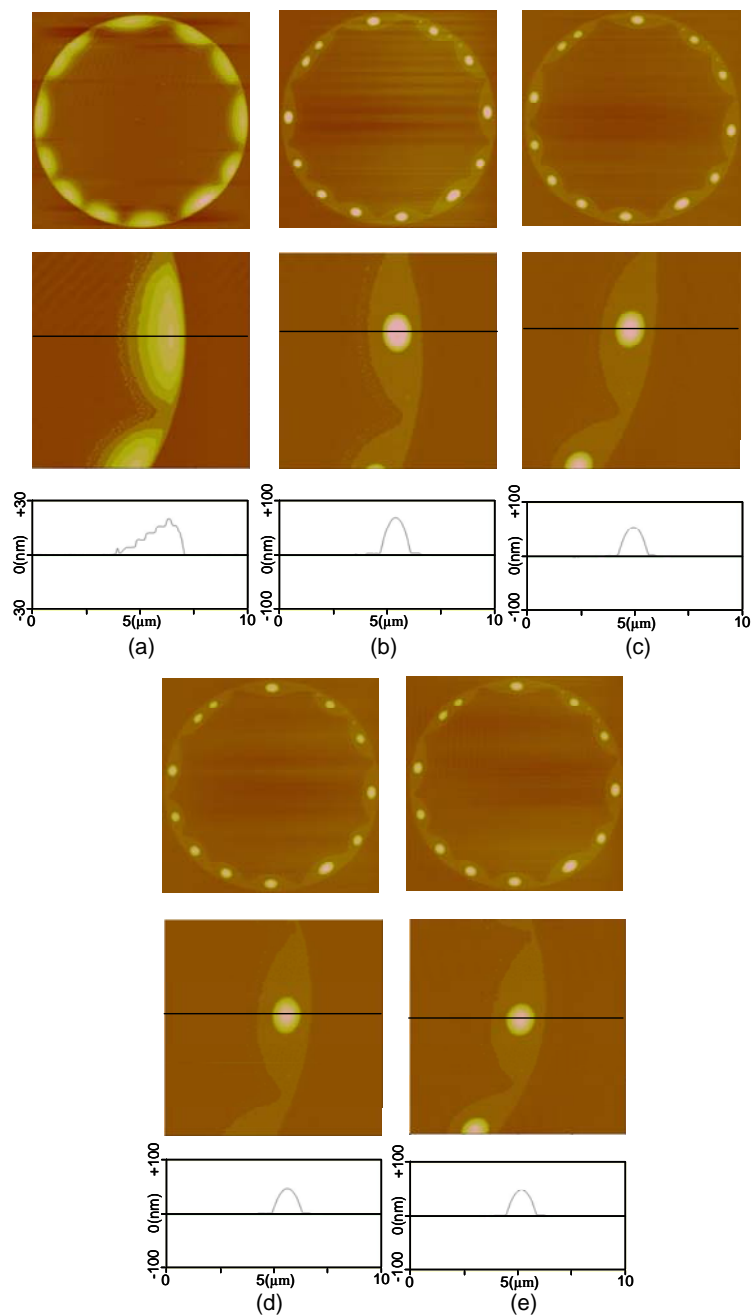


Figure 8.20 Annealing sequence for G4-50% C_{12} ring ($d=27.72 \mu\text{m}$) at $1.05 T_c$ (423K, 150°C).

(a) as deposited (b) 5 minutes at 150°C (c) 30 minutes at 150°C (d) 60 minutes at 150°C (e) 24 hours after annealing at 150°C . Top: topographic images of full rings; middle: topographic images of ring segment at ‘3-o’clock’ position; bottom: radial cross-sectional scans through representative ‘scallop’. The topographic images of the full rings are scaled to yield equal diameters on the print page. The ‘middle’ images are $10 \mu\text{m} \times 10 \mu\text{m}$

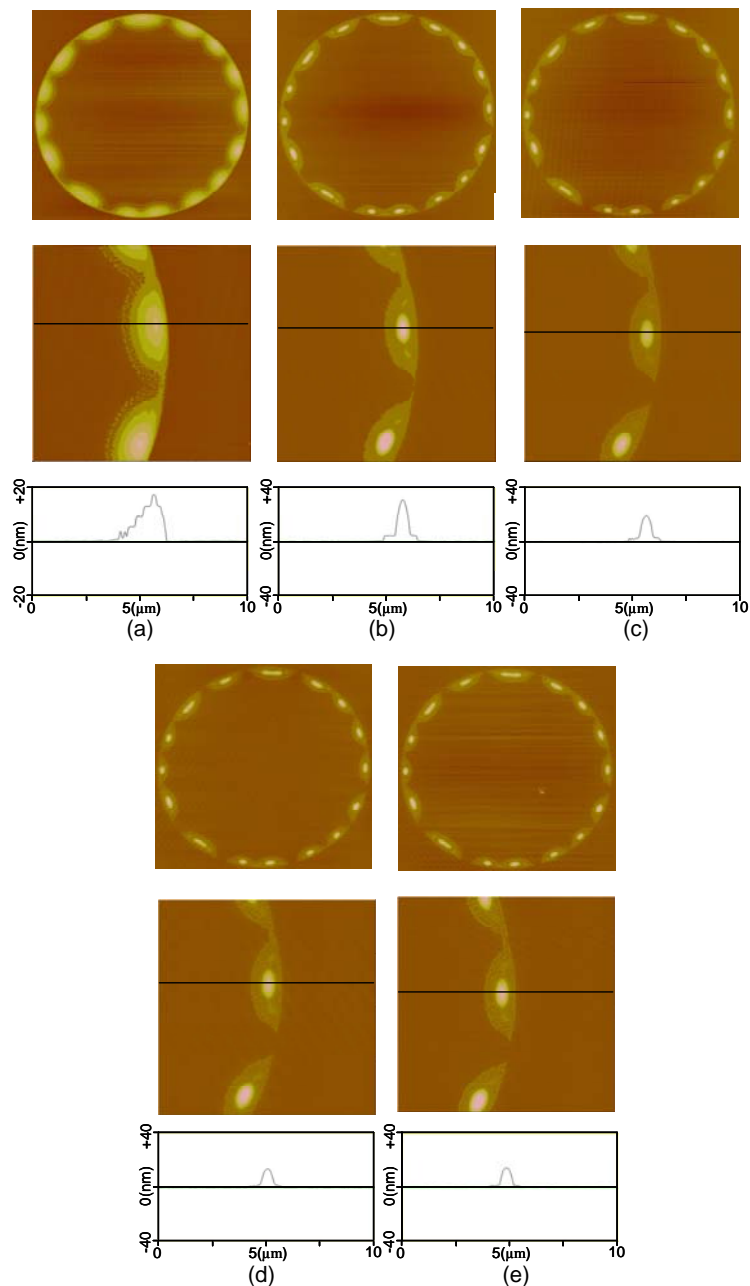


Figure 8.21 Annealing sequence for G4-50% C_{12} ring ($d=30.42 \mu\text{m}$) at $1.1 T_c$ (443K, 170°C).

(a) as deposited (b) 5 minutes at 170°C (c) 30 minutes at 170°C (d) 60 minutes at 170°C (e) 24 hours after annealing at 170°C . Top: topographic images of full rings; middle: topographic images of ring segment at ‘3-o’clock’ position; bottom: radial cross-sectional scans through representative ‘scallop’. The topographic images of the full rings are scaled to yield equal diameters on the print page. The ‘middle’ images are $10 \mu\text{m} \times 10 \mu\text{m}$

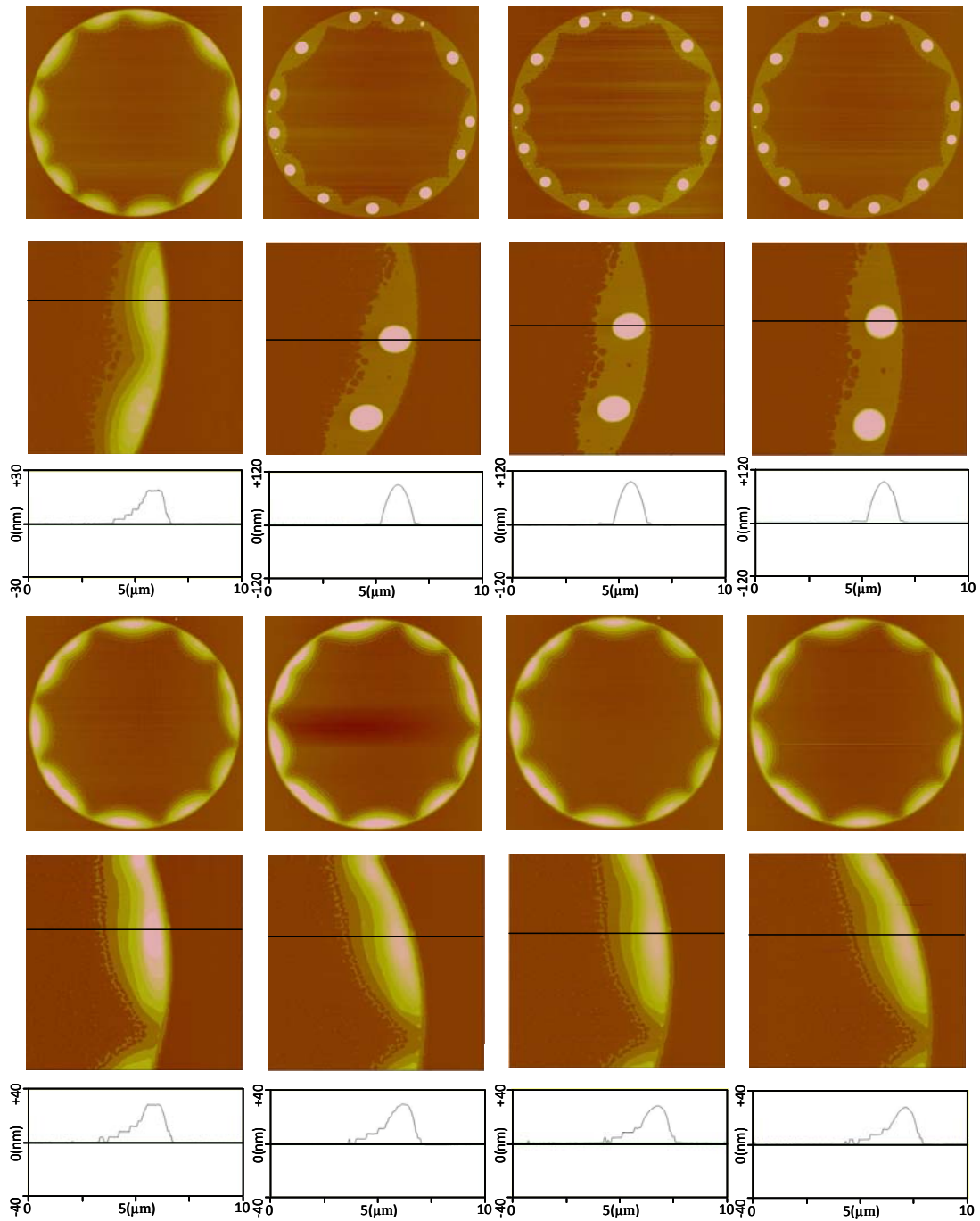


Figure 8.22 Annealing sequences at 95°C ($1.0 T_c$) for two G3-50% C_{12} rings.

Illustration of the stabilizing effect of holding the sample at room temperature before annealing. Top half : annealing sequence for freshly evaporated ring ($d=29.9 \mu\text{m}$); bottom half : annealing sequence for ring held for 24 hours at room temperature before annealing ($28.7 \mu\text{m}$). Images from the left are: as-deposited (top) and as-deposited plus 24 hours (bottom), 5 min at 95°C, 30 min at 95°C, 60 min at 95°C. The topographic images are $10 \mu\text{m} \times 10 \mu\text{m}$.

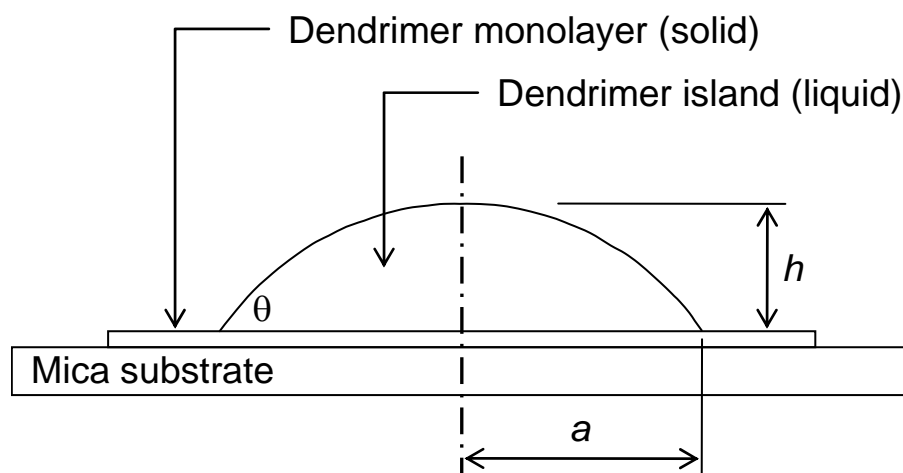


Figure 8.23 Equilibrium between dendrimer island and dendrimer monolayer.

The spherical cap geometry of a dendrimer island in equilibrium with a monolayer of dendrimer solid on a mica substrate.

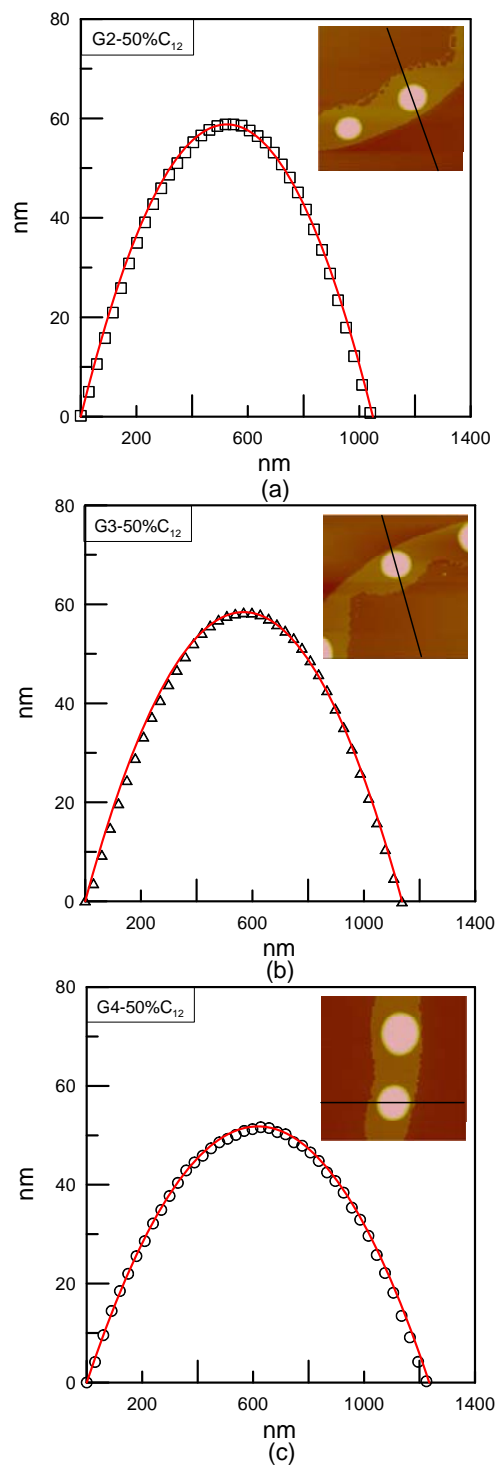


Figure 8.24 Comparison of ideal spherical cap profile and AFM profile.

The ideal spherical cap profiles (solid lines) and measured AFM profiles (open symbols) for three dendrimer islands of different generation; (a) G2-50% C_{12} , (b) G3-50% C_{12} , (c) G4-50% C_{12} . The inserts indicate the section lines used for the AFM measurements.

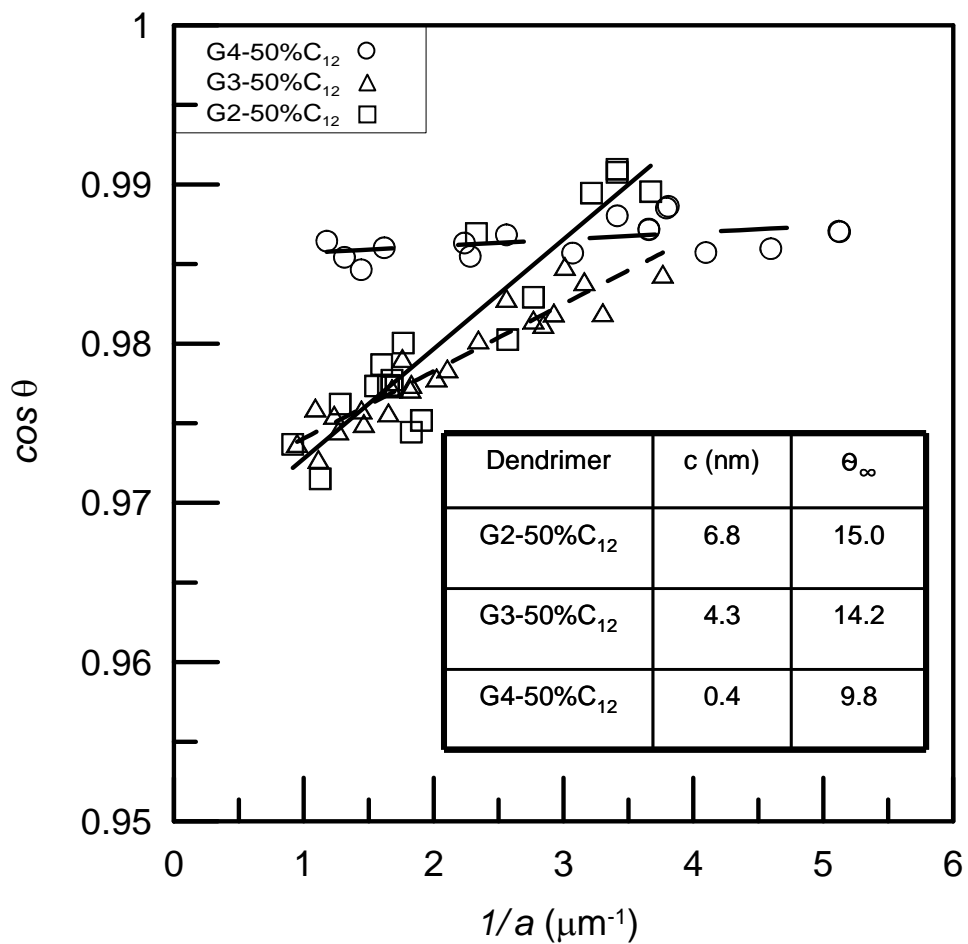


Figure 8.25 Plot of $\text{Cos } \theta$ and local curvature.

$\text{Cos } \theta$ versus $1/a$ for G2-50%C₁₂, G3-50%C₁₂, and G4-50%C₁₂ dendrimer islands. The table (insert) contains the calculated characteristic length scale, c , and macroscopic contact angle, θ_∞ .

9.0 CONCLUSIONS AND RECOMMENDATIONS FOR FUTURE WORK

9.1 SURFACE CHEMISTRY EFFECTS

The condensed structures resulting from micro-droplet evaporation sensitively depend on, and are characteristic of, the surface chemistry of the dendrimer solute molecules. This conclusion has been experimentally confirmed by comparing the behavior of G4, G4-25% C_{12} , and G4-50% C_{12} dendrimers using mica substrates. For the dilute concentration studied here (0.05wt%) the presence of periodically ‘scalped’ molecular rings is ubiquitous. The interiors of the condensed rings are essentially free of adsorbed dendrimers (they have been swept to the perimeter during evaporation and incorporated in the growing ring). The perimeter is held in place by contact line pinning which is strengthened by the accumulating molecules. The instability wavelength of the scalped rings is proportional to the width of the ring with a proportionality constant similar to that expected in the rim instability observed in dewetting holes. The effect of the surface chemistry of the dendrimer molecules is revealed in the detailed structure of the self assembled rings. G4 rings are comparatively diffuse and disordered with no evidence for layered growth. Changing the chemistry of 25% of the G4 terminal sites (G4-25% C_{12}) leads to more highly ordered ring structures and the onset of monomolecular terracing. Further modification of the terminal shell chemistry (G4-50% C_{12}) leads to highly periodic scallops and very distinct monomolecular height terraced growth of the rings with flat terraces

and sharply defined steps. A secondary growth instability along the terrace edges is observed in the G4-50%C₁₂ samples. Pattern formation in the evaporating droplet following initial pinning depends sensitively on the chemistry of the dendrimer terminal shell which modulates dendrimer-dendrimer and dendrimer-substrate interactions.

9.2 EVAPORATION RATE AND THE DENDRIMER GENERATION EFFECTS

The detailed morphologies of condensed dendrimer ring structures resulting from micro-droplet evaporation also depend sensitively on both the solute evaporation rate and the dendrimer generation. This conclusion has been experimentally confirmed by comparing the behavior of G2-50%C₁₂, G3-50%C₁₂, and G4-50%C₁₂ dendrimers in two solvent alcohols (pentanol and hexanol) on mica substrates. In the dilute regime (0.1 wt %) the growth of highly stratified (monomolecular height terraces) and periodically ‘scalped’ dendrimer rings is ubiquitous. The interiors of the condensed rings are mostly free of adsorbed dendrimers, however, pentanol-based rings have cleaner mica interiors than the hexanol-based rings (corresponding to more complete incorporation of dendrimer molecules in the growing ring). The instability wavelength of the scalped rings is proportional to the width of the ring. The proportionality constant depends strongly on solvent, 4.8 for pentanol and 2.3 for hexanol. Pentanol evaporates at a rate three times that of hexanol, and thus the flux of molecules to the growing ring is expected to be significantly higher in pentanol than hexanol. A short wavelength undulation is also noted in all of the dilute ring structures at the front edge of the lower terraces. The wavelength of this secondary instability again depends on solvent (in this case, shorter in pentanol than hexanol). The influence of dendrimer generation on ring structure primarily reflects the increase in

dendrimer density with generation number. Overall pattern formation in the evaporating droplet thus depends on ring growth rate and dendrimer size, and the chemistry of the dendrimer terminal shell. The morphological evolution of G2-50% C_{12} - pentanol rings as a function of dendrimer concentration has also been described.

9.3 THERMAL EFFECTS

Stratified dendrimer rings undergo dramatic temperature and time dependent (and dendrimer generation dependent) morphological changes associated with large-scale molecular rearrangements and partial melting. These thermally driven transformations produce ring structures consisting of a highly stable first monolayer of the scalloped structure in equilibrium with spherical cap shaped dendrimer islands that form at the center of each pre-existing scallop (a kind of ‘pearl necklace’ structure). As-evaporated structures can be stabilized against thermally driven rearrangements by holding the structures at room temperature before annealing instead of annealing freshly evaporated samples. Analysis of the dendrimer island shapes reveals a dependence of island contact angle on contact line curvature (island size) that varies systematically with dendrimer generation. These morphological transformations point to the potential for creating complex multilevel structures and arrays of macroscopic scale using, for example, droplet-on-demand or dip pen nanolithography techniques, coupled with appropriate annealing and stabilizing treatments. The positive slope of $\cos \theta$ versus $1/a$ implies the negative sign of contact line tension in the system. The slope and θ_∞ decrease as the molecule size and number of terminal sites increases.

9.4 FUTURE WORK

The opportunities for extending this work to explore the effects of other system variables are exciting. By combining careful experimental design (e.g., varying the dendrimer type, dendrimer termination, structure geometry, substrate, etc.) with physically realistic simulations these systems can provide an ideal experimental basis for quantitative determination of a number of largely unavailable, yet critical, physical parameters such as surface and adhesion energies, line tensions, molecular diffusivities, and transition temperatures. The possibilities for pre-patterning the substrate either physically or chemically are also unexplored but are clearly promising. The combination of substrate surface functionalization and/or physical patterning, drop delivery systems which allow precise size and position control and thus creation of micro-droplet arrays, and rapid and efficient ‘interrogation’ of the evaporated drop patterns (using automated high speed SPM or optical/electron microscopy) could lead to high throughput lab-on-a-chip style bio-chemical screening. The morphology of molecular ring patterns formed by controlled evaporation of micro-droplets could be used as a ‘fingerprint’ to identify, for example, solute molecule surface chemistry and concentration and serve as an indicator of targeted binding or functionalization events.

BIBLIOGRAPHY

- [1] Deegan, R.D., Bakajin, O., Dupont, T.F., Huber, G., Nagel, S.R., & Witten, T.A. "Capillary flow as the cause of ring stains from dried liquid drops", *Nature* 389, 827-829 (1997).
- [2] Nadkarni, G. & Garoff, S. "An investigation of microscopic aspects of contact angle hysteresis: pinning of the contact line on a single defect", *Europhys. Lett.* 20, 523-528 (1992).
- [3] Decker, E. & Garoff, S., "Contact line structure and dynamics on surfaces with contact angle hysteresis" *Langmuir* 13, 6321-6332 (1997).
- [4] Deegan, R.D. "Pattern formation in drying drops", *Phys. Rev. E* 61, 475-485 (2000).
- [5] Sommer, A. P.; Rozlosnik, "Formation of Crystalline Ring Patterns on Extremely Hydrophobic Supersmooth Substrates: Extension of Ring Formation Paradigms" *N. Cryst. Growth Des.* 5, 551-557 (2005)
- [6] Socol, Y.; Guzman, I.S., "Fast Ring-Shape Self-Assembling in Water-Based Ink-Jetted Droplets" *J. Phys. Chem. B* 110, 18347-18350 (2006)
- [7] de Gans, B-J, Duineveld, P.C., and Schubert, U.S. "Inkjet printing of polymers: state of the art and future developments", *Adv. Mater.* 16, 203-213 (2004).
- [8] de Gans, B-J., and Schubert, U.S. "Inkjet printing of well-defined polymer dots and arrays" *Langmuir* 20, 7789-7793 (2004).
- [9] Magdassi, S.; Ben-Moshe, M., "Patterning of Organic Nanoparticles by Ink-jet Printing of Microemulsions" *Langmuir* 19, 939-942 (2003)
- [10] Sommer, A.P; Franke, R-P. " Biomimicry Patterning with Nanosphere Suspensions" *Nano Letters* 3, 573-575 (2003)
- [11] Sommer, A.P., " Suffocation of Nerve Fibers by Living Nanovesicles: A Model Simulation-Part II" *J. Proteome Res.*, 3, 1086-1088 (2004)
- [12] Sommer, A.P., Gheorghiu, E., Cehreli, M., Mester, A.R., & Whelan, H.T. "Biosensor for detection of nanobacteria in water", *Cryst. Growth Des.* 6, 492-496 (2006)

- [13] Dujardin, E. & Mann, S. "Bio-inspired Materials Chemistry", *Adv. Mater.* 14, 775-788 (2002)
- [14] Dugas, V., Broutin, J. & Souteyrand, E. "Droplet evaporation study applied to DNA chip manufacturing", *Langmuir* 21, 9130-9136 (2005).
- [15] Tomalia, D.A., Naylor, A.M., & Goddard III, W.A, "Starburst dendrimers: molecular level control of size, shape, surface chemistry, topology, and flexibility from atoms to macroscopic matter", *Angew. Chem.* 29, 138-175 (1990).
- [16] Tomalia, D.A. "Starburst/cascade dendrimers: fundamental building blocks for a new nanoscopic chemistry set", *Adv. Mater.* 6, 529-539 (1994)
- [17] Grayson, S.M., Frechet, J. M. J. "Convergent dendrons and dendrimers: from synthesis to applications", *Chem. Rev.* 101, 3819-3868 (2001).
- [18] Newkome, G.R., He, E., & Moorefield, C.N. "Suprasuper molecules with novel properties: metallodendrimers", *Chem. Rev.* 99, 1689-1746 (1999).
- [19] Tomalia, D.A. "Birth of a new macromolecular architecture: dendrimers as quantized building blocks for nanoscale synthetic polymer chemistry", *Prog. Polym. Sci.* 30, 294-324 (2005)
- [20] Buhleier, E., Wehner, W., Vogtle, F., "'Cascade-'and 'Nonskid-Chain-like' syntheses of molecular cavity topologies", *Synthesis* 155-158 (1978)
- [21] Fisher, M., Vogtle, F., "Dendrimers: From Design to Application - A Progress Report", *Angew. Chem. Int. Ed.* 38, 884 (1999)
- [22] Tomalia, D. A., Baker, H., Dewald, J., Hall, M., Kallos, G., Martin, S., Roeck, J., Smith, P. "A New Class of Polymers: Starburst-Dendritic Macromolecules", *Polymer J.* 17, 117-132 (1985)
- [23] Naylor, A. M., Goddard, W. A. "Starburst dendrimers. 4. Covalently fixed unimolecular assemblages reminiscent of spheroidal micelles", *Macromolecules* 20, 1164-1167 (1987)
- [24] Caminati, G., Turro, N. J., Tomalia, D. A., "Photophysical investigation of starburst dendrimers and their interactions with anionic and cationic surfactants", *J. Am. Chem. Soc.* 112, 8515-8522 (1990)
- [25] Gopidas, K. R., Leheny, A. R., Caminati, G., Turro, N. J., Tomalia, D. A. "Photophysical investigation of similarities between starburst dendrimers and anionic micelles", *J. Am. Chem. Soc.* 113, 7335-7342 (1991)
- [26] Lee, I., Athey, B. T., Wetzal, A. W., Meixner, W., Baker, J. R. "Structural Molecular Dynamics Studies on Polyamidoamine Dendrimers for a Therapeutic Application: Effects of pH and Generation", *Macromolecules* 35, 4510-4520 (2002)

- [27] Boas U., Heegaard, P. M. H., “Dendrimers in drug research”, *Chem. Soc. Rev.* 33, 43-63 (2004)
- [28] Quintana, A. E., Raczka, E., Piehler, L., Lee, I., Myc, A., Majoros, I., Patri, A. K., Thomas, T., Mule, J., Baker, J. R., “Design and Function of a Dendrimer-Based Therapeutic Nanodevice Targeted to Tumor Cells Through the Folate Receptor”, *Pharm. Res.* 19, 1310-1316 (2002)
- [29] Choi, Y., Baker, J. R., “Targeting cancer cells with DNA-assembled dendrimers: a mix and match strategy for cancer”, *Cell Cycle* 4, 669–671 (2005)
- [30] Baker, L.A., Zamborini, F.P., Sun, L., & Crooks, R.M. “Dendrimer-Mediated Adhesion between Vapor-Deposited Au and Glass or Si Wafers”, *Anal. Chem.* 71, 4403-4406 (1999)
- [31] Rahman, K.M.A., Durning, C.J., Turro, N.J., & Tomalia, D.A. “Adsorption of poly(amidoamine) dendrimers on gold”, *Langmuir* 16, 10154-10160 (2000)
- [32] Tokuhisa, H., Zhao, M., Baker, L.A., Phan, V.T., Dermody, D.L., Garcia, M.E., Peez, R.F., Crooks, R.M., & Mayer, T.T. “Preparation and characterization of dendrimer monolayers and dendrimer-alkanethiol mixed monolayers adsorbed to gold”, *J. Am. Chem. Soc.* 120, 4492-4501 (1998)
- [33] Tsukruk, V. V., Rinderspracher, F., Bliznyuk, V. N., “Self-Assembled Multilayer Films from Dendrimers”, *Langmuir* 13, 2171-2176 (1997)
- [34] Zhao, M., Liu, R. M., Crooks, Bergbreiter, D. E., “Preparation of Highly Impermeable Hyperbranched Polymer Thin-Film Coatings Using Dendrimers First as Building Blocks and Then as in Situ Thermosetting Agents”, *J. Am. Chem. Soc.* 121, 923 (1999)
- [35] Liu, Y., Brueneing, M. L., Bergbreiter, D. E., Crooks, R. M., “Multilayer Dendrimer-Polyanhydride Composite Films on Glass, Silicon, and Gold Wafers”, *Angew. Chem. Int. ed.* 36, 2114-2117 (1997)
- [36] Street, S. C., Rar, A., Zhou, J. N., Liu, W. J., Barnard, J. A., “Unique Structural and Mechanical Properties of Ultrathin Au Films Grown on Dendrimer-Mediated Substrates”, *Chem. Mater.* 13, 3669-3677 (2001)
- [37] Rar, A., Zhou, N. J., Liu, W. J., Barnard, J. A., Bennett, A., Street, S. C., “Dendrimer-mediated growth of very flat ultrathin Au films”, *Appl. Surf. Sci.* 175-176, 134-139 (2001)
- [38] Rar, A., Curry, M., Barnard, J. A., Street, S. C., “Thin metal films deposited on dendrimer monolayers”, *Trib. Lett.* 12, 87-94 (2002)
- [39] Curry, M., Arrington, D., Street, S. C., Xu, F. T., Barnard, J. A., “Kinetic energy influences on the growth mode of metal overlayers on dendrimer mediated substrates” *J. Vac. Sci. Technol. A* 21, 234-240 (2003)

- [40] Young, T., “An Essay on the Cohesion of Fluids”, *Philos. Trans. R. Soc. London* 95, 65-87 (1805)
- [41] Parisse, F., Allain, C., “Shape changes of colloidal suspension droplets during drying”, *J. Phys. II* 6, 1111-1119 (1996)
- [42] El Bediwi, A. B., Kulnis, W. J., Luo, Y., Woodland, D., Unertl, W. N., “Distributions of latex particles deposited for water suspensions”, *Mater. Res. Soc. Proc.* 372, 277-282 (1995)
- [43] Denkov, N. D., Velev, O., Kralchevski, P., Ivanov, I., Yoshimura, H., Nagayama, K., “Mechanism of formation of two-dimensional crystals from latex particles on substrates”, *Langmuir* 8, 3183-3190 (1992)
- [44] Deegan, R. D.; Bakajin, O.; Dupont, T. F.; Huber, G.; Nagal, S. R.; Witten, T. A., “Contact line deposits in an evaporating drop”, *Phys. Rev. E* 62, 756-765 (2000)
- [45] Li, Q.; Zhu, Y.T.; Kinloch, I.A.; Windle, A.H. “Self-Organization of Carbon Nanotubes in Evaporating Droplets” *J. Phys. Chem. B* 110, 13926-13930 (2006)
- [46] Small, W.R.; Walton, C.D.; Loos, J.; Marc in het huis “Carbon Nanotube Network Formation from Evaporating Sessile Drops” *J. Phys. Chem. B* 110, 13029-13036 (2006)
- [47] Andreeva, L.V.; Koshkin, A.V.; Lebedev-Stepanov, P.V.; Petrov, A.N., Alfimov, M.V.; “Driving forces of the solute self-organization in an evaporating liquid microdroplet” *Colloid Surfaces A* 300, 300-306 (2007)
- [48] Maeda, H.; “An Atomic Force Microscopy Study of Ordered Molecular Assemblies and Concentric Ring Patterns from Evaporating Droplets of Collagen Solutions” *Langmuir* 15, 8505-8513 (1999)
- [49] Okuba, T.; Yamada, T.; Kimura, K.; Tsuchida, A. “Drying dissipative structures of the deionized aqueous suspensions of colloidal silica spheres ranging from 29 nm to 1 μ m in diameter” *Colloid Polyme. Sci.* 283, 1007-1015 (2005)
- [50] Parisse, F.; Allain, C.; “Drying of Colloidal Suspension Droplets: Experimental Study and Profile Renormalization” *Langmuir* 13, 3598-3602 (1997)
- [51] Stefaniuk, T.; Wrobel, P.; Dominiak, R.; Gawlik, G.; Bajdor, K.; Zielecka, M.; Szoplik, T., “Self-assembly of arrays of micro-rings by colloidal evaporative deposition” *Surf. Sci.* 601, 4922-4924 (2007)
- [52] Ko, H.-Y.; Park, J.; Shin, H.; Moon, J. “Rapid Self-Assembly of Monodisperse Colloidal Spheres in an Ink-Jet Printed Droplet” *Chem. Mater.* 16, 4212-4215 (2004).
- [53] Park, J. & Moon, J., “Control of colloidal particle deposit patterns within picoliter droplets ejected by ink-jet printing”, *Langmuir* 22, 3506-3513 (2006).

- [54] Takhistov, P. & Chang, H-C. “Complex stain morphologies”, *Ind. Eng. Chem. Res.* 41, 6256-6269 (2002).
- [55] Wang, J. & Evans, J.R.G. “Segregation in multicomponent ceramic colloids during drying of droplets”, *Phys. Rev. E* 73, 021501 (2006)
- [56] Chen, L.; Zhang, Y.; Yang, S.; Evans, J.R.G. “Protocols for printing thick film ceramic libraries using the London University Search Instrument (LUSI)” *Review of Scientific Instruments* 78, 072210 (2007)
- [57] Smalyukh, I.I.; Zribi, O.V.; Butler, J.C.; Lavrentovich, O.D.; Wong, G.C.L.; “Structure and Dynamics of Liquid Crystalline Pattern Formation in Drying Droplets of DNA” *Phys. Rev. Lett.* 96, 177801 (2006)
- [58] Nellimoottil, T.T.; Rao, P.N.; Chosh, S.S.; Chattopadhyay, A. “Evaporation-Induced Patterns from Droplets Containing Motile and Nonmotile Bacteria” *Langmuir* 23, 8655-8658 (2007)
- [59] Killeen, A.A.; Ossina, N.; McGlennen, R.C.; Minnerath, S.; Borgos, J.; Alexandrov, V.; Sarvazyan, A., “Protein self-organization patterns in dried serum reveal changes in B-cell disorders” *Mol. Diagn. Ther.* 10, 371-380 (2006)
- [60] Yakhno, T.A.; Yakhno, V.G.; Sanin, A.G.; Sanina, O.A.; Pelyushenko, A.S.; Egorova, N.A.; Terentiaev, I.G.; Smetanina, S.V.; Korochkina, O.V.; Yashukova, E.V., “The informative-capacity phenomenon of drying drops” *IEEE Engineering in Medicine and Biology Magazine* 24, 96-104 (2005)
- [61] Gibbs, J. W., “The Scientific Papers vol 1” (New York: Dover) (1961)
- [62] The collected works of J Willard Gibbs, Yale University Press, London, 1957
- [63] Peters, R., Yang, X., Kim, T., Sohn, B., and Nealey, P., “Using Self-Assembled Monolayers Exposed to X-rays To Control the Wetting Behavior of Thin Films of Diblock Copolymers”, *Langmuir* 16, 4625 (2000)
- [64] Lopes, W., Jaeger, H., “Hierarchical self-assembly of metal nanostructures on diblock copolymer scaffolds”, *Nature (London)* 414, 735 (2001)
- [65] Whitesides, G., Stroock, “Flexible methods for microfluidics”, *Phys. Today* 54, 42 (2001)
- [66] Li, D., “Drop size dependence of contact angles and line tension of solid-liquid systems” *Colloid surf. A* 116, 1-23 (1996)
- [67] Neumann, A.W., Good, R. J., “Thermodynamics of contact angles. I. Heterogeneous solid surfaces”, *Colloid Interface Sci.* 38 341-358 (1972)
- [68] Wenzel, R. N., “RESISTANCE OF SOLID SURFACES TO WETTING BY WATER” *Ind. Eng. Chem.* 28, 988-994 (1936)

- [69] Cassie, A. B. D., Bazter, S., "Wettability of porous surfaces", *Trans. Faraday Soc.*, 40, 546-551 (1944)
- [70] Shittleworth, R., Bailey, G. L., "The spreading of a liquid over a rough solid" *Discuss. Faraday Soc.*, 3, 16-22 (1948)
- [71] Johnson, R. E. Jr., Dettre, R. H., "Contact Angle Hysteresis. III. Study of an Idealized Heterogeneous Surface" *J. Phys. Chem.*, 68, 1744-1750 (1964)
- [72] Li, D., Neumann, A. W., "Surface heterogeneity and contact angle hysteresis" *Colloid Polym. Sci.*, 270, 498-504 (1992)
- [73] Schwartz, L. W., Garoff, S., "Contact angle hysteresis and the shape of the three-phase line" *J. Colloid Interface Sci.*, 106, 422-437 (1985)
- [74] Churaev, N. V., "Wetting films and wetting" *Rev. Phys. Appl.*, 23, 975-987 (1988)
- [75] Langmuir, I., "Oil Lenses on Water and the Nature of Monomolecular Expanded Films" *J. Chem. Phys.*, 1, 756-776 (1933)
- [76] Gershfeld, N. L., Good, R. J., "Line tension and the penetration of a cell membrane by an oil drop" *J. Theor. Biol.*, 17, 246-251 (1967)
- [77] Wallace, J. A., Schürch, S., "Line tension of a sessile drop on a fluid—fluid interface modified by a phospholipid monolayer" *J. Colloid interface Sci.*, 124, 452-461
- [78] Yekta-Fard, M., Ponter, A. B., "The influences of vapor environment and temperature on the contact angle-drop size relationship" *J. Colloid Interface Sci.*, 126, 134-140 (1988)
- [79] Drelich, J., Miller, J., "The effect of surface heterogeneity on pseudo-line tension and the flotation limit of fine particles" *Colloids Surf.*, 69, 35-43 (1992)
- [80] Drelich, J., Miller, J., "The Effect of Solid Surface Heterogeneity and Roughness on the Contact Angle/Drop (Bubble) Size Relationship" *J. Colloid Interface Sci.*, 164, 252-259 (1994)
- [81] Gaydos, J., Neumann, A. W., "The dependence of contact angles on drop size and line tension" *J. Colloid Interface Sci.*, 120, 76-86, (1987)
- [82] Li, D., Neumann, A. W., "Determination of line tension from the drop size dependence of contact angles" *Colloids Surf.*, 43, 195-206 (1990)
- [83] Cuncan, D., Li, D., Gaydos, J., Neumann, A. W., "Correlation of Line Tension and Solid-Liquid Interfacial Tension from the Measurement of Drop Size Dependence of Contact Angles" *J. Colloid Interface Sci.*, 169, 256-261 (1995)
- [84] Boruvka, L., Neumann, A. W., "Generalization of the classical theory of capillarity" *J. Chem. Phys.* 66, 5464-5476 (1977)

- [85] Toshev, B. V., Platikanov, D., Scheludko, A., "Line tension in three-phase equilibrium systems" *Langmuir*, 4, 489-499 (1988)
- [86] Tarazona, P., Navascues, G., "Thermodynamics of deformable three-phase systems" *Physica A*, 115, 490-500 (1982)
- [87] Drelich, J., "The significance and magnitude of the line tension in three-phase (solid-liquid-fluid) systems" *Colloid Surf. A* 116, 43-54 (1996)
- [88] Getta, T., Dietrich, S., "Line tension between fluid phases and a substrate" *Phys. Rev. E* 57, 655-671 (1998)
- [89] Harkins, W. D., "Linear or Edge Energy and Tension as Related to the Energy of Surface Formation and of Vaporization" *J. Chem. Phys.* 5, 135-140 (1937)
- [90] Bresme, F., Quirke, N., "Computer simulation study of the wetting behavior and line tensions of nanometer size particulates at a liquid-vapor interface", *Phys. Rev. Lett.* 80, 3791-3794 (1998)
- [91] Rowlinson, J. S., Widom, B., "Molecular Theory of capillarity" (Oxford University Press, New York, 1984), p. 240.
- [92] Churaev, N. V., Starov, V. M., Derjaguin, B. V., "The shape of the transition zone between a thin film and bulk liquid and the line tension" *J. Colloid Interface Sci.* 89, 16-24 (1982)
- [93] Pompe T.; Herminghaus, S., "Three-Phase Contact Line Energetics from Nanoscale Liquid Surface Topographies" *Phys. Rev. Lett.*, 85, 1930-1933 (2000)
- [94] Wang, J. Y.; Betelu, S.; Law, B.M., "Line tension approaching a first-order wetting transition: Experimental results from contact angle measurements" *Phys. Rev. E.* 63, 031601-031612 (2001).
- [95] Milchev A.I.; Milchev, A.A.; "Wetting behavior of nanodroplets: The limits of Young's rule validity" *Europhys. Lett.* 56, 695-701 (2001)
- [96] Checco, A.; Guenoun, P., "Nonlinear dependence of the contact angle of nanodroplets on contact line curvature" *Phys. Rev. Lett.* 91, 186101-186105 (2003)
- [97] Quéré, D.; "Surface wetting: Model droplets" *Nature Materials* 3, 79-80 (2004)
- [98] Amirfazli A.; Neumann A.W., "Status of the three-phase line tension: a review" *Adv. Colloid Interface Sci.* 110, 121-141 (2004)
- [99] Guo, H.-K.; Fang, H.-P., "Drop Size Dependence of the Contact Angle of Nanodroplets" *Chin. Phys. Lett.* 22, 787-790 (2005)
- [100] Barberis, F.; Beruto, D.T., "Adsorption of paraffin vapor on oxidized molybdenum substrates at nano- and micro-scales" *J. Colloid Interface Sci.* 313, 592-599 (2007)

- [101] Letellier, P.; Mayaffre, A.; Turmine, M., “Drop size effect on contact angle explained by nonextensive thermodynamics Young's equation revisited” *J. Colloid Interface Sci.* 314, 604-614 (2007)
- [102] Drelich, J.; Miller, J., “The line/pseudo-line tension in three-phase systems”, *Particul. Sci. Technol.*, 10, 1-20 (1992)
- [103] Drelich, J., Miller, J., Kumar, A., and Whitesides, G. M., “Wetting characteristics of liquid drops at heterogeneous surfaces” *Colloids Surfaces A* 93, 1-15 (1994)
- [104] Langmuir, I., “The evaporation of small droplets”, *Phys. Rev.* 12, 368-370 (1912).
- [105] Xu, F.T.; Street, S.C.; Barnard, J.A. “Coverage Dependent Evolution of Two-Dimensional Dendrimer/Mica Domain Patterns” *J. Phys. Chem. B* 107, 12762-12767 (2003)
- [106] Heslot, F., Fraysse, N. & Cazabat, A.M. “Molecular layering in the spreading of wetting drops”, *Nature* 338, 640-642 (1989).
- [107] Santer, S., Zong, Y., Knoll, W., & R uhe, J. “On the formation of molecular terraces”, *Langmuir* 21, 8250-8254 (2005).
- [108] Burton, W.K., Cabrera, N., & Frank, F.C. “The growth of crystals and the equilibrium structure of their surfaces”, *Philos. Trans. R. Soc. London, Ser. A* 243, 299-358 (1951).
- [109] Bales, G.S., Zangwill, A. M. “Morphological instability of a terrace edge during step-flow growth”, *Phys. Rev. B* 41, 5500-5508 (1990)
- [110] Brochard-Wyart, F. & Redon, C. “Dynamics of liquid rim instabilities”, *Langmuir* 8, 2324-2329 (1992)
- [111] Vuilleumier, R., Ego, V., Neltner, L., & Cazabat, A.M. “Tears of wine: the stationary state”, *Langmuir* 11, 4117-4121 (1995)
- [112] Sekimoto, K., Oguma, R., & Kawasaki, K. “Morphological stability analysis of partial wetting”, *Ann. Phys.* 176, 359-392 (1987)
- [113] Roy, R.V. & Schwartz, L.W. “On the stability of liquid ridges”, *J. Fluid Mech.* 391, 293-318 (1999)
- [114] Choi, S-H., Newby, B.Z., “Dynamic contact angle in rim instability of dewetting holes” *J. Chem. Phys.* 124, 054702 (1-6) (2006)
- [115] Rayleigh, L. “On the instability of a cylinder of viscous liquid under capillary force”, *Philos. Mag.* 34, 145-154 (1892)
- [116] Nasirzadeh, K., Neueder, R., & Kunz, W., “Vapor pressure determination of the aliphatic C5 to C8 1-alcohols”, *J. Che. Eng. Data* 51, 7-10 (2006)

- [117] Saleh, M.A., Akhtar, S., Begum, S., Ahmed, M.S., & Begum, S. "Density and Viscosity of 1 alkanols", *Phys. and Chem. of Liquids* 42, 615-623 (2004)
- [118] Mullins, W. W.; Sekerka, R. F. "Morphological Stability of a Particle Growing by Diffusion or Heat Flow" *J. Appl. Phys.* 34, 323-329 (1963)
- [119] Mullins, W. W.; Sekerka, R. F. "Stability of a Planar Interface During Solidification of a Dilute Binary Alloy" *J. Appl. Phys.* 35, 444-451 (1964)
- [120] Di Tolla, F. D.; Ercolessi, F.; Tosatti, E., "Maximum Overheating and Partial Wetting of Nonmelting Solid Surfaces" *Phys. Rev. Lett.* 74, 3201-3204 (1995)
- [121] Zykova-Timan, T.; Tartaglino, U.; Ceresoli, D.; Sekkal-Zaoui, W.; Tosatti, E., "NaCl nanodroplet on NaCl(100) at the melting point" *Surface Science*, 566-568, 794-798 (2004)
- [122] Tartaglino, U.; Zykova-Timan, T.; Ercolessi, F.; Tosatti, E. "Material surfaces and nanosystems close to the melting temperature" *Journal of Materials Science* 40, 2141-2147 (2005)